

Structure analysis of the Perseus and the Cepheus B molecular clouds

Inaugural-Dissertation

zur

Erlangung des Doktorgrades
der Mathematisch-Naturwissenschaftlichen Fakultät

der Universität zu Köln

vorgelegt von

Kefeng Sun

aus VR China

Köln, 2008

Berichterstatter : Prof. Dr. Jürgen Stutzki
Prof. Dr. Andreas Zilges

Tag der letzten mündlichen Prüfung : 26.06.2008

To my parents and Jiayu

Contents

Abstract	i
Zusammenfassung	v
1 Introduction	1
1.1 Overview of the interstellar medium	1
1.1.1 Historical studies of the interstellar medium	1
1.1.2 The phases of the ISM	2
1.1.3 Carbon monoxide molecular clouds	3
1.2 Diagnostics of turbulence in the dense ISM	4
1.2.1 The Δ -variance method	6
1.2.2 <i>Gaussclumps</i>	8
1.3 Photon dominated regions	9
1.3.1 PDR models	12
1.4 Outline	12
2 Previous studies	14
2.1 The Perseus molecular cloud	14
2.2 The Cepheus B molecular cloud	16
3 Large scale low -J CO survey of the Perseus cloud	18
3.1 Observations	18
3.2 Data Sets	21
3.2.1 Integrated intensity maps	21
3.2.2 Velocity structure	24
3.3 The Δ -variance analysis	24
3.3.1 Integrated intensity maps	27
3.3.2 Velocity channel maps	30
3.4 Discussion	34
3.4.1 Integrated intensity maps	34
3.4.2 Velocity channel maps	34

3.5	Summary	38
4	The <i>Gaussclumps</i> analysis in the Perseus cloud	40
4.1	Results and discussions	40
4.1.1	Clump mass	41
4.1.2	Clump mass spectra	42
4.1.3	Relations of clump size with line width and mass	46
4.1.4	Equilibrium state of the clumps	49
4.2	Summary	53
5	Study of the photon dominated region in the IC 348 cloud	55
5.1	Datasets	56
5.1.1	[C I] and ^{12}CO 4–3 observations with KOSMA	56
5.1.2	Complementary data sets	57
5.2	Observational results	57
5.3	LTE Analysis	63
5.4	PDR Model	67
5.4.1	FUV intensity	67
5.4.2	Clumpy PDR scenarios	68
5.5	Summary and Conclusions	78
6	Multi-line study of the Cepheus B cloud	80
6.1	The IRAM 30m telescope observations	81
6.2	Chemical tracers at the PDR interfaces	81
6.3	Two observed cuts	83
6.4	Results	85
6.4.1	Spectra at the two interface positions	85
6.4.2	Integrated intensities along the two cuts	91
6.4.3	LTE analysis	91
6.5	Summary and outlook	95
7	Summary and future prospects	97
7.1	Summary of results	97
7.2	Future prospects	99
A	Local thermodynamic equilibrium analysis	101
A.1	Opacity	101
A.2	Excitation temperature	102
A.3	Column density	102
A.4	Mass	103

B	A new atmospheric calibration method	104
B.1	Introduction	104
B.1.1	Atmospheric model	105
B.2	The previous calibration (Hiyama's)	106
B.3	The new calibration scheme	107
B.4	Testing the new calibration	108
B.4.1	How to use <i>Kalibrate</i>	108
B.4.2	On simulations	112
B.4.3	On real data	116
B.5	Conclusion	116
C	A uniform observing script	118
	Reference	121
	List of Figures	136
	List of Tables	144
	Acknowledgments	147
	Publications	151
	Lebenslauf	152

Abstract

Astronomical observations have shown that molecular clouds are the birth places of new stars and planets. As molecular clouds are massive objects with a mass varying from $\sim 10^6$ to a few solar masses, a mechanism is needed to break up the molecular clouds into stellar size fragments. Star formation occurs when individual fragments become gravitationally dominated, which can occur either spontaneously or triggered by external forces. Molecular clouds are observed to be turbulent. Turbulence plays a dual role in star formation. It creates density fluctuations to initiate gravitational collapse; on the other hand, it can counter local collapse. Hence, the cloud structure and dynamics control important properties of star formation.

In the first part of this work, I study the structural properties of Galactic molecular clouds. To determine cloud properties, observable quantities, such as (integrated) intensities, spectral line profiles of the standard tracers are used. The carbon monoxide, CO, molecule is the second most abundant molecule in the Universe after H_2 and because of its low rotational excitation energy, it is the principal molecule to study the molecular gas in galactic and extragalactic sources. Its isotopomer ^{13}CO is often optically thin, and is a good tracer of column density. In this work, four rotational transitions of ^{12}CO and ^{13}CO are employed: ^{12}CO 1–0 and 3–2, and ^{13}CO 1–0 and 2–1.

For both dust continuum maps and integrated line intensity maps, it has been shown that the observed intensities follow a power law scale relation. The spatial structure of the emission has been quantified in terms of its power spectrum that is the Fourier transform of the autocorrelation function. For a given observable quantity, the power spectrum gives a plot of the portion of power falling within given unit bins. When fitting the azimuthally averaged power spectrum with a power law, the fitted slope β provides information on the relative amount of structure at the linear scales resolved in the image. I apply the Δ -variance method to quantitatively characterize the observed cloud structures. The Δ -variance method measures the relative amount of structure on a given scale by filtering an observed map by a radially symmetric wavelet with a characteristic length scale L and computing the total variance in the convolved map. Within the typical range

of spectral indices measured in interstellar clouds, the fitted exponent from the Δ -variance method can be related to the exponent of the power spectrum. The advantage of the Δ -variance method is that it allows clear discrimination against the noise and other systematic effects (finite size, beam smearing) in the observed maps.

There is a different approach to quantify the observed cloud structure, which is the decomposition of the observed emission into discrete entities clumps in order to establish scaling relations for the clumps e.g. mass-size relation and clump mass spectra. For this purpose, I use the method, *Gaussclumps*. This method identifies a clump as a Gaussian shaped least square fit to the surroundings of the present map maximum, and successively subtracts one clump after the other until the complete intensity has been assigned to clumps. *Gaussclumps* can identify efficiently small clumps near the resolution limit of the observations, and thus it is very helpful to obtain a complete clump mass spectrum that measures the number of clumps of a given mass.

The Perseus molecular cloud has been selected for these studies. Since it is one of the best examples of the nearby active low- to intermediate-mass star forming regions.

The Δ -variance method is applied to both the CO integrated intensity maps and the velocity channel maps that present spatial distribution of line intensities at each successive velocity interval. The spectral index β of the corresponding power spectrum is determined. Its variation across the cloud and across the lines is studied. It is found that the power spectra of all CO line integrated maps of the whole complex show the same index, $\beta \approx 3.1$, for scales between about 0.2 and 3 pc, independent of isotopomer and rotational transition. However, the CO maps of individual subregions show a variation of β . The ^{12}CO 3–2 data provide a spread of indices between 2.9 in L 1455 and 3.5 in NGC 1333. In general, active star forming regions show a larger power-law exponent. I use the velocity channel analysis to study the statistical relation between the neighboring channel maps. Some theory predicts systematic increase of the spectral index with channel width. Such systematic increase is only detected in the blue line wings for the CO data.

I apply *Gaussclumps* to the whole observed Perseus cloud and seven subregions, and to derive the clump properties as traced in ^{13}CO 1–0 and 2–1. With the individual clumps identified, their properties such as mass, size, velocity width are derived. The clumps identified have a power law mass spectrum, and a power law index ~ 1.9 of clump mass spectra. The virial parameter, which is the ratio between virial mass and the mass estimated from the Local Thermodynamic Equilibrium (LTE) analysis, is used to characterize the equilibrium state of a clump. The LTE assumes that all distribution functions characterizing the material and its interaction with the radiation field at one position are given by thermodynamic equilibrium relations at local values of the temperature and density. Virial mass

here is the mass of a clump in statistical equilibrium derived by using the virial theorem. All clumps identified in both NGC 1333 and L 1455 are found with a virial parameter above 1. The external pressure needed to bind the clumps falls within 10^3 K cm^{-3} and 10^6 K cm^{-3} for the whole observed Perseus cloud, while it varies between active star formation regions and quiescent dark clouds.

After stars form, they provide important feedback mechanisms for regulating star formation: ultraviolet (UV) radiation dissociates molecules, ionizes, and heats the gas and the dust in photon dominated regions (PDRs). Outflows, radiation driven bubbles, and supernova (SN) shells provide mechanical energy input. All effects lead to the dispersion of molecular clouds and to the compression of cores possibly triggering further star formation. The study of photon dominated regions is to understand the effects of stellar far-ultraviolet photons on the structure, chemistry, thermal balance, and evolution of the neutral interstellar medium of galaxies.

The second part of this thesis is to study the physical properties of the transition layers on the surface of molecular clouds, i.e. Galactic photon dominated regions. Two clouds are selected for the study: IC 348 and Cepheus B. Both clouds are close to the radiation field of the bright stars that are part of the youngest generation. Hence, they are ideal places to study the properties of PDRs.

The KOSMA - τ PDR model is used to interpret the observed line intensities. It is a spherical PDR model, which computes the chemical and temperature structure of a spherical clump illuminated by an isotropic FUV radiation field and cosmic rays. The form of carbon changes with increasing depth from the surface of the PDR from C^+ through C^0 to CO. Therefore emission from $[\text{C II}]$, $[\text{C I}]$ and the rotational lines of CO can be used as probes of temperature, density and column density in the PDRs. I use the data of ^{12}CO 1–0, 4–3, ^{13}CO 1–0 and $[\text{C I}]$ $^3\text{P}_1 - ^3\text{P}_0$ to study physical and chemical properties of the PDRs in IC 348.

New observations of maps in $[\text{C I}]$ at 492 GHz and ^{12}CO 4–3 with a resolution of $\sim 1'$ are combined with the FCRAO data of ^{12}CO 1–0, ^{13}CO 1–0 and far-infrared continuum data. To derive the physical parameters of the region, three independent line ratios are analyzed using the following: a simple LTE analysis; KOSMA - τ PDR model considering an ensemble of PDR clumps. Detailed fits to observations are presented at seven representative positions in the cloud revealing clump densities between about $4.4 \cdot 10^4 \text{ cm}^{-3}$ and $4.3 \cdot 10^5 \text{ cm}^{-3}$, and C/CO column density ratios between 0.02 and 0.26. The FUV flux obtained from the model fit is consistent with that derived from FIR continuum data, varying between 2 to 100 Draine units across the cloud. An ensemble of a few tens PDR clumps with a total mass of a few solar masses and a beam filling close to unity reproduces the observed line intensities and intensity ratios.

A multi-line study in the Cepheus B molecular clouds is presented. Two $5'$ long cuts have been observed for up to three transitions of the CS, HCO^+ ,

HCN, HNC, CN, and C₂H molecules. The integrated intensity distribution along the cuts have been calculated and a least square fit is used to the observed hyperfine structure of C₂H, CN and HCN for deriving the opacities. At the two interface positions, column densities of H₂, ¹²CO, ¹³CO, C¹⁸O, CS, C³⁴S, HCO⁺, H¹³CO⁺, HCN, HNC, HCS⁺ and HCO are estimated under the LTE assumption.

The thesis presents the comparison of the structural properties for entire surveys and sub-sets, as well as the velocity channel analysis, provide additional, significant characteristics of the ISM in observed CO spectral line maps. These quantities are useful for a comparison of the structure observed in different clouds, possibly providing a diagnostic tool to characterize the star-formation activity and providing additional constraints for numerical simulations of the ISM structure. The thesis also studies different PDRs subject to low and intermediate FUV fields using the clumpy KOSMA - τ PDR model. Future observations will be useful to constrain the models and to judge the importance of different input parameters used. A better knowledge of these conditions in IC 348 and Cepheus B will provide a template for future studies of Galactic PDRs and the ISM in external galaxies.

Zusammenfassung

Astronomische Beobachtungen haben gezeigt, dass in Molekülwolken die Entstehungsgebiete neuer Sterne und Planeten liegen. Da Molekülwolken massive Objekte mit Massen im Bereich von einigen Sonnenmassen bis 10^6 Sonnenmassen sind, gibt es einen Mechanismus zur Entstehung stellarer Massen-Fragmente. Die Sternentstehung beginnt, wenn einzelne Fragmente von der Gravitationskraft dominiert werden, was entweder spontan oder durch externe Kräfte initialisiert werden kann. Beobachtungen zeigen, dass Molekülwolken turbulent sind. Die Turbulenz spielen dabei eine duale Rolle in der Sternentstehung: einerseits werden Dichtefluktuationen erzeugt die Kollaps durch Gravitation erzeugen; zum Anderen verhindert die Turbulenz lokalen Kollaps. In diesem Sinne bestimmen räumliche Struktur und Dynamik der Molekülwolken wichtige Eigenschaften der Sternentstehung.

Im ersten Teil dieser Arbeit werden die strukturellen Eigenschaften galaktischer Molekülwolken untersucht. Um die Eigenschaften der Molekülwolken zu bestimmen, benutzen wir Beobachtungsgrößen wie (integrierte) Intensitäten und spektrale Linienprofile von üblichen Linienübergängen. Das Kohlenmonoxid-Molekül, CO, ist das nach dem H_2 zweithäufigste Molekül im Universum. Durch seine niedrige Rotationsanregungsenergie ist es das meiststudierte Molekül in galaktischen und extragalaktischen Quellen. Das ^{13}CO Isotop ist häufig optisch dünn und eignet sich deshalb als Indikator für Säulendichten. In dieser Arbeit benutzen wir 4 Rotationsübergänge von ^{12}CO und ^{13}CO : ^{12}CO 1–0 und 3–2, und ^{13}CO 1–0 und ^{13}CO 2–1.

Um die Struktur der Molekülwolken zu quantifizieren, benutzen wir die Δ –Varianz Methode und *GAUSSCLUMPS*. Die Δ –Varianz Methode ermöglicht die Identifizierung von Rauschen und anderen systematischen Effekten (begrenzte Größe, Beam-Verschmierung) in den beobachteten Karten. *GAUSSCLUMPS* kann effizient kleine Klumpen nahe des Auflösungslimits der jeweiligen Beobachtungen identifizieren und ist deshalb sehr hilfreich für die Bestimmung eines kompletten Klumpen-Massen Spektrums, welches die Zahl der Klumpen in einem Massenintervall angibt.

Die Molekülwolke Perseus wurde für diese Beobachtungen ausgewählt, da Sie

eine der besten Beispiele für eine nahegelegene aktive Sternentstehungsregion im niedrigen und mittleren Massenbereich darstellt.

Wir haben das Power-Spektrum der Fourier-Transformierten der Autokorrelationsfunktion der räumlichen Struktur der Emission bestimmt. Für eine bestimmte Beobachtungsgröße quantifiziert das Powerspektrum die Energie die in bestimmten räumlichen Einheiten auftritt. Durch Anpassen eines Power-Laws mit Steigung β an das Power-Spektrum, können wir studieren, welcher Anteil der Struktur auf verschiedenen linearen Skalen in der Region aufgelöst wurde. Die Δ -Varianz Methode wurde sowohl auf die integrierten CO Intensitätskarten als auch auf die Geschwindigkeitskanalkarten angewandt, die die räumliche Verteilung der Linienintensitäten in unterschiedlichen Geschwindigkeitsbereichen quantifizieren. Der spektrale Index β der korrespondierenden Power-Spektren wird bestimmt. Wir finden, dass auf Skalen von 0.2-3pc die integrierten Karten des gesamten Perseus-Komplexes unabhängig von Isotopomer und Rotationsübergang einen Spektral Index $\beta = 3.1$ haben. Die CO-Karten individueller Teilregionen zeigen Variation in β . ^{12}CO 3-2 Daten zeigen einen β -Bereich von 2.9 in L 1455 bis 3.5 in NGC 1333. Im Allgemeinen findet man größere Power-Indizes in aktiven Sternentstehungsgebieten. Die Abhängigkeit der Powerspektren der Kanalkarten von der Breite der Geschwindigkeitskanäle zeigt sich nur in der Zunahme der Spektralindizes im blauen Linienflügel.

GAUSSCLUMPS identifiziert einen Klumpen als gaußförmigen least-square Fit zum aktuellen Maximum der Karte und subtrahiert iterativ Klumpen von der Karte bis die komplette Intensität in Klumpen aufgeteilt wurde. Ich benutze diese Methode in der gesamten Perseus Wolke und in sieben Sub-Regionen, um die Klumpeneigenschaften in ^{13}CO 1-0 und 2-1 zu studieren. Für die einzelnen identifizierten Klumpen untersuchen wir Masse, Größe und Geschwindigkeitsbreite des jeweiligen Klumpens. Die identifizierten Klumpen zeigen ein Powerlaw mit einem Index ~ 1.9 des Klumpen-Massen Spektrums. Der Virialparameter, das Verhältnis aus Virialmasse und Masse berechnet unter Annahme lokalen thermischen Gleichgewichtes (LTE), beschreibt den Gleichgewichtszustand der Klumpen. Die LTE-Annahme impliziert, dass sich alle Verteilungsfunktionen, die Materie und seine Interaktion mit dem Strahlungsfeld beschreiben, durch lokale Werte für Temperatur und Dichte im thermodynamischen Gleichgewicht beschreiben lassen. Mit Virialmasse bezeichnen wir hier die Gleichgewichtsmasse eines Klumpen hergeleitet unter Annahme des Virialtheorems. Alle Klumpen in den Regionen NGC 1333 und L1455 haben Virialparameter größer als 1. Der externe Druck, der benötigt wird um einen Klumpen zu binden, ist zwischen 10^3Kcm^{-3} und 10^6Kcm^{-3} im gesamten Perseus-Gebiet. Zwischen aktiven Sternentstehungsgebieten und Dunkelwolken finden wir Variationen in den Virialparametern.

Nach der Entstehung von Sternen sind diese ein wichtiger Teil der Regulierung

neuer Sternentstehung: ultraviolett (UV) Strahlung dissoziiert Moleküle, ionisiert und heizt Gas und Staub in Photonen dominierten Regionen (PDRs). Durch Ausflüsse, durch Strahlungsblasen und Supernovaschalen wird mechanische Energie abgegeben. Alle Effekte führen zur Dispersion der Molekülwolken und möglichen neuen Sternentstehung in neuen komprimierten Kernen. Die Studien Photonen dominierten Regionen helfen dabei, die Effekte der stellaren UV-Strahlung auf Struktur, Chemie, thermisches Gleichgewicht und die Entwicklung des neutralen interstellaren Mediums in Galaxien zu verstehen.

Im zweiten Teil dieser Arbeit werden die physikalischen Eigenschaften der Übergangsschichten an der Oberfläche von Molekülwolken studiert, d.h. Galaktische PDRs. Dafür werden zwei Regionen betrachtet: IC348 und CepheusB. Beide Wolken liegen im Strahlungsfeld heller junger Sterne und damit ideal um die Eigenschaften von PDRs zu untersuchen.

Das KOSMA- τ PDR-Model wird benutzt um die beobachteten Linienintensitäten zu interpretieren. Das Model ist ein sphärisches PDR-Model und berechnet die chemische Struktur und Temperaturverteilung eines Klumpens, der in einem isotropen FUV- und kosmischen Strahlungsfeld liegt. Die Form in der Kohlenstoff vorliegt ändert sich im Klumpen mit zunehmenden Abstand von der Oberfläche von C^+ über C zu CO. Deshalb können [C II], [C I] und die Rotationsübergänge von CO benutzen, um Temperatur, Dichte und Säulendichte in PDRs zu bestimmen. In dieser Arbeit werden ^{12}CO 1–0, 4–3, ^{13}CO 1–0 und [C I] 1–0 um die chemischen und physikalischen Eigenschaften der PDRs in IC348 zu studieren.

Dazu werden neu beobachtete Karten in [C I] bei 492 GHz und ^{12}CO 4–3 bei ca. 1' Auflösung mit FCRAO-Daten der Linien ^{12}CO 1–0, ^{13}CO 1–0 und Fern-Infrarot (FUV) Kontinuum-Daten kombiniert. Um die physikalischen Parameter dieser Region zu bestimmen, analysieren wir wie folgt drei unabhängige Linienverhältnisse: mit einer einfachen LTE-Analyse und mit Hilfe des KOSMA- τ PDR-Models und einem Ensemble von Klumpen. An sieben repräsentativen Positionen der Wolke diskutieren wir detaillierte Fits an die Beobachtungen, welche Klumpen-Dichten zwischen $4.4 \cdot 10^4$ und $4.3 \cdot 10^5 \text{ cm}^{-3}$ ergeben. Die Fits für den FUV-Fluss aus dem PDR-Model sind konsistent mit Ergebnissen aus den FUV Kontinuum-Daten und variieren zwischen 2 und 100 Draine-Einheiten in der Wolke. Ein Ensemble einigen zehn PDR Klumpen mit einer totalen Masse von einigen zehn Sonnenmassen und einem Füllfaktor nahe 1 reproduziert die beobachteten integrierten Intensitäten und Linienverhältnisse.

Eine Studie in verschiedenen Linien in der CepheusB-Molekülwolke wird vorgestellt. In zwei 5' langen Schnitten wurden bis zu drei Linienübergänge der CS,, HCO^+ , HCN, HNC, CN, und C_2H Moleküle beobachtet. Es wurden die integrierten Intensitäten berechnet und ein least-square Fit wurde benutzt um aus den beobachteten Hyperfeinstrukturübergängen von C_2H , CN und HCN die Opazitäten zu bestimmen. An zwei Interface-Positionen werden H_2 , ^{12}CO , ^{13}CO , C^{18}O , CS,

C^{34}S , HCO^+ , H^{13}CO^+ , HCN , HNC , HCS^+ und HCO Säulendichten unter der Annahme von LTE bestimmt.

Diese Arbeit präsentiert den Vergleich der strukturellen Eigenschaften kompletter Studien und Untermengen, ebenso wie die Analyse von Geschwindigkeitsskanalkarten. Diese zeigen zusätzliche, wichtige Eigenschaften des interstellaren Mediums in den beobachteten CO-Karten. Diese Größen sind nützlich um einen Vergleich der Struktur in verschiedenen Wolken zu studieren um damit eine mögliche Diagnostik zur Charakterisierung der Sternentstehungs Aktivität zu erhalten und weitere Einschränkungen für numerische Simulationen der Struktur des ISM. Außerdem werden in dieser Arbeit mit Hilfe des klumpigen KOSMA- τ PDR-Models verschiedene PDR-Regionen in niedriger und mittlerer FUV-Strahlung studiert. Zukünftige Beobachtungen werden helfen, die Modelle weiter einzuschränken und die Wichtigkeit verschiedener Parameter zu bestimmen. Ein besseres Verständnis der Bedingungen in IC 348 und Cepheus B wird eine nützliche Referenz für zukünftige Studien in galaktischen PDRs und des ISM in externen Galaxien darstellen.

Chapter 1

Introduction

1.1 Overview of the interstellar medium

1.1.1 Historical studies of the interstellar medium

In 1811, William Herschel created a catalog of bright patches on the sky and called them *nebulae*. In 1904, Johannes Hartmann discovered stationary [Ca II] lines in the spectrum of the spectroscopic binary, δ Orionis, and he came to the conclusion that the gas responsible for the absorption was not present in the atmosphere of δ Orionis, but was instead located within an isolated cloud of matter residing somewhere along the line-of-sight to this star. This discovery started the study of the interstellar medium (ISM). Barnard (1919) catalogued 182 dark nebulae in the sky using photographs. Those dark places were considered to be possible holes in stellar distribution or obscuring matter. Heger (1922) observed a number of line-like absorption features which seemed to be interstellar in origin, which is the discovery of diffuse interstellar bands (DIBs). In 1944, van de Hulst predicted the existence of the 21 cm hyperfine line of neutral interstellar hydrogen. And the 21 cm emission was detected by Ewen & Purcell (1951); Muller & Oort (1951). The first interstellar molecules (CH, CH⁺, CN) were detected by Swings & Rosenfeld (1937); McKellar (1940); Adams (1941). Weinreb et al. (1963) discovered interstellar OH masers. And NH₃ was first detected in the ISM by Cheung et al. (1968). Wilson et al. (1970) detected ¹²CO 1–0 emission at 115 GHz, which later becomes the principal molecule to study the molecular gas in galactic and extragalactic sources. As of January 2008, there are more than 140 molecules listed as detected in the interstellar medium or circumstellar shells (CDMS, <http://www.astro.uni-koeln.de/vorhersagen/>).

Fig. 1.1 presents the Cone Nebula observed by the Hubble space telescope (HST). The Cone Nebula lies at a distance of about 770 pc. Fig. 1.1 shows the upper ~ 0.8 pc of the nebula. There are hot, young stars located beyond the top



Figure 1.1: Hubble space telescope image of Cone nebula (NGC2264): star forming pillar of gas and dust.

of the image. UV light from the stars heats the edges of the dark cloud, releasing gas into the relatively empty region of surrounding space. The red halo of light seen around the pillar is produced by additional ultraviolet radiation causing the hydrogen gas to glow. The blue-white light from surrounding stars is reflected by dust. Background stars can be seen peeking through the evaporating tendrils of gas, while the turbulent base is pockmarked with stars reddened by dust (taken from <http://hubblesite.org/newscenter/archive/releases/2002/11/image/b/>).

1.1.2 The phases of the ISM

The ISM includes a mixture of ions, atoms, molecules, larger dust grains, cosmic rays, and (galactic) magnetic fields (Spitzer, 1978). The Galactic matter consists of about 99% gas and 1% dust by mass. The gas is roughly 90.8% by number (70.4% by mass) of hydrogen and 9.1% by number (28.1% by mass) of helium, with a sprinkling (0.12% by number and 1.5% by mass) of heavier elements, which can be neutral, ionized, or in molecular form and in gas phase or in the solid state (Ferrière, 2001; Tielens, 2005). The interstellar gas is in a dynamical

state of constant change, driven by ultraviolet (UV) heating where stars are forming, by supersonic expansion of supernova explosions, and subject to dynamical instabilities on various scales from a small fraction of a parsec to thousands of parsecs (Burke & Graham-Smith, 2002). A wide span of densities and temperatures of the ISM has been found.

Ranges of densities and temperatures are usually indicated as components or phases. The term "phases" is used to denote components that may exist in thermal pressure equilibrium, with $P/k = nT \sim 3 \times 10^3 \text{ cm}^{-3} \text{ K}$ in the solar vicinity (Jenkins et al., 1983). In the three-phase model, those phases often include the following (McKee & Ostriker, 1977; Hollenbach & Tielens, 1999; Cox, 2005): the low-density hot ionized medium (HIM) with temperatures in excess of 10^5 K and densities below about 0.01 cm^{-3} ; the warm neutral medium (WNM) and the warm ionized medium (WIM) with densities in the range 0.1 to 1 cm^{-3} and temperatures of several thousand Kelvin; and the dense cold neutral medium (CNM) with densities above about 10 cm^{-3} and temperatures below 100 K (McKee & Ostriker, 1977; Kulkarni & Heiles, 1987).

The CNM itself contains a variety of cloud types, spanning a wide range of physical and chemical conditions. The densest clouds that are most protected from UV radiation from stars are referred to as dense clouds, dark clouds, or molecular clouds, which may be thought of as a short-term product of the ISM leading to star formation (Cox, 2005). The most tenuous clouds, fully exposed to starlight, are usually called diffuse clouds. Clouds that fall in between these two extremes are often referred to as translucent clouds (Snow & McCall, 2006). This thesis work mainly deals with molecular clouds, particularly carbon monoxide (CO) molecular clouds.

1.1.3 Carbon monoxide molecular clouds

Molecular clouds are composed of dust and molecular gas that is molecular hydrogen (H_2) and helium, with small amounts of heavier elements. They make up for about 50 to 75% of the dense interstellar medium in the Milky Way. Typically, molecular clouds are cold ($10 - 50 \text{ K}$) and dense ($10^2 - 10^6 \text{ cm}^{-3}$). Because of their dusty content, visible light can not penetrate into a molecular cloud. Hence, infrared and (sub)millimeter observations are needed.

Molecular hydrogen is the most abundant molecule in ISM and it plays a fundamental role in star formation. However, the first excitation state of the hydrogen molecule is about a few hundred Kelvin. And the hydrogen molecule is homonuclear, it does not have a permanent dipole moment and vibrational or rotational transitions do not occur in electric dipole transition. These transitions are allowed in electric quadrupole transition and therefore have very low probabilities. Thus, cold molecular hydrogen is very hard to observe. Fortunately, there are other

molecules mixed with the hydrogen and dust. The most abundant of these is carbon monoxide. CO is a very stable molecule and the first rotational excited state lies only 5 Kelvin above the ground state, and therefore is readily excited by the ambient cosmic microwave background radiation or collisions with neighboring molecules (usually H_2). CO is the principal molecule to study the molecular gas in galactic and extragalactic sources. The main rotational lines of CO are often optically thick. Thus it is also important to observe its isotopomers, ^{13}CO or C^{18}O . The abundance ratio between ^{12}CO and ^{13}CO is about 65 and it is about 470 between ^{12}CO and C^{18}O (Langer et al., 1990).

1.2 Diagnostics of turbulence in the dense ISM

Turbulence is extremely important for many physical processes that take place in the ISM, including star formation, cosmic ray and dust dynamics, magnetic field formation and evolution, and heat transport (Vázquez-Semadeni, 2000). For those reasons there is an increasing interest in the astronomical community on turbulence (Esquivel et al., 2007). Understanding the role and nature of interstellar turbulence has been the subject of intensive studies for about half a century now, but many aspects still remain open (Elmegreen & Scalo, 2004). Turbulence causes the formation of structures of many different length scales. The large scale structures contain most of the energy of the turbulent motion. The energy cascades from the large scale structures to smaller scale structures. This process continues and creates smaller and smaller structures which produces a hierarchy of structures. Major questions concern the mechanisms by which turbulent motions are driven and the role of the strong compressibility of the interstellar medium for the structure of the turbulent energy cascade.

Various methods (Scalo, 1984; Klein & Dickman, 1984; Péroult et al., 1986; Miesch & Bally, 1994; Stutzki et al., 1998; Rosolowsky et al., 1999) have been used to quantitatively characterize the interstellar turbulence. They study the two-point correlation function or directly the power spectrum of the observed emission. There are methods like autocorrelation, structure function and power spectra (Scalo, 1984; Klein & Dickman, 1984; Péroult et al., 1986; Miesch & Bally, 1994; Rosolowsky et al., 1999). Here I will only give details on the method used in the thesis, which is the Δ -variance method introduced by Stutzki et al. (1998). This method has proven to be particularly useful. It allows for a better separation of the intrinsic cloud structure from contributions resulting from the finite signal-to-noise in the data, the telescope beam and limited map size. In addition, problems related to the discrete sampling of the data can be avoided (Stutzki et al., 1998; Bensch et al., 2001). The detailed introduction of the Δ -variance method will be given in the following subsection.

One thing to be noted is that the astronomically observed maps are two dimensional projection of the structure. However, Stutzki et al. (1998) have shown that the spectral index β of the power spectrum for an spatially isotropic structure remains constant on projection, which means that the projected map of three dimensional density structures shows the same β as the original structure assuming that the astronomical structure is on the average isotropic.

Interstellar turbulence has also been characterized by a different approach to quantify the structure. That is the decomposition of the observed emission into discrete entities ("clumps") in order to establish scaling relations for the clumps e.g. mass-size relation and clump mass spectra (cf. Stutzki & Güsten, 1990; Williams et al., 1994; Kramer et al., 1998b; Heyer & Terebey, 1998). With an individual clump identified, its mass, size, line width, and other parameters can be determined. One of the more fundamental parameters of a clump is its mass. The mass is generally derived via the integrated intensity of an optically thin line. Hence, the clump mass is a very robust parameter and does not depend on the actual spatial or velocity resolution (unless small size clumps blend into a larger clump).

Several different methods (e.g. eye inspection, *Clumpfind* and *Gaussclumps*, etc.) have been developed to characterize the clumpy structure. There are studies reporting clump mass spectra by eye inspection (Carr, 1987; Loren, 1989; Nozawa et al., 1991; Lada et al., 1996; Blitz, 1993; Dobashi et al., 1996). But eye inspection is obviously limited to uncrowded fields and to the identification of only the larger clumps. Two computerized clump decomposition algorithms are widely used: *Clumpfind* and *Gaussclumps*. *Clumpfind* has been developed by Williams et al. (1994), which decomposes an observed image into a number of clumps by assigning each volume element of the three dimensional data cube to one of the local maxima identified in the observed intensity distribution. In this method the number of clumps is limited exactly to the number of local maxima in the observed data cube. The *Clumpfind* method allows the clumps to have arbitrarily complex shapes, while it fails to identify weaker clumps partially overlapping with larger ones. *Gaussclumps*, developed by Stutzki & Güsten (1990), is used in this thesis work. The detailed introduction of *Gaussclumps* will be given in the following subsection.

In the cases where clump masses have been derived for a significantly large number of clumps, the different methods agree in showing a clump mass spectral distribution following a power law mass spectrum of the form $dN/dM \propto M^{-\alpha}$ with α of 1.7 - 1.9 for large well-sampled maps (Blitz, 1993; Kramer et al., 1998b).

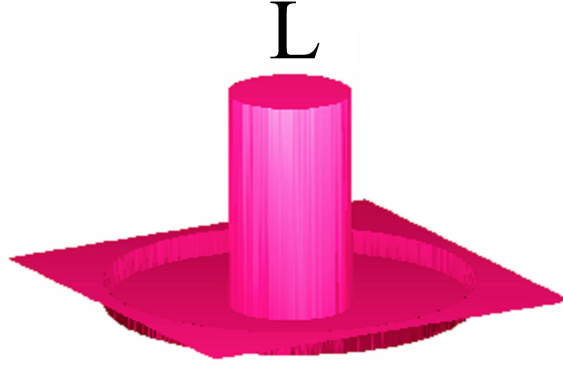


Figure 1.2: Example of the filter function used in the Δ -variance analysis

1.2.1 The Δ -variance method

The Δ -variance method is a means to quantify the relative amount of structural variation at a particular scale in a two dimensional map or a three dimensional data set. It follows the concept of the Allan-variance, originally introduced by Allan (1966) to study the stability of atomic clocks. The Δ -variance analysis provides an extension to functions in higher dimensions and can be applied to images and three dimensional structures. Consider a two dimensional scalar function $s = s(x, y)$ with x and y representing continuous Cartesian coordinates. Because we are mainly interested in spatial intensity distributions we refer to $s(x, y)$ as an "image". For the sake of simplicity we assume a vanishing average, $\langle s \rangle_{x,y} \equiv 0$. This is no essential restriction and can always be achieved by adding a constant. The Δ -variance is defined as the variance of an image $s(\vec{r})$ convolved with a normalized spherically symmetric wavelet \odot of size L

$$\sigma_{\Delta}^2 = \langle [s(\vec{r}) * \odot_L(\vec{r})]^2 \rangle_{\vec{r}}, \quad (1.1)$$

where the asterisk denotes the spatial convolution (Stutzki et al., 1998; Bensch et al., 2001) and is defined as below (see also Fig. 1.2):

$$\odot_L(\vec{r}) = \begin{cases} \frac{1}{\pi(L/2)^2}, & r \leq \frac{L}{2} \\ \frac{-1}{8\pi(L/2)^2}, & \frac{L}{2} < r \leq \frac{3L}{2} \\ 0, & r > \frac{3L}{2} \end{cases} \quad (1.2)$$

For structures characterized by a power-law spectrum, $P(|\vec{k}|) \propto |\vec{k}|^{-\beta}$ where $k = (k_x^2 + k_y^2)^{1/2}$, the Δ -variance follows as well a power law, with the exponent

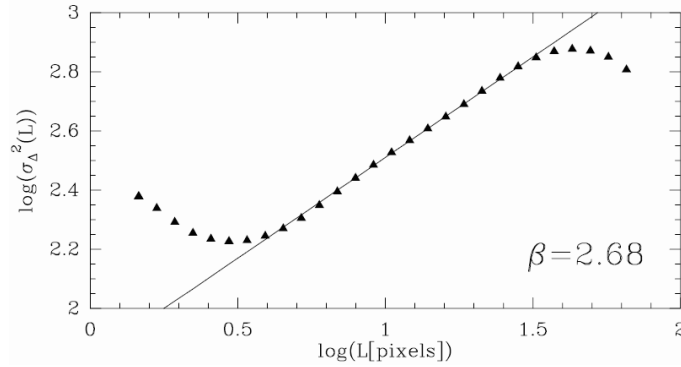


Figure 1.3: An example of a typical Δ -variance spectrum for a subset of the FCRAO outer galaxy survey (^{13}CO 1–0). This subset has a very large scale (384 by 128 pixels; $50''$ per pixel). The x axis is the lag and the y axis is the value of the variance. The black line indicates the power-law fits to the data. The turnover at the smallest angular scales shows the effect from the white noise behavior (for pure white noise, $\sigma_{\Delta}^2(L) \propto L^{-2}$); the turnover at the large angular scales is due to the influence of the typical size of main structures in the image. The figure is adapted from the Fig. 3 in the paper by Stutzki et al. (1998).

$d_{\Delta} = \beta - 2$ in the range $0 \leq \beta \leq 6$ (Stutzki et al., 1998). Fig. 1.3 presents an example of a Δ -variance spectrum.

Several studies have been performed using the Δ -variance method. Stutzki et al. (1998) used this method to study the structure of molecular cloud images (the Polaris Flare and subset of the Five College Radio Astronomy Observatory (FCRAO) outer galaxy survey). Their application to the observed CO maps shows the power spectrum has a power law shape and the power law index is close to $\beta = 2.8$ in clouds. Plume et al. (2000) employed the Δ -variance analysis for a quantitative comparison of the structure visible in the line-integrated maps of ^{13}CO 1–0 and $[\text{C I}]$ $^3\text{P}_1 - ^3\text{P}_0$ and found a typical β of ~ 2.6 . Bensch et al. (2001) presented a detailed study of the Δ -variance method as a tool to determine the power law power spectral index β of two dimensional intensity distributions. They applied the Δ -variance method to several observed CO maps, including surveys of giant molecular clouds made with the Bell Labs 7 m telescope and observations toward the Polaris Flare/MCLD 123.5+24.9. And they found that for linear scales ≥ 0.5 pc, the spectral index is remarkably uniform ($2.5 < \beta < 2.8$) for different clouds (quiescent/star forming) and tracers with different optical depths (^{12}CO and ^{13}CO $J = 1-0$). Significantly larger indices ($\beta > 3$) are found for the ^{13}CO 1–0 map of Perseus/NGC 1333 and observations made at higher spatial resolution toward MCLD 123.5+24.9. The index β found by Bensch et al. (2001) steepens in the Polaris Flare from 2.5 to 3.3 for maps with a linear resolution increasing from

$\gtrsim 1$ pc to $\lesssim 0.1$ pc.

1.2.2 *Gaussclumps*

Gaussclumps, developed by Stutzki & Güsten (1990), is a modified least square fitting procedure to decompose the observed three dimensional data cubes (two spatial coordinates, one spectral coordinate) into a series of clumps, which are assumed to have Gaussian shape (details on this algorithm can be found in Kramer et al., 1998b). Stutzki & Güsten (1990) tested the reliability of the Gaussian clump decomposition algorithm with artificially generated clump ensembles. The power law index of artificially created clump ensembles was reproduced by the algorithm to within less than 0.1 in the range $\alpha = 1.1$ to 1.75.

The clump decomposition provides the positions, LSR center velocities, orientations of the individual clumps, the clump sizes, brightness temperatures, and FWHM line widths. The intrinsic sizes of the clumps (i.e. de-convolved from the resolution) are calculated by:

$$x_{\text{ins}} = \sqrt{\Delta x^2 - d_{\text{beam}}^2}; y_{\text{ins}} = \sqrt{\Delta y^2 - d_{\text{beam}}^2}; v_{\text{ins}} = \sqrt{\Delta v^2 - v_{\text{res}}^2}. \quad (1.3)$$

Where x_{ins} , y_{ins} and v_{ins} are the three dimensional intrinsic sizes of a clump, Δx , Δy and Δv are clump parameters obtained from *Gaussclumps*, d_{beam} is the beam size, and v_{res} is the spectral resolution.

One advantage of *Gaussclumps* is that it can principally find clumps blending in position and velocity by a priori assuming a Gaussian shaped clump profile. While usually only clumps fulfilling the following criteria will be used to derive clump mass spectra, which is that the three dimensional intrinsic sizes of a clump, x_{ins} , y_{ins} and v_{ins} , are larger than 50% of the resolution. The criteria can be written as:

$$x_{\text{ins}} > 0.5 \cdot d_{\text{beam}}; y_{\text{ins}} > 0.5 \cdot d_{\text{beam}}; v_{\text{ins}} > 0.5 \cdot v_{\text{res}}. \quad (1.4)$$

The criteria will exclude a large number of small-size clumps. However, the power law index of clump mass spectrum will not be changed by this (Kramer et al., 1998b).

Stutzki & Güsten (1990) used the method for an analysis of a C¹⁸O 2–1 map of the M17 SW cloud core and decomposed it into about 170 clumps. The method has been applied to different molecules and transitions by a number of other authors (Hobson, 1992; Johnen, 1992; Herberitz, 1992; Zimmermann, 1993; Hobson et al., 1994; Corneliussen, 1996; Kramer et al., 1996; Röhrig, 1996; Wiesemeyer et al., 1997; Heithausen et al., 1998; Kramer et al., 1998b; Simon et al., 2001;

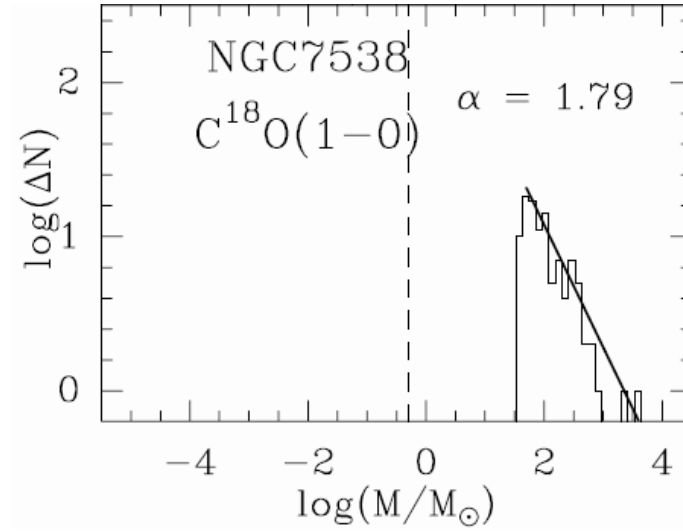


Figure 1.4: An example of a clump mass spectrum for clump mass spectra of NGC 7538. All spectra are fitted by a power law function $dN = dM \propto M^{-\alpha}$. The straight line represents the best linear fit over the range of masses spanned by the line. The resulting indices α is 1.79 in this case. The dashed line denotes the minimum possible mass limit, which is estimated by the resolution limits and the rms noise. The figure is adapted from the Fig. 6 in the paper by Kramer et al. (1998b).

Mookerjee et al., 2004). Below I will summarize some previous studies using *Gaussclumps*.

Kramer et al. (1998b) studied seven molecular clouds, L 1457, MCLD 126.6 + 24.5, NGC 1499SW, Orion B South, S 140, M 17 SW, and NGC 7538, using *Gaussclumps*. They discussed in details the reliability of the mass spectra derived by studying their dependence on the control parameters of the decomposition algorithm. Simon et al. (2001) presented a *Gaussclumps* study of the structure of four molecular clouds from the Milky Way Galactic ring survey in ^{13}CO 1–0 (see Fig. 1.5). Both studies found that the clump mass spectra are consistent with a power law, $dN = dM \propto M^{-\alpha}$, with $\alpha \sim 1.8$, independent of star formation activity. Fig. 1.4 presents an example of a clump mass spectrum.

1.3 Photon dominated regions

The cosmic cycle of star formation and stellar death controls the evolution of the ISM. The stars provide important feedback mechanisms for regulating star formation via stellar winds and radiation. Ultraviolet radiation from stars dis-

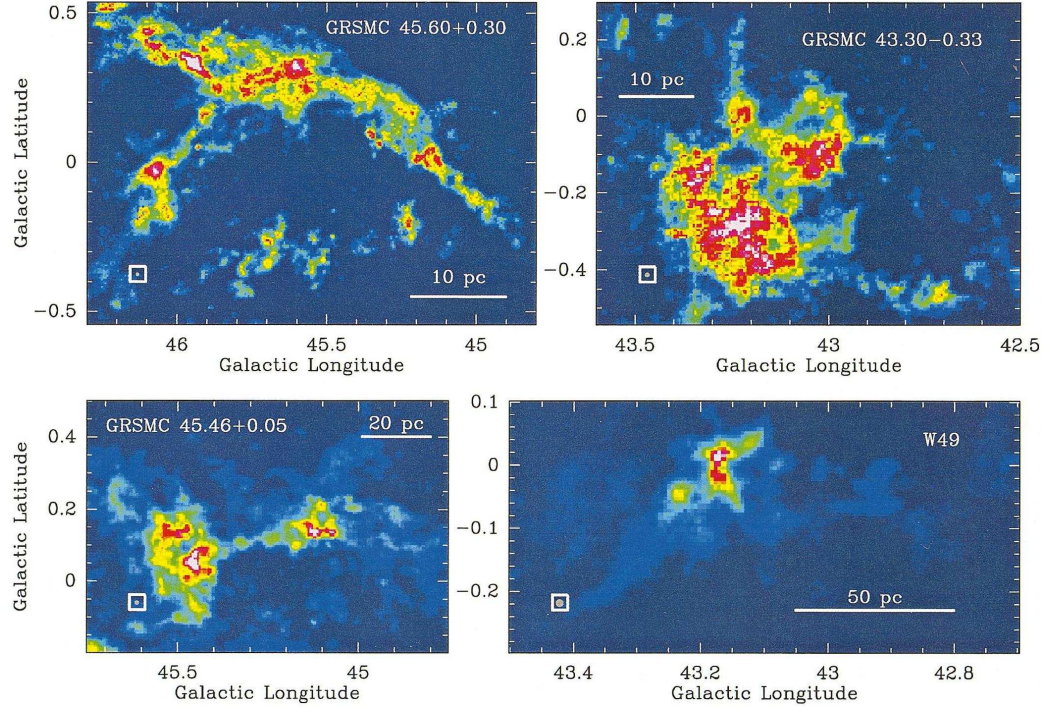


Figure 1.5: The GRS ^{13}CO intensity integrated over the velocity range relevant for emission from the individual cloud complexes. The beam size is indicated as a filled circle in the lower left corner of each panel. Top panels : Quiescent clouds; Bottom: Star-forming clouds. The figure is adapted from the Fig. 2 in the paper by Simon et al. (2001).

sociates molecules, ionizes, and heats the gas and the dust in photon dominated regions (PDRs). PDRs are the interface between the hot ionized medium and cold, dense molecular clouds. They are predominantly neutral, atomic and molecular regions where the physical and chemical processes are dominated by Far Ultraviolet (FUV) ($6.0 \text{ eV} < h\nu < 13.6 \text{ eV}$) radiation (Hollenbach & Tielens, 1997). Due to the clumpy nature of molecular clouds, PDRs are not strictly confined to the surface of the molecular clouds. For example, the extended $[\text{C II}]$ and $[\text{C I}]$ emission observed from all over the molecular clouds suggest formation of PDRs deep inside the molecular clouds, at the surfaces of clumps inundated with FUV photons escaping into the cloud (Mookerjea et al., 2006).

The study of photon dominated regions is the study of the effects of stellar far-ultraviolet photons on the structure, chemistry, thermal balance, and evolution of the neutral interstellar medium of galaxies.

Fig. 1.6 shows an example of one photon Dominated Region: NGC 3603.



Figure 1.6: One example of galactic photon dominated region: NGC 3603 observed by HST. Sher 25, the evolved blue supergiant, is to the upper right of center. The star has a unique circumstellar ring of glowing gas. A starburst cluster is near the center. A torrent of ionizing radiation and fast stellar winds from these massive stars has blown a large cavity around the cluster. The giant gaseous pillars to the right and lower left of the cluster are the evidence of the interaction of ionizing radiation with cold molecular-hydrogen cloud material. (<http://hubblesite.org/newscenter/archive/releases/1999/20/image/a/>).

1.3.1 PDR models

To study the chemical and physical structure of PDRs, this thesis uses the KOSMA - τ PDR model, a spherical PDR model developed by Störzer et al. (1996). Detailed description has been given by Störzer et al. (1996); Röllig et al. (2006, 2007). This model solves the coupled equations of energy balance (heating and cooling), chemical equilibrium, and radiative transfer, considering spherical clouds illuminated by an isotropic FUV field and cosmic rays. It computes the chemical and temperature structure of a spherical clump illuminated by an isotropic FUV radiation field and cosmic rays.

The PDR clumps are characterized by the incident FUV field intensity χ , given in units of the mean interstellar radiation field of Draine (Draine, 1978); the clump mass; and the average density of the clump. The emission from the models is calculated as a function of the hydrogen volume density, FUV radiation field and mass of the clumps (implicitly specifying the clump size). The model clump is assumed to have a power-law density profile of $n(r) \sim r^{-1.5}$ for $0.2 \leq r/r_{\text{cl}} \leq 1$ and $n(r) = \text{const.}$ for $r/r_{\text{cl}} \leq 0.2$. The surface density is about half of the mean clump density.

The PDR models are available on a regular grid with equidistant logarithmic steps. The FUV field covers the range from $10^0, 10^{0.5}, \dots, 10^{5.5}, 10^{6.0} G_0$; The clump surface densities range from $10^{2.0}, 10^{2.5}, \dots, 10^{5.5}, 10^{6.0} \text{ cm}^{-3}$; and the clump masses cover $10^{-3.0}, 10^{-2.5}, \dots, 10^{1.5}, 10^{2.0} M_{\odot}$.

1.4 Outline

This investigation of turbulence in dense interstellar medium and photon dominated regions unfolds over six chapters.

Chapter 2 summarizes the previous studies in the Perseus and Cepheus B molecular clouds. In Chapter 3 and Chapter 4, a structure analysis of maps of low $-J$ CO lines (^{12}CO 1–0, 3–2 and ^{13}CO 1–0 and 2–1) in the Perseus cloud is presented. The analysis uses both the Δ -variance method and *Gaussclumps*. The spatial structures of both line-integrated maps and velocity channel maps are studied. The spectral index β of the corresponding power spectrum is determined and its variation across the cloud and across the lines is also studied. I also use a three dimensional Gaussian clump decomposition, *Gaussclumps*, to identify clumps in the clouds and to investigate their properties.

Chapter 5 and 6 contain a photon dominated region study in IC 348, a subset of the Perseus cloud, and in Cepheus B. In Chapter 5, I present maps in [C I] at 492 GHz and ^{12}CO 4–3 combined with the FCRAO data of ^{12}CO 1–0, ^{13}CO 1–0 and far-infrared continuum data observed by HIRES/IRAS. To derive the physi-

cal parameters of the region, I analyze the line ratios of $[\text{C I}] \ ^3\text{P}_1\text{--}^3\text{P}_0/^{12}\text{CO } 4\text{--}3$, $[\text{C I}] \ ^3\text{P}_1\text{--}^3\text{P}_0/^{13}\text{CO } 1\text{--}0$, and $^{12}\text{CO } 4\text{--}3/^{12}\text{CO } 1\text{--}0$ using the following: a simple LTE analysis; analysis using the KOSMA - τ PDR model considering (a) a single spherical clump and (b) an ensemble of PDR clumps. The single spherical PDR model constrains the clump density and FUV field well, although it fails to explain the observed absolute line integrated intensities. The clumpy PDR models produce model line intensities which are in good agreement to within a factor of ~ 2 with the observed intensities. In Chapter 6, I study two cuts running through the interfaces into the main cloud and thus allow to trace several interface regions in Cepheus B. Particularly, we select two positions at the interfaces for a more detailed study. The studied frequency covers from 85 GHz to 272 GHz and includes 21 transitions of 11 molecules, such as HCN, HCO^+ , CN, CS and CCH. The aim of this study is to resolve the temperature, chemical, and excitation structure of the transition zone from the H II region to the dense molecular cloud in a PDR which is subject only to moderately strong UV fields.

A summary of all the results and an outlook of possible future work are presented in Chapter 7.

There are three appendices in this thesis work. Appendix A summarizes the basic of the LTE analysis. Appendix B is about a new atmospheric calibration routine. Different to the traditional calibration approach that determines the atmospheric transmission as an average over a representative section of each receiver band individually, that new atmospheric calibration scheme uses a single, free parameter, the precipitable water vapor (pwv) which is fitted to the observed atmospheric emission spectrum derived from HOT/COLD/SKY-measurements in the standard calibration cycle. Appendix C presents the introduction of a uniform observing script used at both the KOSMA and the NANTEN 2 observatories.

Chapter 2

Previous studies

To investigate turbulence in dense interstellar medium and the properties of photon dominated regions, I select two nearby star forming regions: the Perseus and Cepheus B molecular clouds. In this chapter, I present a brief summary of the previous studies in those two molecular clouds.

The Perseus molecular cloud is one of the best examples of the nearby active low- to intermediate-mass star forming regions and about 10° away from Taurus. It lies at a distance of 350 pc (Borgman & Blaauw, 1964; Herbig & Jones, 1983; Bachiller & Cernicharo, 1986) and is known to be related to the Perseus OB2 association (Bachiller & Cernicharo, 1986; Ungerechts & Thaddeus, 1987). There are an active star-forming region (NGC 1333), a young cluster (IC 348) and several dark clouds (L 1448, L 1445, Barnard 1, Barnard 1 EAST, Barnard 3 and Barnard 5) in this region.

The Cepheus molecular cloud is at a distance of 730 pc from the Sun (Blaauw, 1964). Cepheus B is the hottest ^{12}CO component in the CO maps (Sargent, 1979) and is located to the northwestern edge of the Cepheus molecular complex, near the Cepheus OB 3 association. The interface between the molecular cloud and the OB stars is clearly delineated by the optically visible H II region S 155, whose very sharp edges clearly indicate the presence of ionization fronts bounding the dust/molecular cloud. The OB association itself seems to be composed of two subgroups of different ages, with the youngest lying closer to the molecular cloud (Sargent, 1979). There are also indications that the younger subgroup has its origin near the Cepheus B cloud (Testi et al., 1995).

2.1 The Perseus molecular cloud

Ungerechts & Thaddeus (1987) carried a CO survey of the dark nebulae in Perseus, and they obtained the morphology and mass of the clouds. Bachiller & Cer-

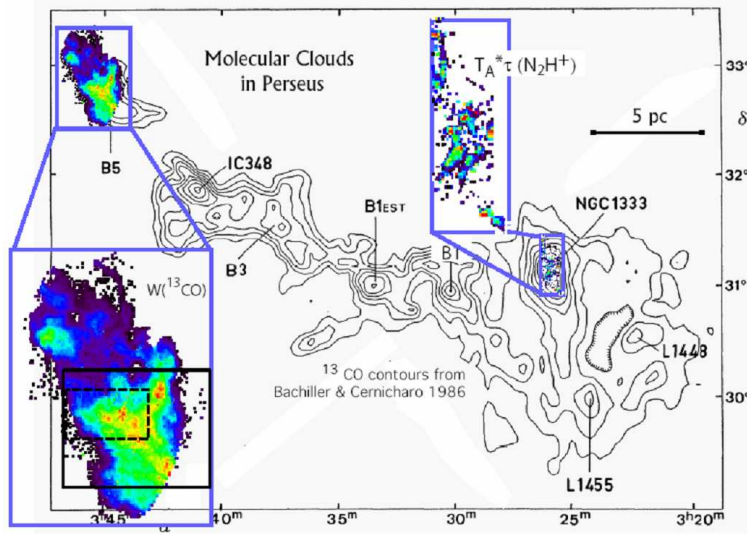


Figure 2.1: Map of the integrated intensity of the ^{13}CO 1–0 in the Perseus cloud (Bachiller & Cernicharo, 1986).

nicharo (1986) studied the relation between CO emission and visual extinction in the Perseus dark cloud (see Fig.2.1) and they determined the regression line of $N(^{13}\text{CO})$ on A_v for the range $1 \text{ mag} < A_v < 5 \text{ mag}$ $N(^{13}\text{CO}) = (2.5 \pm 0.5) 10^{15} (A_v - 0.8 \pm 0.4)$, where $N(^{13}\text{CO})$ is the LTE column density measured in cm^{-2} and A_v is the visual extinction in mag. From an extensive survey of the Perseus cloud in several molecular lines and star counts, Bachiller (1985) showed that the molecular cores in Perseus have densities and temperatures similar to those of the Taurus clumps (Bachiller & Cernicharo, 1984, 1986). 91 protostars and pre-stellar cores have been identified in a 3 square degree survey of the dust continuum at 850 and $450 \mu\text{m}$ made with the James Clerk Maxwell Telescope, JCMT (Hatchell et al., 2005). Imaging observations of the Perseus complex in molecular cloud tracers exhibit a wealth of substructure, such as cores, shells, filaments, outflows, jets, and a large-scale velocity gradient (Padoan et al., 1999). Padoan et al. (1999) compared the structure traced by ^{13}CO 1–0 observations to synthetic spectra and find that the motions in the cloud must be super-Alfvénic, with the exception of the B1 core, where Goodman et al. (1989) and Crutcher et al. (1993) detected a strong magnetic field. Padoan et al. (2003a) find that the structure function of the line-integrated ^{13}CO 1–0 map follows a power law for linear scales between 0.3–3 pc, and Padoan et al. (2003b) compared the velocity structure of Perseus to MHD simulations.

2.2 The Cepheus B molecular cloud

Sargent (1979) carried out a large-scale CO survey in Cepheus and found a clumpy and irregular structure, with several components having sizes of a few parsecs. The observations of these condensations imply that most are possible sites of recent star formation. The radio emission in the Cepheus B molecular cloud exhibits an extended arc-shaped structure (Felli et al., 1978) which surrounds the molecular cloud and smoothly decreases away from the molecular cloud. The physical association between the Cepheus B molecular cloud and the S 155 H II region was also confirmed by the H_2CO and recombination lines observations of Panagia & Thum (1981)). They deduced that the ionization front is moving into the molecular cloud at a velocity of about 2 km s^{-1} , while the ionized material is flowing away at $\sim 11 \text{ km s}^{-1}$.

In a first study with the KOSMA 3 m telescope, Beuther et al. (2000) mapped the Cepheus B cloud in 2–1 and 3–2 transitions of ^{12}CO , ^{13}CO , and C^{18}O at $2''$ resolution and used PDR models (Störzer et al., 2000) to explain the emission at four selected positions. The hotspot emission indicated the presence of shocks. Beuther et al. (2000) derived local volume densities of $\sim 2 \times 10^4 \text{ cm}^{-3}$, and average volume density less than 10^3 cm^{-3} and they drew a conclusion that Cepheus B is highly clumped with clumps filling only 2% to 4% by volume of the cloud. Then Mookerjee et al. (2006) observed fully-sampled maps of $[\text{C I}]$ at 492 GHz and ^{12}CO 4–3 in the Cepheus B cloud at resolution of $\sim 1''$ with the KOSMA 3 m telescope. They found an anti-correlation between C/CO and $\text{N}(\text{H}_2)$ which can be explained by considering an ensemble of clumps.

Fig 2.2 is a ^{12}CO 1–0 map in the Cepheus molecular cloud to indicate the location of the Cepheus B cloud in that cloud complex.

In the following chapters, I will present results of the structure analysis in the Perseus molecular cloud (Chapter 3 and Chapter 4) and PDR analysis in the IC 348 cloud (Chapter 5 and in the Cepheus B cloud (Chapter 6).

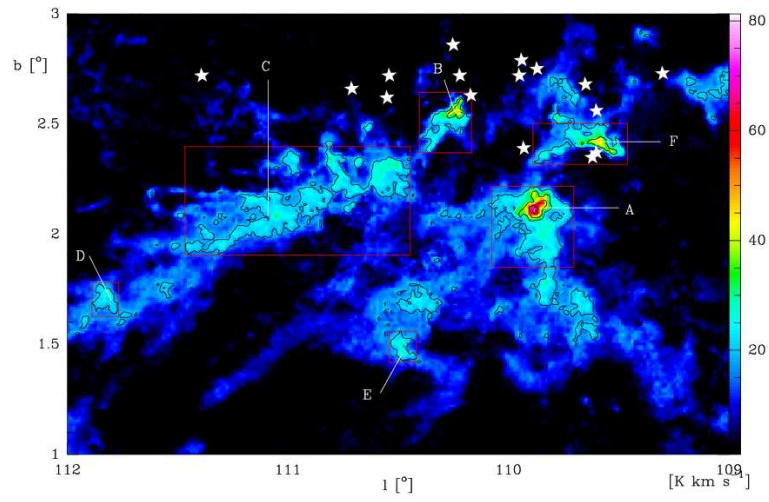


Figure 2.2: Integrated intensity map of ^{12}CO 1–0 in Cepheus (Masur, 2005). Cepheus A to Cepheus F are marked. The white stars denote the stars in Cepheus OB3 association.

Chapter 3

Large scale low - J CO survey of the Perseus cloud

In this chapter, I will present the results on the Δ -variance analysis in the Perseus molecular cloud. Mainly, the ^{12}CO 3–2 and ^{13}CO 2–1 data are used for the analysis. Optical extinction data from 2mass, ^{12}CO 1–0 and ^{13}CO 1–0 from FCRAO are also used as complementary data in the analysis.

Section 3.1 presents the details on the data observations. The general properties of the CO data sets are discussed in Section 3.2. Section 3.3 presents the results of the Δ -variance analysis in both integrated intensity maps and velocity channel maps. The discussion of the results and a summary of the Δ -variance analysis are given in Section 3.4 and 3.5, respectively. Part of this chapter has been published in *Astronomy and Astrophysics* in 2006 (Sun et al., 2006).

3.1 Observations

The observations were made from February to April, 2004 using the KOSMA 3m submillimeter telescope on Gornegrat, Switzerland, equipped with a dual-channel SIS receiver (Graf et al., 1998) and acousto optical spectrometers (Schieder et al., 1989). Main beam efficiencies and half power beamwidths (HPBW) are 68%, 130'' at 220 GHz and 70%, 82'' at 345 GHz. The HPBWs correspond to linear resolutions of 0.22 pc and 0.14 pc, where I adopted a distance of 350 pc (Borgman & Blaauw, 1964; Herbig & Jones, 1983; Bachiller & Cernicharo, 1986). All temperatures quoted in this paper are given on the main beam temperature scale.

The whole observation target is about 7.1 deg^2 that was divided into $10' \times 10'$ fields. Each map was observed using the on-the-fly (OTF) mode (Kramer et al., 1999) with a scanning speed of $7.5''/\text{s}$, a sampling rate of 4s, and a distance between

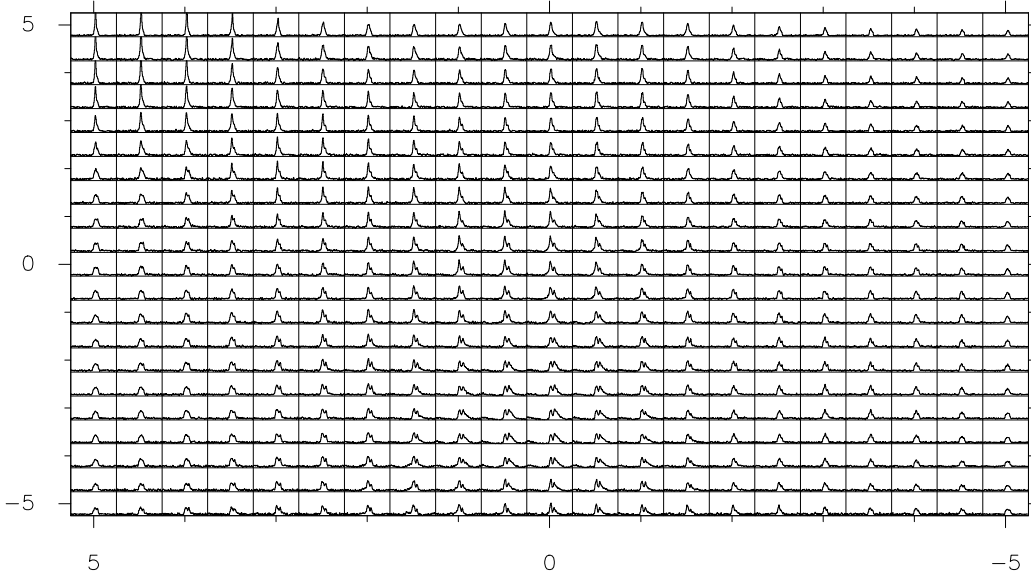


Figure 3.1: The ^{12}CO 3–2 spectra in one $10' \times 10'$ field.

successive scanning lines of $30''$, which results in an evenly sampled map of 21×21 points with a grid spacing of $30''$ (see Fig. 3.1). All the maps had the same center (03:26:00 +31:10:00 B1950) and I selected 3 emission-free off positions according to the ^{13}CO 1–0 map from the COMPLETE website.

The pointing was accurate to within $10''$ by regularly checking the standard pointing sources and planets. The channel spacing $\Delta\nu_{\text{ch}}$ and the average baseline noise rms of the spectra is 0.22 km s^{-1} , 0.48 K for ^{13}CO 2–1 and 0.29 km s^{-1} , 1.02 K for ^{12}CO 3–2.

Atmospheric calibration was done by measuring the atmospheric emission at the off position to derive the opacity (Hiyama, 1998). Spectra of the two frequency bands were calibrated separately. Sideband imbalances were corrected by using standard atmospheric models (Cernicharo, 1985). During the whole observation, I used DR 21, W3(OH) and the center of NGC 1333 as the calibration sources and the accuracy of the absolute intensity calibration is better than 15%. The basic observational parameters are listed in Table 3.1 and the dynamic range is in Table 3.2.

Table 3.1: Basic observation parameters. The first two columns indicate the line and transition frequency, followed by the main beam efficiency, B_{eff} . The telescope Half Power Beam Width (HPBW) (considering a distance of 350 pc, I converted the angle distance to distance) is listed in Column four. Column five is the observing grid and Column six is the number of observation points. Δv denotes the velocity resolution and T_{rms} is the average rms noise temperature per channel on a T_{mb} scale.

line	Frequency [GHz]	B_{eff}	HPBW ["]/pc	Grid ["]	Position	Δv [kms ⁻¹]	T_{rms} [K]
¹³ CO 2-1	220	0.68	130/0.22	30	96451	0.23	0.48
¹² CO 3-2	345	0.70	82/0.14	30	96451	0.29	1.02

Table 3.2: Dynamic range. Column one and two indicate the line and mapped area (I adopted the 350 pc as the distance) followed by the ratios of mapped area over beam size, the peak temperature over the average rms noise temperature and the σ . The σ is defined: $\sigma = \sqrt{N} \Delta V_{res} T_{rms}$. And the velocity range is from 0kms⁻¹ to 16kms⁻¹.

line	Mapped area [degree ²]/[pc ²]	Dynamic range		σ [Kkms ⁻¹]
		Mapped area/Beam ²	Peak temp./rms	
¹³ CO 2-1	7.10/264.67	5445	28.6	0.7
¹² CO 3-2	7.10/264.67	13685	41.6	1.7

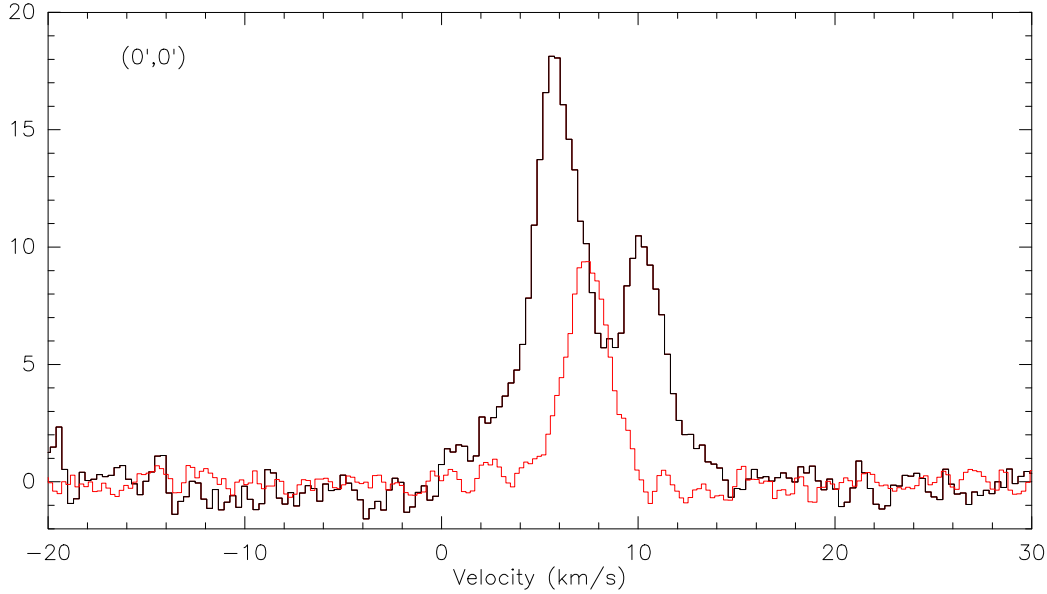


Figure 3.2: The spectra of ^{12}CO 3–2 (black) and ^{13}CO 2–1 (red or grey in black and white) at the center of the observed map.

3.2 Data Sets

3.2.1 Integrated intensity maps

Fig. 3.2 presents the ^{12}CO 3–2 and ^{13}CO 2–1 spectra of the center (0,0) position in main beam scales. The emission of the ^{12}CO 3–2 ranges from ~ 0 to 14 km s^{-1} ; and it is about from 4 to 12 km s^{-1} for ^{13}CO 2–1 spectra. The peak temperature is about 18 and 9 K for the ^{12}CO 3–2 and ^{13}CO 2–1 spectra, respectively. A dip in the ^{12}CO 3–2 spectrum lies at the peak of the ^{13}CO 2–1 spectrum. This indicates self-absorption for the ^{12}CO 3–2 spectrum.

The maps of velocity integrated ^{13}CO 2–1 and ^{12}CO 3–2 emission (Figs. 3.3,3.4) show the Perseus region, viz. the well known string of molecular clouds running over $\sim 30 \text{ pc}$ projected distance from NGC 1333 and L 1455 in the west to B 1, B 1 East, and B 3 in the center, and to IC 348 and B ,5 in the east (cf. Bachiller & Cernicharo, 1986; Ungerechts & Thaddeus, 1987). Generally, there is a good correlation between ^{12}CO 3–2 and ^{13}CO 2–1 integrated intensities.

Two major molecular clouds dominate the map: NGC 1333 and IC 348. The integrated intensity is strongest in NGC 1333 in ^{12}CO 3–2 and there are two peaks in it: one is around $(0',0')$, the other lies about $(5',5')$. The peak intensity of IC 348 is around $(195',45')$ and the emission extends in the north-east direction following the filament. There are weaker peaks in B 1, B 1 EAST, B 3 and B 5, while the

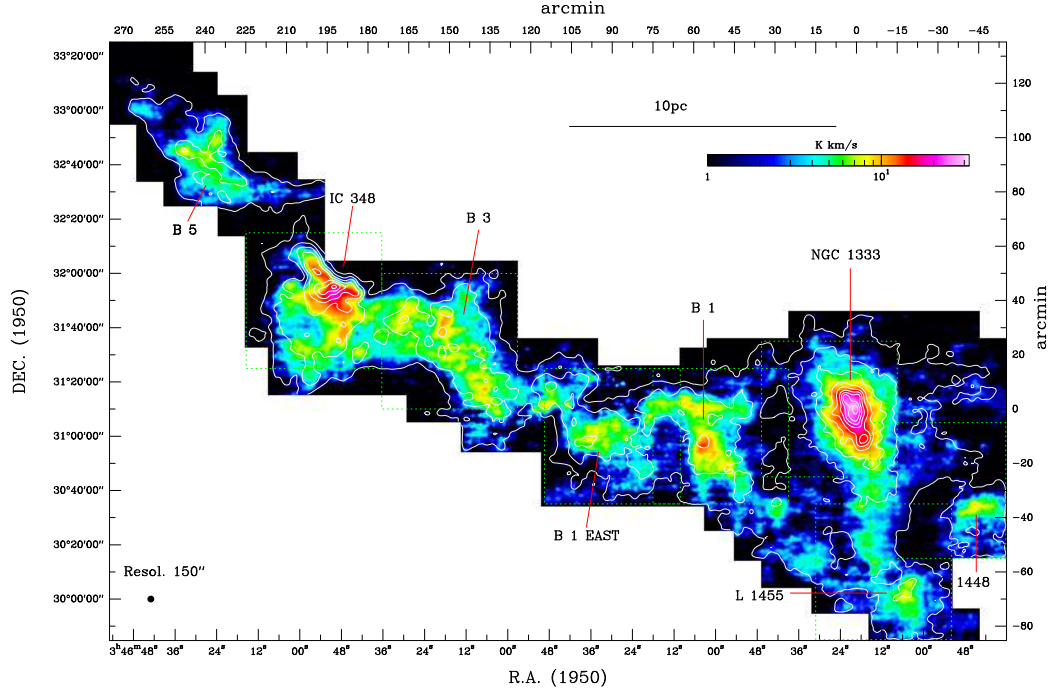


Figure 3.3: The Perseus molecular cloud complex. KOSMA maps of integrated intensities of ^{13}CO 2–1 (colors) and ^{12}CO 3–2 (contours) at $150''$ resolution. The integration interval is $0\text{--}16\text{ km s}^{-1}$. Colors run from 1 K km s^{-1} ($\sim 1\sigma$) to 32 K km s^{-1} . Contours range from 6.6 K km s^{-1} ($\sim 3\sigma$) to 83 K km s^{-1} in steps of 9 K km s^{-1} . The (0,0) position corresponds to $\text{RA}=03:26:00$, $\text{DEC}=+31:10:00$ (B1950). Seven sub-regions are marked by dotted square boxes of $50' \times 50'$.

weakest emissions are in L 1448 and L 1455.

In the next section, I compare the statistical properties of the structure seen in the entire Perseus map with the structure seen in individual regions. For this, I defined seven boxes of $50' \times 50'$ which roughly coincide with the known molecular clouds (cf. Fig. 3.3).

Figure 3.4 shows an overlay of integrated ^{13}CO 2–1 intensities and a map of optical extinctions (Goodman, 2004; Alves et al., 2005), at $2.5'$ and $5'$ resolution, respectively. The ^{13}CO map covers all regions above 7 mag and $\sim 70\%$ of the regions above 3 mag. A linear least squares fit to a plot of A_V vs. ^{13}CO 2–1 results in a correlation coefficient of 0.76. The region mapped in ^{13}CO has a mass of $1.7 \times 10^4 M_\odot$ using the A_V data and the canonical conversion factor $[\text{H}_2]/[A_V] = 9.36 \times 10^{20}\text{ cm}^{-2}\text{ mag}^{-1}$ (Bohlin et al., 1978).

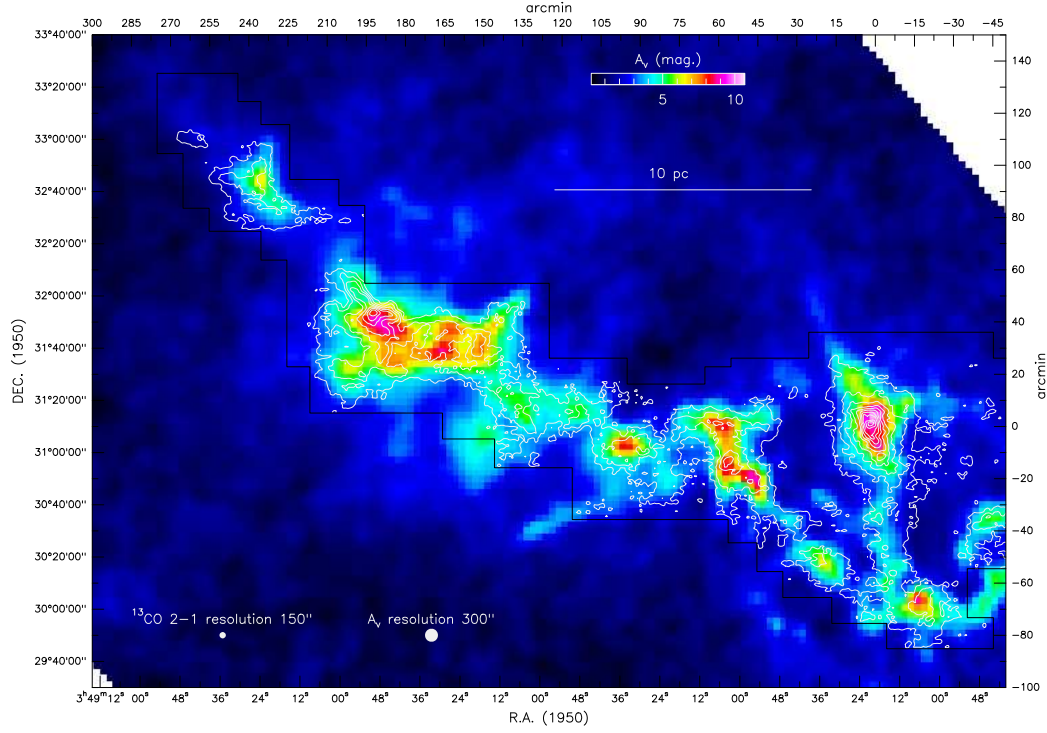


Figure 3.4: Overlay of ^{13}CO 2–1 integrated intensities (contours) with a map of optical extinctions in colors (Goodman, 2004; Alves et al., 2005). Contours range from 2.7 Kkms^{-1} (3σ) to 32 Kkms^{-1} by 3 Kkms^{-1} . Colors range from $A_V = 1 \text{ mag}$ to 11 mag . Resolutions are $2.5'$ for ^{13}CO and $5'$ for A_V . A polygon marks the boundary of the ^{13}CO map.

3.2.2 Velocity structure

Maps of ^{13}CO 2–1 emission integrated over small velocity intervals (Fig. 3.5) illustrate the filamentary structure of the Perseus clouds. The channel maps show the well-known velocity gradient between the western sources, e.g. NGC 1333 at $\sim 7 \text{ km s}^{-1}$, and the eastern sources, e.g. IC 348 at $\sim 9 \text{ km s}^{-1}$. The channel map integrated between 5 and 6 km s^{-1} exhibits two filaments originating at L 1455, one runs north to NGC 1333, the second runs north-east to B 1. I will discuss the structural properties of individual velocity channel maps in the next sections.

To study the statistics of the velocity field, I start with the distribution of the line widths across the map. Since many spectra show deviations from a Gaussian line shape, I use the equivalent line width $\Delta v_{\text{eq}} = \int T dv / T_{\text{peak}}$ as a measure of the velocity dispersion along individual lines of sight. Figure 3.6 shows the mean equivalent line widths and their scatter for the seven sub-regions shown in Figure 3.3.

The mean ^{12}CO widths vary significantly between 2.2 km s^{-1} in the quiescent dark cloud L 1455 and 3.8 km s^{-1} in the active star forming region NGC 1333. In contrast, the ^{13}CO widths are smaller and show only a weak trend around $\sim 2 \text{ km s}^{-1}$.

Several positions in L 1455, but also in e.g. IC 348, show small line widths of $\sim 1 \text{ km s}^{-1}$, only a factor of ~ 8 –11 larger than the CO thermal line width, which is $\approx 0.16 \text{ km s}^{-1}$ for a kinetic temperature of 10 K as was found for the bulk of the gas in Perseus by Bachiller & Cernicharo (1986).

3.3 The Δ -variance analysis

In this section, I statistically quantify the spatial structure observed in the maps, both for the overall structure and for the structure of individual regions within the Perseus molecular cloud. I measure the spectral index of the power spectrum using the Δ -variance analysis, a wavelet convolution technique. I analyze the new CO data and compare the results with an equivalent analysis of the FCRAO ^{12}CO 1–0, ^{13}CO 1–0 maps and the A_V Perseus map obtained from 2MASS (Two Micron All Sky Survey) by the COMPLETE team (Goodman, 2004; Alves et al., 2005).

In the KOSMA data I noticed that the noise does not follow a pure white noise behaviour, but it is //colored// due to artifacts from instrumental drifts, baseline ripples, OTF stripes etc. This has to be taken into account when deriving the cloud spectral index β from the Δ -variance spectra.

Thus I measured the spectral index of the colored noise d_{noise} by analyzing maps created from velocity channels which do not see any line emission but which cover the same velocity width as the actual molecular line maps. The result is

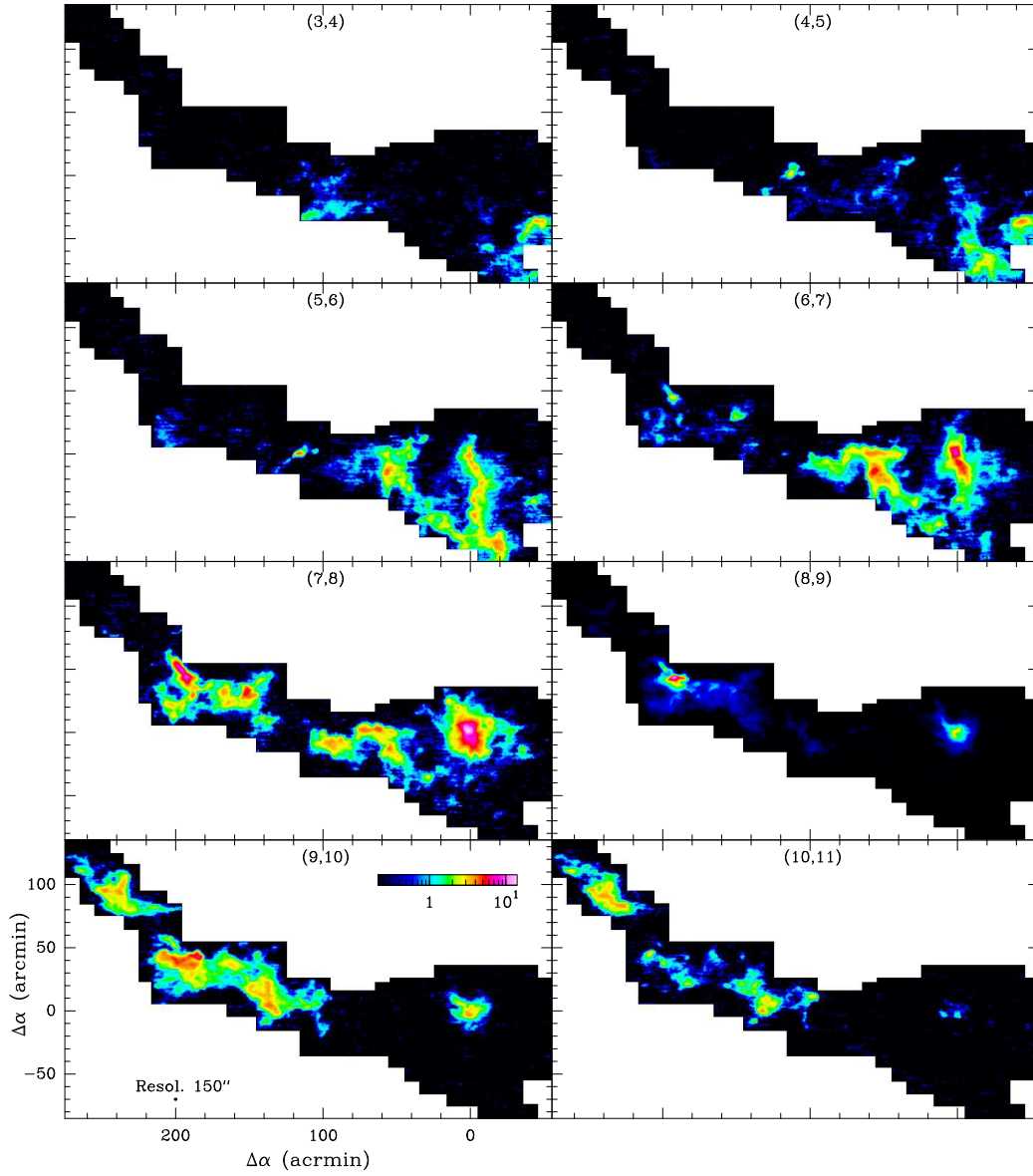


Figure 3.5: ^{13}CO 2–1 velocity channel maps of the Perseus region. The velocity range runs from 3 km s^{-1} to 11 km s^{-1} with an interval of 1 km s^{-1} which is indicated on the top of each plot. The intensities are plotted from 0.7 K km s^{-1} ($\sim 1 \sigma$) to 15 K km s^{-1} .

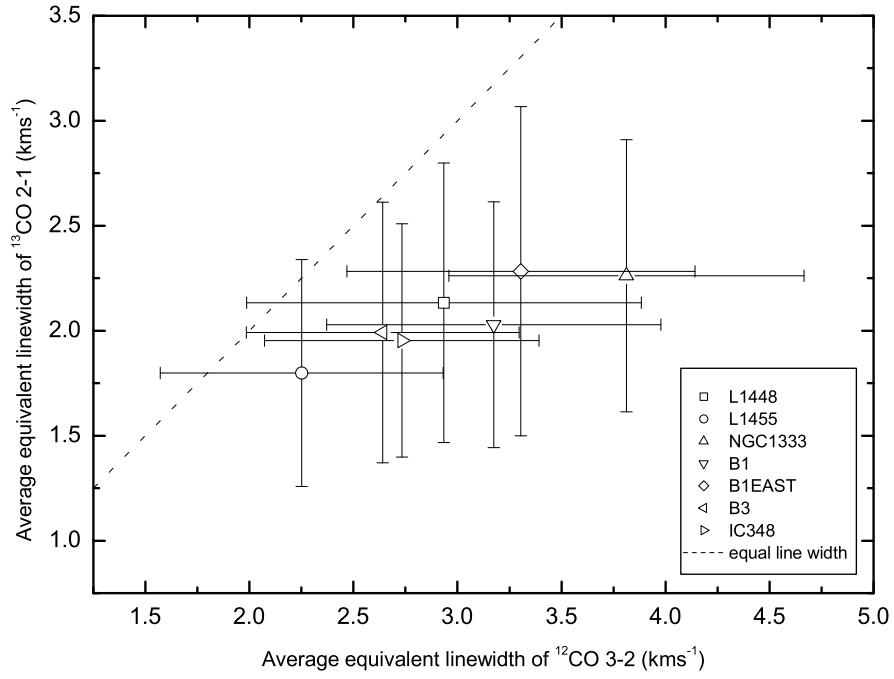


Figure 3.6: Mean and rms of the equivalent line widths Δv_{eq} of the ^{12}CO 3–2 and ^{13}CO 2–1 spectra for the observed positions of the seven $50' \times 50'$ sub regions (Fig. 3.3). The dashed line delineates equal widths in ^{12}CO and ^{13}CO . The error bars indicate the difference between the minimum/maximum and the mean values.

shown in Fig. 3.7. I find a nearly constant index $d_{\text{noise}} \approx -1.5$ for all off-line channels at scales between about 1 and 6'. At larger lags, the noise deviates from the $\beta = 0.5$ behaviour, but this does not affect the structure analysis as the absolute noise contribution is negligible there.

For the FCRAO data and the COMPLETE A_V map I have no emission-free channels available so that I cannot perform an equivalent noise fit there. The Δ -variance at small lags shows however no indications for a deviation from the pure white noise behaviour, so that I stick to $d_{\text{noise}} = -2$ for the fit of these data.

3.3.1 Integrated intensity maps

Figure 3.8 compares the Δ -variance spectra of the different integrated intensity maps for the entire region mapped with KOSMA (see Fig. 3.3)¹. When corrected for the observational noise, the Δ -variance spectra of all maps follow power laws between the linear resolution of the surveys and about 3 pc (Table 3.3). The good agreement of the spectral indices obtained from the different CO data is remarkable. They cover only the narrow range between 3.03 ± 0.14 and 3.15 ± 0.04 . In contrast, the extinction data result in a significantly lower index. This indicates a more filamentary structure in A_V . When I actually compare the A_V map with ^{13}CO 2–1 data smoothed to the same resolution, it is also noticeable by eye that the A_V map looks more clumpy or filamentary than the ^{13}CO map. This indicates that ^{13}CO does not trace all details of the cloud structure, but rather measures the more extended, and thus more smoothly distributed gas.

All Δ -variance spectra show a turnover at about 3 pc. To test whether this peak measures the real width of the Perseus cloud or whether it is produced by the elongated shape of the CO maps, I have repeated the Δ -variance analysis for the A_V data of the entire region shown in Figure 3.4. In this case I find almost the same spectrum below 3 pc, but instead of a turnover only a slight decrease of the slope at larger lags. Thus I have to conclude that the Δ -variance spectra of the CO maps at scales beyond 3 pc are dominated by edge effects, due to the shape of the maps, so that these scales should be excluded from the analysis. In Figure 3.8 I compare only spectra for the same region, i.e. the Δ -variance spectra of the A_V data of the region also mapped with KOSMA.

As it is not guaranteed that the structure of the overall region is representative for individual components, I have also applied the Δ -variance analysis to the KOSMA data of the individual clouds contained in the seven $50' \times 50'$ subregions shown in Fig. 3.3. The results of the power-law fits to the Δ -variance spectra are listed in Table 3.4. They differ significantly between the individual regions. The active star-forming region NGC 1333 shows the highest spectral indices in

¹Note that the area covered by the FCRAO is slightly smaller than that observed with KOSMA.

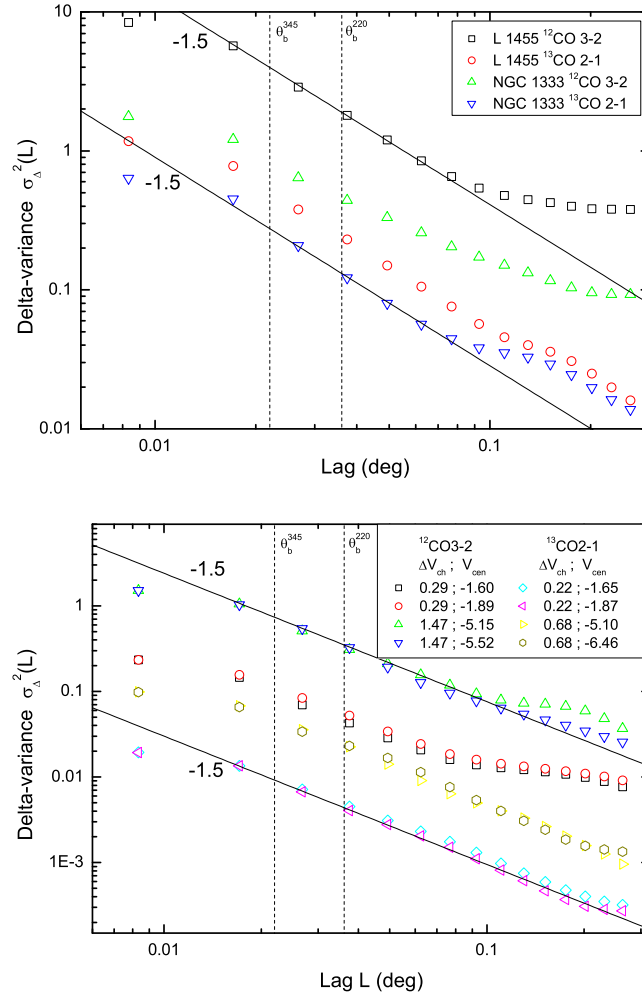


Figure 3.7: Δ -variance analysis of the off-line channel maps. In the upper plot a velocity span corresponding to the integrated intensity maps is used. The two regions representing opposite extremes in the structural behaviour, NGC 1333 and L1455, show about the same spectral index of the colored noise in both transitions for small lags. In the lower plot, the influence of different velocity spans, as used in the velocity channel analysis (Sect. 3.3.2), is studied for L1455. The colored noise index d_{noise} is nearly constant independent of species, transition, velocity range Δv_{ch} , and center velocity v_{cen} .

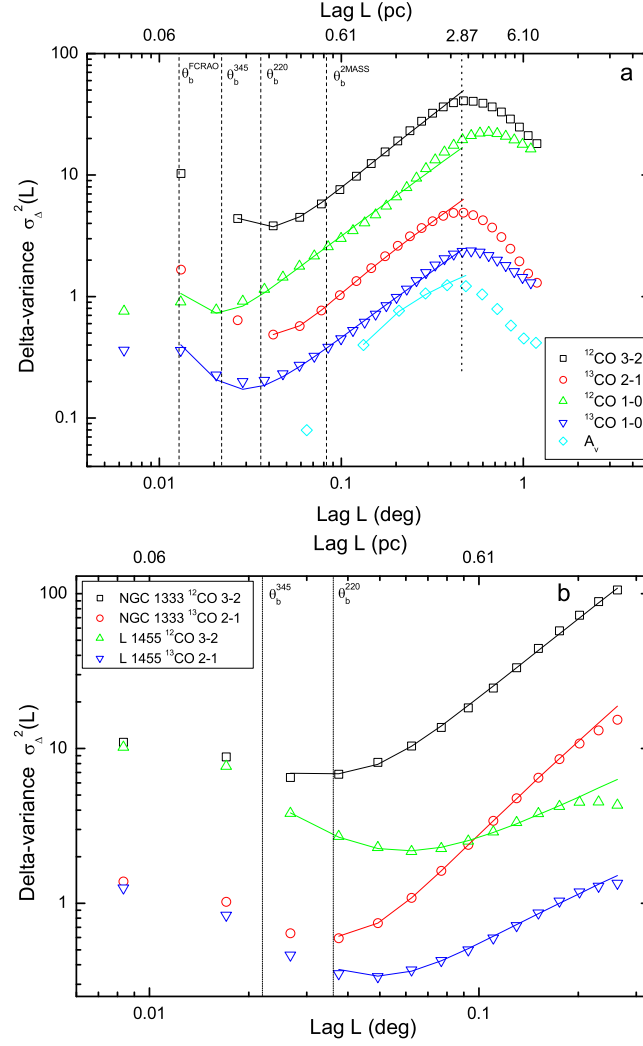


Figure 3.8: Δ -variance spectra of integrated intensities. **a)** Spectra obtained from the CO maps and the A_V data of the region mapped with the KOSMA telescope. **b)** Spectra of integrated intensity maps of two $50' \times 50'$ sub-regions: NGC 1333 and L 1455. Power-law fits to the data corrected for noise and beam-blurring are indicated as solid lines.

Table 3.3: Results of the Δ -variance analysis of the integrated CO maps and the A_V data for the region mapped with KOSMA (Fig. 3.3).

Transition	Telescope	resol. [']	Fit Range [']	β
A_V	2MASS	5	5.0-28	2.55 ± 0.02
$^{13}\text{CO } 1-0$	FCRAO	0.77	0.8-28	3.09 ± 0.09
$^{12}\text{CO } 1-0$	FCRAO	0.77	0.8-28	3.08 ± 0.04
$^{13}\text{CO } 2-1$	KOSMA	2.17	2.2-28	3.03 ± 0.14
$^{12}\text{CO } 3-2$	KOSMA	1.37	1.4-28	3.15 ± 0.04

Table 3.4: Results of the Δ -variance analysis of the KOSMA data for seven $50' \times 50'$ sub-regions of the cloud (Figure 3.3). The spectral indices β were fitted in the size range 2.2-14' for the $^{13}\text{CO } 2-1$ and in the size range 1.4-14' for the $^{12}\text{CO } 3-2$ data.

Region	$\beta(^{13}\text{CO } 2-1)$	$\beta(^{12}\text{CO } 3-2)$
L 1448	2.96 ± 0.42	3.41 ± 0.16
L 1455	2.86 ± 0.09	2.85 ± 0.30
NGC 1333	3.76 ± 0.48	3.52 ± 0.11
B 1	3.14 ± 0.29	3.00 ± 0.20
B 1 EAST	3.16 ± 0.09	3.39 ± 0.09
B 3	3.36 ± 0.09	3.14 ± 0.06
IC 348	2.71 ± 0.42	3.06 ± 0.24

both transitions. The low end of the spectral index range is formed by the dark cloud L 1455 together with the environment of the young cluster IC 348. The Δ -variance spectra of the two extreme examples NGC 1333 and L 1455 are shown in Fig. 3.8b. Starting from the same noise values at small scales the spectra of the two regions show an increasing difference in the relative amount of structure at large scales reflected by the strongly deviating spectral indices. Altogether, I find high indices as characteristics of large condensations for the regions with active star formation and lower indices quantifying more filamentary structure for dark clouds, but IC 348 as an exception to this rule, showing also a very filamentary structure.

3.3.2 Velocity channel maps

When performing the Δ -variance analysis not only for maps of integrated intensities, but for individual channel maps I obtain additional information on the velocity structure of the cloud. In the velocity channel analysis (VCA), introduced by

Lazarian & Pogosyan (2000), the change of the spectral index of channel maps as a function of the channel width was used to simultaneously determine the scaling behavior of the density and the velocity fields from a single data cube of line data. Here I conduct such a study for the KOSMA CO data.

I start with the analysis of individual channel maps as they are provided by the channel spacing Δv_{ch} of the backends (cf. §3.1). For all channel maps I perform the Δ -variance analysis and fit power laws to the measured structure for all lags between the telescope beam size and the maximum scale resolved by the Δ -variance (about 1/4 of the map size). As a result I get the power-law index as a function of the channel velocity, a curve which I call *index spectrum*. As an example I show the index spectrum obtained for the ^{13}CO 2–1 data in the L 1455 region in Fig. 3.9. The spectrum is always truncated at velocities where the average line temperature is lower than the noise rms.

The overall structure of the index spectrum is similar to the line profile. The largest spectral indices are found at velocities close to the average line peak. This may implicate that extended smooth structure provides the major contribution to the overall emission, while the velocity tail of this structure is formed by small-scale features. However, the indices show an asymmetric behavior with respect to the blue and the red wing. The indices drop steeply to a noise-dominated value at the red wing, while the blue wing shows only a very shallow decay. Even at the noise limit, noticeable structure is detected in the channel maps there.

For the full velocity channel analysis, the index spectrum has to be computed for different velocity channel widths (Lazarian & Pogosyan, 2000). Thus I have binned the data to averages of three, five, and seven velocity channels and computed the index spectra for these binned channel maps. In Fig. 3.10 I show the results for three examples: IC 348, NGC 1333 and L 1455. For the sake of clarity the error bars of the index spectra were omitted in these plots.

The overall structure of the index spectra is similar to Fig. 3.9 for all sources, transitions and channel widths. In most cases I find the asymmetry of a shallower blue wing relative to the red wing. When looking at narrow velocity channels, I find a dip in the centre of the index spectrum for the ^{12}CO 3–2 data of NGC 1333 and L 1455. A slight indication of such a dip is also present in the ^{12}CO 3–2 data of IC348 and in the ^{13}CO 2–1 data of NGC 1333. This could be due to optical depth effects. Because I see self-absorption in quite a few positions, when I check individual spectra in those regions. This leads to a more filamentary appearance of the central channel maps reflected by this dip in the index spectra. It is interesting to notice that the VCA is more sensitive to self-absorption than the average spectrum.

When increasing the channel width by binning, the self-absorption dip is smoothed out, so that the resulting index spectra peak again close to the peak velocity of the line temperature. In all situations where the self absorption is negligible, the in-

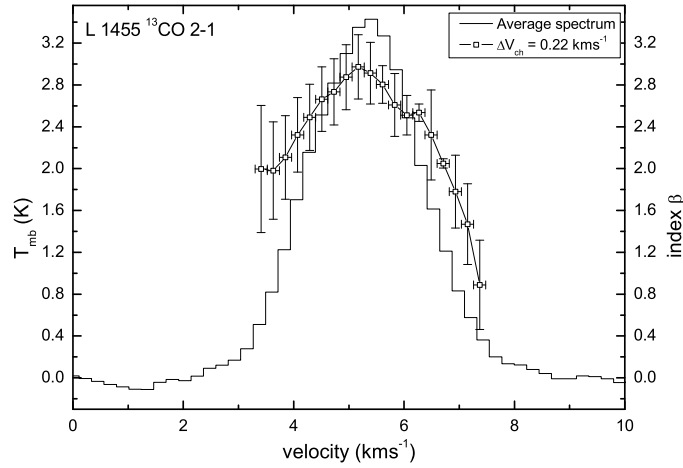


Figure 3.9: Comparison of the index spectrum of the ^{13}CO 2–1 data in L 1455 with the average line profile. The index spectrum is created by power-law fits to the Δ -variance spectrum of individual channel maps ($\Delta v_{\text{ch}} = 0.22 \text{ km s}^{-1}$). The vertical error bars represent the uncertainty of the fit. The horizontal error bars indicate the velocity channel width.

indices for the line core channels are almost independent from the channel width. The indices for the line integrated intensities always fall slightly below the peak indices, as they represent an average which is typically dominated by the line cores.

In the red line wings, most indices remain approximately constant when increasing the velocity width, except for the largest bin width where the contribution from the core leads to an observable increase. In the blue wing, I find a monotonic growth of the spectral indices with the channel width for both tracers in all three regions. The additional peak at 2 km s^{-1} visible in the ^{12}CO 3–2 data of NGC 1333 stems from a separate dark cloud which is also contained in the NGC 1333 map.

Figure 3.11 summarizes the relation between the spectral indices and the velocity channel width. In Fig. 3.11a I plot the average spectral index over the line as a function of the channel width for the six data sets presented in Fig. 3.10. Figure 3.11b contains the analysis when restricted to a 2 km s^{-1} window in the blue line wings. The error bars contain the standard deviation of the index variation across the line and the fit errors. They are necessarily large because of the systematic variation of indices over the velocity range. In contrast to similar analysis by Dickey et al. (2001); Stanimirović & Lazarian (2001) I find no significant systematic variation of the mean line index as a function of channel width (Figure 3.11a).

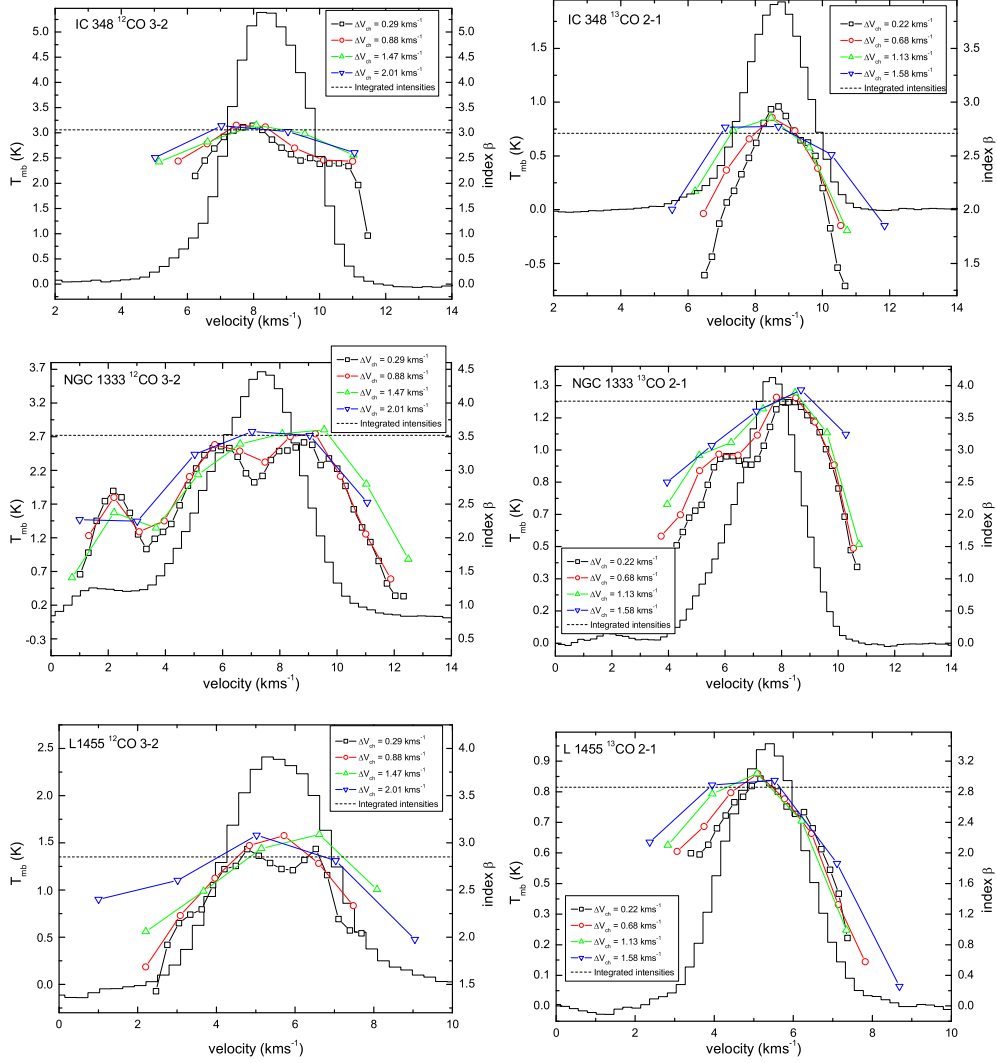


Figure 3.10: Comparison of the index spectra obtained for different velocity channel widths with the average line profile. The upper plots show the results for IC 348, the central plot NGC 1333 and the lower plot L 1455. For the left column I used the ^{12}CO 3–2 data, the right column represents the ^{13}CO 2–1 data. The different symbols indicate the results from different velocity channel widths. The dashed lines represents the index of the integrated intensity maps.

In contrast to the average of the index spectrum I find a continuous increase of the spectral index with the channel width when restricting the analysis to the blue wing (Figure 3.11b). The average index steepens from about 2.8 to about 3.1 in the ^{12}CO 3–2 maps and from about 2.4 to about 2.8 in the ^{13}CO 2–1 maps. As discussed above I find no systematic trend in the red wings. This indicates that the average spectral index taken over the full line profile provides no measure for the velocity structure in the CO maps while the peculiar behaviour in the blue wings needs further investigation.

3.4 Discussion

3.4.1 Integrated intensity maps

Besides the Δ -variance, other tools have been used to characterize interstellar cloud structure. The second-order structure function for an observable $s(\vec{r})$ is $S_2 = \langle |s(\vec{r}) - s(\vec{r} + \delta\vec{r})|^2 \rangle_{\vec{r}}$ which is treated as a function of the absolute value of the increment $|\delta\vec{r}|$ (Elmegreen & Scalo, 2004). Padoan et al. (2003a) computed the structure function of the integrated intensity map of ^{13}CO 1–0 in Perseus. A power-law fit to $S_2 \propto \delta r^\zeta$ over a range of 0.3 to 3 pc provided an index ζ of 0.83. The index of the structure function is related to the power spectral index by $\zeta = \beta - 2$ for $2 < \beta < 4$ (Stutzki et al., 1998) resulting in $\beta = 2.83$. This result of Padoan et al. (2003a) agrees within the error bars with the indices found by the Δ -variance analysis of the Perseus maps of integrated CO intensities over almost the same linear range (see Table 3.3).

However, the Δ -variance spectra of individual regions show significant variations of the spectral index as discussed above. For ^{13}CO 2–1, these span the range between $\beta = 2.86$ in L1455 and 3.76 in NGC 1333 (Table 3.4). The analysis of different sub-sets in molecular cloud complexes thus provides additional and complementary information on the structure of the cloud complex.

3.4.2 Velocity channel maps

The velocity channel analysis, was used previously by Dickey et al. (2001) to study H I maps of two regions in the 4th Galactic quadrant. One of the regions is rich in warm H I gas, the other is rich in cool H I gas. For the warm gas, Dickey et al. (2001) find a systematic increase of the mean index with velocity channel width. The cold gas at lower latitudes behaves differently and shows rather constant indices of 2.7–3.1.

The latter results resemble the outcome of the VCA of the ^{12}CO and ^{13}CO channel maps in Perseus presented above. I find similar indices for the velocity

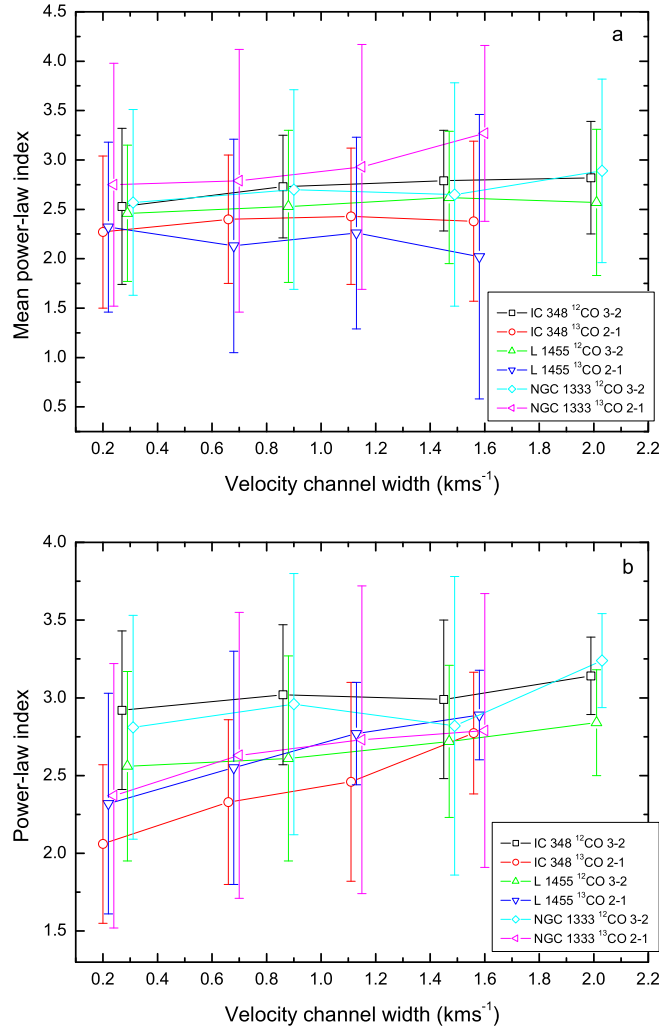


Figure 3.11: Average spectral indices of the channel maps as a function of the channel width. **a)** shows the average over the full line width. **b)** represents only the indices in the blue wing components. The line wing components are centered at 5 km s⁻¹ for NGC 1333, at 4 km s⁻¹ for L 1455, and at 7 km s⁻¹ for IC 348. The error bars contain the fit error and the standard deviation of the indices within the considered velocity range. To avoid overlapping error bars in the plot, I have shifted the points for IC 348 and NGC 1333 by ± 0.02 km s⁻¹ relative to their actual position.

integrated maps of the full region (cf. Table 3.3) and the CO data show no significant variation of the index with velocity channel width when averaged over all velocity bins (Figure 3.11a). The indices stay relatively constant. Since the bulk of the molecular gas traced by CO is even colder than cold H I gas, these results suggest a sequence of a reduced dependence of the spectral index of the channel maps on the bin widths from the warm to the cold ISM. The constancy of the average spectral index could also be explained by optical depth effects. Lazarian & Pogosyan (2004) have shown that absorption can lead to an effective slice broadening, which leads in extreme cases to slice indices that become independent from the actual channel width.

Studying the spectral index of individual velocity bins of the CO data across the line profile (Fig. 3.10), I find that the power-law indices increase with the velocity channel width in the blue wing (Fig. 3.11b) while staying rather constant in the red wing. No corresponding analysis was conducted for the H I data by Dickey et al. (2001). One possibility to explain the asymmetry between the blue and red wings might be a shock expansion of the CO gas in Perseus. Sancisi (1974) found an expanding shell of neutral hydrogen which was created by a supernova in the Per OB2 association a few 10^6 years ago. At the location of the molecular cloud complex, the expansion is directed away from the Sun. Most of the associated molecular gas has been swept up by the shock, but pillar-like filaments have been left at the backside of the shock. They are visible in the channel maps (Fig. 3.5) and produce the velocity dependence seen in the VCA of the blue line wings, i.e. the increase of indices with size of the velocity bin because of a gradual increase of large scale contributions across the line wing. I illustrate this scenario in Fig. 3.12.

The quantitative results from the velocity channel analysis can be interpreted in terms of the power spectrum of the velocity structure. Lazarian & Pogosyan (2000) showed that the spectrum of velocity slices as a function of the velocity channel width is determined by the power spectral indices of the density structure β and the velocity structure m . They obtain different regimes for shallow ($\beta < 3$) and steep ($\beta > 3$) density power spectra:

$$P(k) \propto \begin{cases} k^{-\beta + \frac{m-3}{2}}, & \text{thin slices,} \\ k^{-\beta}, & \text{thick slices,} \\ k^{-\beta}, & \text{very thick slices;} \end{cases} \quad (\beta < 3)$$

$$P(k) \propto \begin{cases} k^{-\frac{9-m}{2}}, & \text{thin slices,} \\ k^{-\frac{3+m}{2}}, & \text{thick slices,} \\ k^{-\beta}, & \text{very thick slices.} \end{cases} \quad (\beta > 3)$$

Thin slices have a velocity width less than the local velocity dispersion at the studied scale; thick slices have a width larger than the velocity dispersion and very

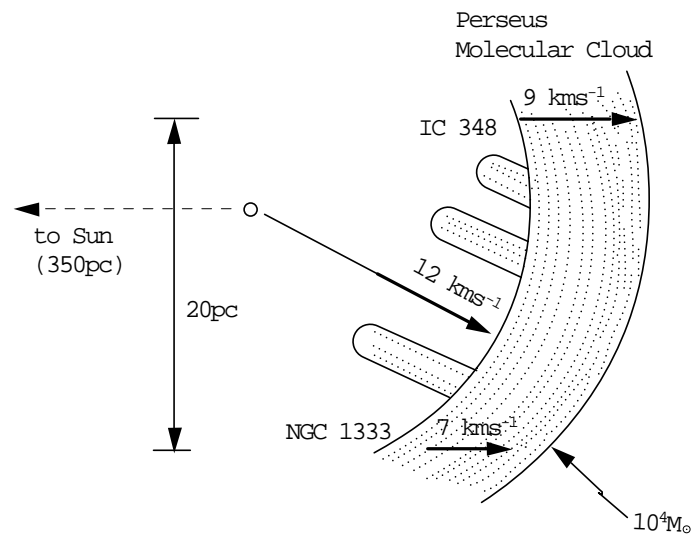


Figure 3.12: Sketch adopted from Fig. 3 of Sancisi (1974) illustrating the spatial arrangement and motion of the Perseus cloud complex. The gas is swept up by a shock expansion with 12 km s^{-1} . Due to the overall curvature, the line-of-sight velocity is 9 km s^{-1} for IC 348, but only 7 km s^{-1} for NGC1333. The diameter of the cloud is $\sim 20 \text{ pc}$. Pillar-like structures are left at lower velocities as remainders of high-density regions which were not accelerated to the same velocity.

thick slices essentially correspond to the integrated maps (Lazarian & Pogosyan, 2000). I can assume that a single channel of the data corresponds to thin slices as they are much narrower than any observed line width. I use β from the integrated maps and the index measured in the single channels to derive m . From the indices obtained by averaging over the full line profile (Fig. 3.11a), I obtain m values of 3.9 ± 1.6 , 3.9 ± 1.9 and 3.8 ± 1.7 for ^{12}CO 3–2 in IC 348, NGC 1333 and L 1455, respectively; while m is 3.9 ± 2.0 , 3.5 ± 2.5 and 4.1 ± 1.8 for ^{13}CO 2–1 in the same three regions. In the blue wings (Fig. 3.11b), I obtain m values of 3.2 ± 1.6 , 3.4 ± 1.4 and 3.6 ± 1.5 for ^{12}CO 3–2; while m is 4.3 ± 1.9 , 4.3 ± 1.7 and 4.1 ± 1.5 for ^{13}CO 2–1 in the three regions. These values have large error bars, so that they are not directly suited to discriminate between different turbulence models. At least, I find that all values are consistent with Kolmogorov turbulence that gives $m \sim 3.7$ (Kolmogorov, 1941).

3.5 Summary

1. I present KOSMA maps of the ^{13}CO 2–1 and ^{12}CO 3–2 emission of the Perseus molecular cloud covering 7.1 deg^2 . These data are combined with FCRAO maps of integrated ^{12}CO and ^{13}CO 1–0 intensities and with a 2MASS map of optical extinctions.
2. To characterize the cloud density structure, I applied the Δ -variance analysis to integrated intensity maps. The Δ -variance spectra of the overall region follow a power law with an index of $\beta = 2.9 - 3.0$ for scales between 0.2 and 3 pc. This agrees with results obtained by Padoan et al. (2003a) studying structure functions of a ^{13}CO 1–0 map of Perseus.
3. I also applied the Δ -variance method to seven sub-regions of Perseus. The resulting power spectral indices vary significantly between the individual regions. The active star-forming region NGC 1333 shows high spectral indices ($\beta = 3.5 - 3.8$) while the dark cloud L 1455 shows low indices of 2.9 in both transitions.
4. Additional information is obtained from the Δ -variance spectra of individual velocity channel maps. They are very sensitive to optical depth effects, indicating self-absorption in the densest regions. The asymmetry of the channel map indices relative to the line centrum is a hint towards a peculiar velocity structure of the Perseus cloud complex.
5. When analyzing the spectral indices as a function of the velocity channel width I find almost constant indices when averaging over the total line profile. A continuous increase of the index with varying velocity channel width

is, however, observed in the blue wings. This behavior can be explained by a shock running through the region creating a filamentary structure preferentially at low velocities.

I find that the comparison of the structural properties for entire surveys and sub-sets, as well as the velocity channel analysis (VCA), provide additional, significant characteristics of the ISM in observed CO spectral line maps. These quantities are useful for a comparison of the structure observed in different clouds, possibly providing a diagnostic tool to characterize the star-formation activity and providing additional constraints for numerical simulations of the ISM structure.

In the next chapter (Chapter 4), I will use a different approach to quantify the structure with decomposing the observed emission into discrete entities ("clumps"). For this purpose, *Gaussclumps* is used in that analysis.

Chapter 4

The *Gaussclumps* analysis in the Perseus cloud

Visual inspection of position-velocity cuts and of channel maps of molecular clouds, indicate a large number of structures; all these maps exhibit a complex, inhomogeneous, nested, filamentary, or clumpy structure on all scales down to the resolution limits. These maps appear self-similar: the structure looks the same independent of the scales. The derivation of clump mass spectra leads to a better quantification of this description. Another motivation to analyze the distribution of clump masses is, that it possibly determines the stellar initial mass function, which in turn determines all stellar evolution, and its links with star formation efficiency (Zinnecker et al., 1993).

In this chapter, I use *Gaussclumps* (Stutzki & Güsten, 1990) to identify clumps in the Perseus molecular cloud and to investigate its properties. The aim of the analysis is to identify clumps in clouds and to derive their basic properties, such as sizes, line widths and masses. Here I study mainly the ^{13}CO 2–1 data from the KOSMA 3m telescope and the ^{13}CO 1–0 data from the FCRAO 14m telescope.

This chapter is organized as the following: Section 1 presents the results and discussions on clump mass spectra, the relations of clump size with line width and mass and the equilibrium state of the clumps; a summary is given in Section 2.

4.1 Results and discussions

Using the KOSMA ^{13}CO 2–1 data, there are 341 clumps found, the mass range of which is between $0.54 M_{\odot}$ and $87.98 M_{\odot}$. And I find 737 clumps using the FCRAO ^{13}CO 1–0 data and the clump mass ranges from $0.28 M_{\odot}$ and $140.90 M_{\odot}$.

Fig. 4.1 presents the clump center velocity and peak temperature for the clumps

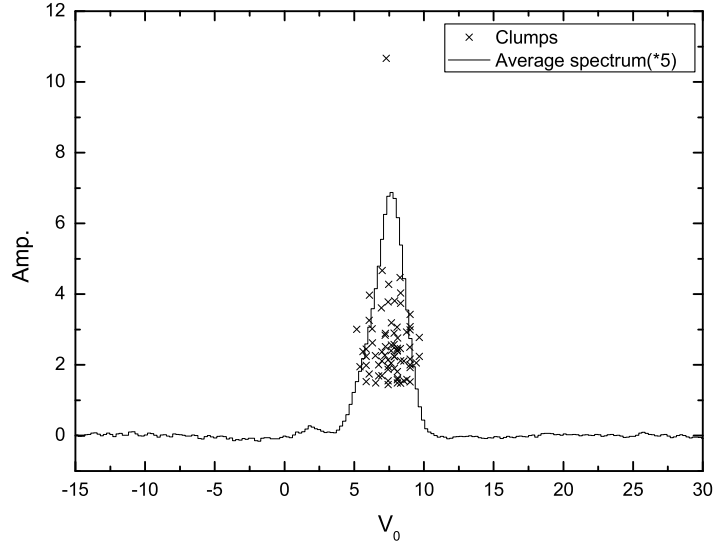


Figure 4.1: Velocity (v_0) of the clumps found in NGC 1333 versus peak intensity (amp.). The average spectrum of ^{13}CO 2-1 in NGC1333 is also presented.

found in NGC 1333. The averaged spectrum of ^{13}CO 2-1 emission is also presented in the figure. The peak temperatures of all clumps are significantly above the general noise level. Furthermore, the center velocities of those clumps lie within the velocity range of emission. This is one additional proof, that almost all clumps are decomposed from the emission.

4.1.1 Clump mass

Under the assumption of local thermodynamic equilibrium and optically thin emission of ^{13}CO 2-1, I calculate the ^{13}CO clump column density using ^{13}CO 2-1 clump brightness temperatures T_{mb} in K and the FWHM line widths Δv in km s^{-1} . To derive the clump mass, I assume that the excitation temperature is fixed to be 10 K. In the active star forming regions like NGC 1333, the excitation temperature must be higher. However, ^{13}CO column densities are only weakly sensitive to the exact choice of the excitation temperature. If excitation temperature is changed to 20 K or to 30 K, the derived column densities increases only by 40% and 92%, respectively. So the T_{ex} assumption of 10 K will be good estimation. Then taken the canonical abundance factors of $[^{12}\text{CO}/^{13}\text{CO}] = 65$ (Langer et al.,

1990) and $[H_2/^{12}CO] = 8 \times 10^5$ (Frerking et al. , 1982), ^{13}CO column densities are converted into H_2 column densities.

The total mass of a clumps can be computed from the H_2 column density, the solid angle of the clump and the distance of the cloud. Hence, the clump mass in the unit of solar masses is written as (see Appendix A for details):

$$M_{\text{clump}} = 1.30 \times 10^6 \cdot T_0(\text{K}) \cdot \Delta x \cdot \Delta y \cdot \Delta v (\text{kms}^{-1}) M_{\odot}, \text{ for } ^{13}\text{CO}2-1, \quad (4.1)$$

$$M_{\text{clump}} = 2.06 \times 10^6 \cdot T_0(\text{K}) \cdot \Delta x \cdot \Delta y \cdot \Delta v (\text{kms}^{-1}) M_{\odot}, \text{ for } ^{13}\text{CO}1-0, \quad (4.2)$$

where Δx and Δy are in radian.

The minimum possible mass is given by the spatial and velocity resolution, and the rms noise of the data, which is the smallest clump mass the *Gaussclumps* algorithm can possibly find. For the Perseus cloud, the low mass limit ($M_{\text{min}}^{\text{limit}}$) for ^{13}CO 2–1 is given by

$$M_{\text{min}}^{\text{limit}} = 1.30 \times 10^6 T_{\text{rms}}(\text{K}) \cdot \Delta v_{\text{res}} (\text{kms}^{-1}) \cdot d_{\text{beam}}^2 = 0.14 M_{\odot}, \text{ for } ^{13}\text{CO}2-1, \quad (4.3)$$

$$M_{\text{min}}^{\text{limit}} = 2.06 \times 10^6 T_{\text{rms}}(\text{K}) \cdot \Delta v_{\text{res}} (\text{kms}^{-1}) \cdot d_{\text{beam}}^2 = 0.019 M_{\odot}, \text{ for } ^{13}\text{CO}1-0, \quad (4.4)$$

where beam size is in radian.

The smallest clump masses found in the Perseus cloud is always higher than this minimum possible mass by at least a factor of a few tens.

4.1.2 Clump mass spectra

Here, I will focus on the results of clump mass spectra. Similar to the Δ -variance analysis in Chapter 3, I will first present the clump mass spectra of the whole observed Perseus cloud, then I will study the clump mass spectra of the seven individual sub-regions.

Fig. 4.2 shows an example how different bin size will affect fitted power law indices of clump mass spectra. The figure presents the clump mass spectra of ^{13}CO 2–1 in the whole observed Perseus cloud with different bin sizes. A least-squares fit, weighted by the error bars represent assuming a Poisson distribution $\sqrt{\Delta N}$, is used to obtain power law indices. The fitted clump mass range is from $10^{0.40} M_{\odot}$ to $10^{1.95} M_{\odot}$. When the bin size changes from $10^{0.2} M_{\odot}$, $10^{0.3} M_{\odot}$, $10^{0.4} M_{\odot}$, to $10^{0.5} M_{\odot}$, the power index of the clump mass spectra varies from 1.87 ± 0.07 , 1.90 ± 0.07 , 1.70 ± 0.06 , to 1.86 ± 0.06 correspondingly. The average power index α is $1.83_{0.19}^{0.14}$. Such effect has also been studied by Wong et al. (2008) using the ^{13}CO 1–0 data in RCW 106. They found that varying the bin size between $10^{0.1} M_{\odot}$ and $10^{0.25} M_{\odot}$ yields power laws between 1.6 and 1.75.

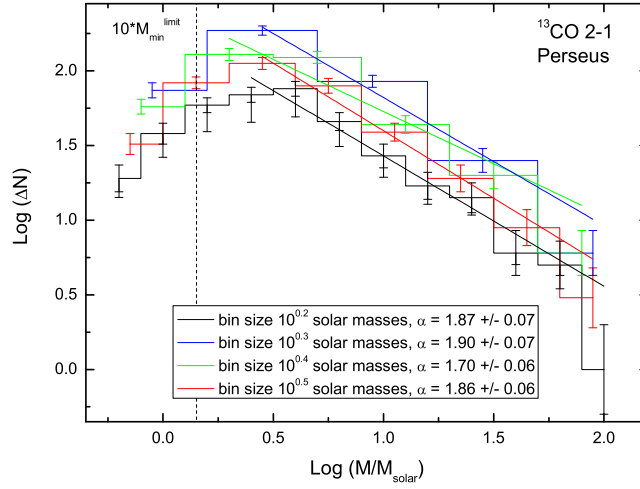


Figure 4.2: An example of the effect of different clump mass binning sizes. The bin size changes from $10^{0.2} M_{\odot}$, $10^{0.3} M_{\odot}$, $10^{0.4} M_{\odot}$, to $10^{0.5} M_{\odot}$. Error bars represent the standard deviation of a Poisson distribution $\sqrt{\Delta N}$. The dashed line denotes the lower clump mass limit ($10 * M_{\min}^{\text{limit}}$).

The derivation of the power indices is small, which indicates that bin size has no big effect on the results. In the following, I will choose a bin size of $10^{0.2} M_{\odot}$ for all the analysis.

4.1.2.1 The whole observed Perseus cloud

I firstly derive the power indice of clump mass spectra of the whole observed Perseus cloud for the KOSMA ^{13}CO 2–1 data and the FCRAO ^{13}CO 1–0 data (see Fig. 4.3). Due to the much smaller beam of the FCRAO telescope ($\sim 46''$), there are much more clumps identified, especially small clumps, using the ^{13}CO 1–0 data. A least-squares fit is used to obtain the power law index. The fitted clump mass ranges are from $10^{0.4} M_{\odot}$ to $10^{1.9} M_{\odot}$ for ^{13}CO 2–1 data and from $10^{0.7} M_{\odot}$ to $10^{1.9} M_{\odot}$ for ^{13}CO 1–0 data. The minimum clump mass M_{\min}^{cl} , found from the FCRAO ^{13}CO 1–0 data, is much larger than 10 times of the lower mass limit M_{\min}^{limit} ($0.019 M_{\odot}$ for ^{13}CO 1–0, $1.42 M_{\odot}$ for ^{13}CO 2–1).

For both ^{13}CO 1–0 and ^{13}CO 2–1, the fitted power law indices are close to 1.9, which is consistent with the results from other clouds (Kramer et al., 1998b; Simon et al., 2001; Mookerjee et al., 2004; Wong et al., 2008).

Table 4.1: Comparison of the masses of clump identified in the Perseus cloud with studies of other molecular clouds. The cloud name, studied tracers, distance, and the HPBW are listed in Column (1), (2), (3) and (4); Column (5) presents the number of selected clumps; The mass range used for the least-squares fit is in Column (6). Column (7) and (8) present the total mass of all clumps selected and the minimum mass identified with the criteria of Equation 1.4; The fitted power law index α is given in Column (9) (note that I adopt the power law index for a bin size of $10^{0.2} M_{\odot}$ for comparison); Column (10) is the reference: ^a This work; ^b Kramer et al. (1998b); ^c Simon et al. (2001).

Cloud	tracer	Distance [pc]	HPBW [pc]	N_{cl}	Mass range M_{\odot}	M_{tot}^{cl} M_{\odot}	M_{min}^{cl} M_{\odot}	α	Reference
Perseus	^{13}CO 2–1	350	0.221	341	2.51 - 79.43	2291.89	0.54	1.90 ± 0.08	a
Perseus	^{13}CO 1–0	350	0.078	737	5.01 - 79.43	8431.86	0.28	1.89 ± 0.07	a
S 140	C^{18}O 2–1	910	0.057	130	0.6 - 160	840	0.4	1.77 ± 0.30	b
NGC 7538	C^{18}O 1–0	2200	0.533	110	50 - 3900	27000	34	1.79 ± 0.12	b
Orion B-S	^{13}CO 2–1	400	0.242	216	3 - 320	2970	0.52	1.72 ± 0.09	b
GRSMC 45.60 + 0.30	^{13}CO 1–0	1800	0.401	235	15.85 - 1000	12000	3.55	1.78 ± 0.30	c
W 49	^{13}CO 1–0	11400	2.542	85	1000 - 39811	320000	125.89	1.52 ± 0.20	c

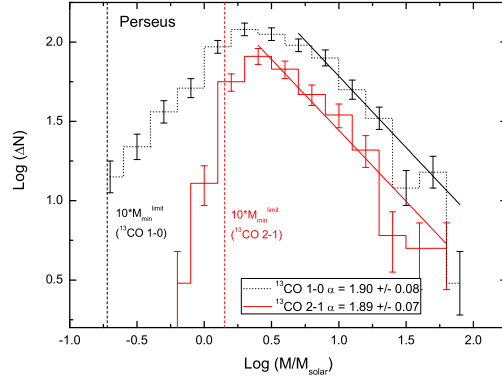


Figure 4.3: Clump mass spectra of the Perseus molecular cloud from both the FCRAO ^{13}CO 1–0 data and the KOSMA ^{13}CO 2–1 data. Both spectra are fitted by a power law function $dN = dM/M^{-\alpha}$. The straight line represents the best linear fit over the range of masses spanned by the line. The resulting indices α for both datasets are very similar, ~ 1.9 . The two vertical dashed lines show the 10 times of the lower mass limits for both tracers.

4.1.2.2 The seven sub-regions in the Perseus cloud

To study the behavior of the power indices of clump mass spectra for different regions (quiescent or star forming), I divide the Perseus molecular cloud into seven sub-regions as the same as the Δ -variance analysis in Chapter 3. Then using the KOSMA ^{13}CO 2–1 data, I derive the power law indices of the clump mass spectra. The results of the seven sub-regions are presented in Fig. 4.4 and Table 4.2. The clump identification works on the way that the maximum clump masses found reflect the peak temperatures, maximum line widths, and largest spatial clump sizes found in an observed region. Molecular clouds with ongoing star formation like NGC 1333, exhibit massive clumps of up to $\sim 100 M_{\odot}$, whereas quiescent, cold clouds like L 1455 and L 1448, only show clumps of less than $30 M_{\odot}$.

I also perform a least-squares fit to the data. The lower mass limit of the fit is fixed to all the seven sub-regions to $10^{0.5} M_{\odot}$ and the upper mass limit is the maximum clump mass of each sub-region. The upper limit of each sub-region is different. The biggest up limit is $\sim 101.02 M_{\odot}$ in NGC 1333, while the smallest one is $\sim 19.40 M_{\odot}$ in L 1455. The power law indices of the seven regions show slightly variation, changing from 1.65 in IC 348 and 1.85 in B 1 EAST. The active star forming region, NGC 1333, does not have the largest power law index. while the quiescent clouds like L 1455, B1 and B1 EAST have the largest power law index. It seems that the power law index of clump mass spectra is not directly related to star forming activities. The average power law index of those seven

Table 4.2: The results of the seven sub-regions. The cloud name is listed in Column (1); Column (2) presents the number of selected clumps; The mass range used for the least-squares fit is in Column (3). Column (4) and (5) present the total mass of all clumps selected and the minimum mass identified with the criteria of Equation 1.4; The fitted power law index α is given in Column (6).

Cloud	N_{cl}	Mass range Log(M_{\odot})	$M_{\text{tot}}^{\text{cl}}$ M_{\odot}	$M_{\text{min}}^{\text{cl}}$ M_{\odot}	α
L 1448	28	0.5 - 1.5	156.92	0.62	1.72 ± 0.24
L 1455	39	0.5 - 1.1	179.45	0.65	1.81 ± 0.27
NGC 1333	76	0.5 - 2.1	547.77	0.56	1.78 ± 0.17
B 1	58	0.5 - 1.7	333.12	0.54	1.83 ± 0.19
B 1 East	43	0.5 - 1.5	270.82	0.59	1.85 ± 0.18
B 3	70	0.5 - 1.5	377.71	0.55	1.76 ± 0.20
IC 348	65	0.5 - 1.9	611.23	0.66	1.65 ± 0.13

regions is 1.80, which is a typical value found in the previous studies of clump mass spectra. It may show a trend that clump mass spectra have a common power law index, independent of star formation activity, which have also been pointed out by Kramer et al. (1998b); Simon et al. (2001).

The power law index of clump mass spectra found using the molecular line data (mainly CO) is also often smaller than that using the (sub)millimeter continuum (Mookerjee et al., 2004; Kirk et al., 2006). The different power law indices between CO and (sub)millimeter continuum may be due to different methods of observations, in the definition of structure, the effects of chemistry such as freeze-out, or real differences in the structures at the large and small scales (Kirk et al., 2006).

4.1.3 Relations of clump size with line width and mass

In this subsection, I will study the relations of clump size with line width, and with mass in the Perseus cloud and two typical sub-regions: NGC 1333 and L 1455. NGC 1333 is an active star forming region and L 1455 is a quiescent dark cloud. Hence, those two sub-regions are typical examples in the Perseus cloud.

Fig. 4.5 and Fig. 4.6 present the relations between line width and mass as a function of size of all clumps in the three regions mentioned before. The clump radius is defined as the geometric mean of the major and minor half-axes identified from *Gaussclumps*.

The contribution from the thermal line width to the observed line width may be considerable and could flatten the power index of a size-line width relation (Myers & Goodman, 1988). For ^{13}CO , the thermal line width can be given as

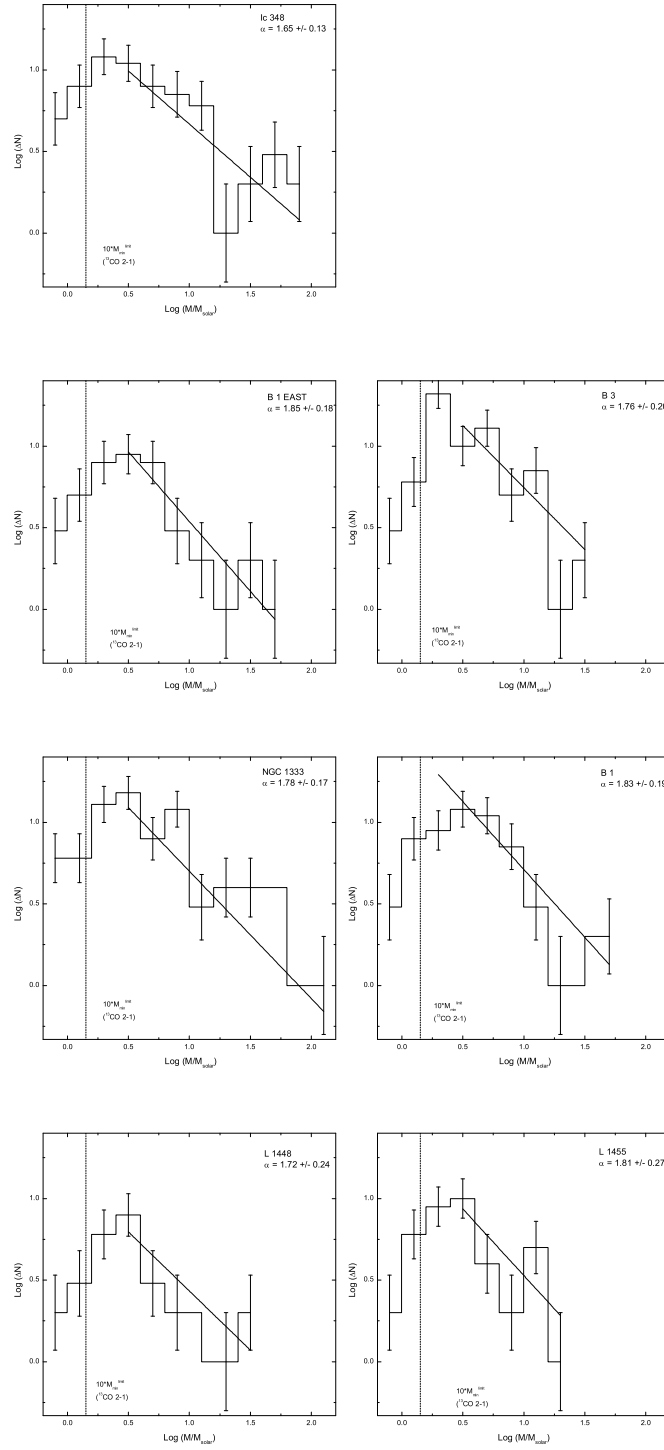


Figure 4.4: Clump mass spectra of the seven sub-sets in the Perseus molecular cloud. All spectra are fitted by a power law function $dN = dM/M^{-\alpha}$. The straight line represents the best linear fit over the range of masses spanned by the line. The resulting indices α lie in the range 1.65 to 1.85. The vertical dashed line shows the 10 times of the lower mass limits.

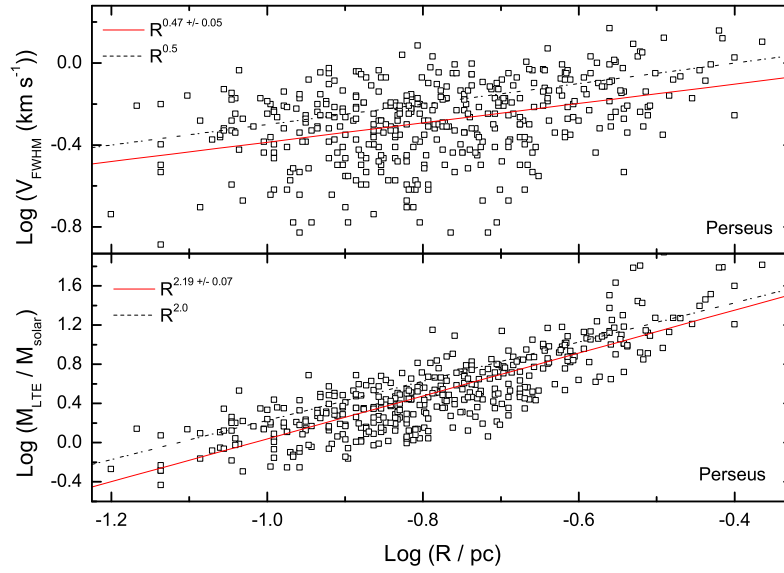


Figure 4.5: Size-line width (top panel) and size-mass (bottom panel) relations for the Perseus cloud using ^{13}CO 2–1 data. Least-squares fits to $\Delta v \propto R^{\alpha_{\text{lw}}}$, and $M_{\text{LTE}} \propto R^{\alpha_{\text{m}}}$ are presented by the solid lines. The dashed lines show fit with fixed power law indices of $\alpha_{\text{lw}} = 0.5$ and $\alpha_{\text{m}} = 2$, which correspond the conventional Larson relations (Larson, 1981).

$\Delta v_{\text{th}} = 2(\ln 2)^{\frac{1}{2}} \sqrt{\frac{kT_{\text{kin}}}{u}} = 0.13 \sqrt{\frac{T_{\text{kin}}}{10}} \text{ km s}^{-1}$, where k is the Boltzmann constant, T_{kin} is the kinetic temperature in K, and u is the mean molecular weight. For a kinetic temperature of 10 K, each clump identified has highly supersonic line widths.

Least-squares fits to $\Delta v \propto R^{\alpha_{\text{lw}}}$, and $M_{\text{LTE}} \propto R^{\alpha_{\text{m}}}$ are presented in Fig. 4.5 and Fig. 4.6. For the whole Perseus cloud, we obtain α_{lw} of 0.47 ± 0.05 and α_{m} of 2.19 ± 0.17 . For NGC 1333 and L 1455, the fitted α_{lw} is 0.51 ± 0.17 and 0.78 ± 0.10 , respectively; the fitted α_{m} is 1.96 ± 0.18 and 2.45 ± 0.13 for NGC 1333 and L 1455, respectively. Previous studies yield power law indices that cover wide ranges: α_{lw} between 0.15 and 0.7, and α_{m} between 1.7 and 2.5 (Larson, 1981; Leung et al., 1983; Myers, 1983; Sanders et al., 1985; Dame et al., 1986; Solomon et al., 1987; Heithausen, 1996; Kramer et al., 1996; Heyer & Schloerb, 1997; Williams et al., 2000; Simon et al., 2001). The fitted indices from this work are consistent with those studies.

The assumption of gravitational virial equilibrium $GM/R \propto \Delta v^2$ implies scaling relation of the form $\alpha_{\text{lw}} = (\alpha_{\text{m}} - 1)/2$ (Simon et al., 2001). Values of the different power-law indices were empirically determined from giant molecular

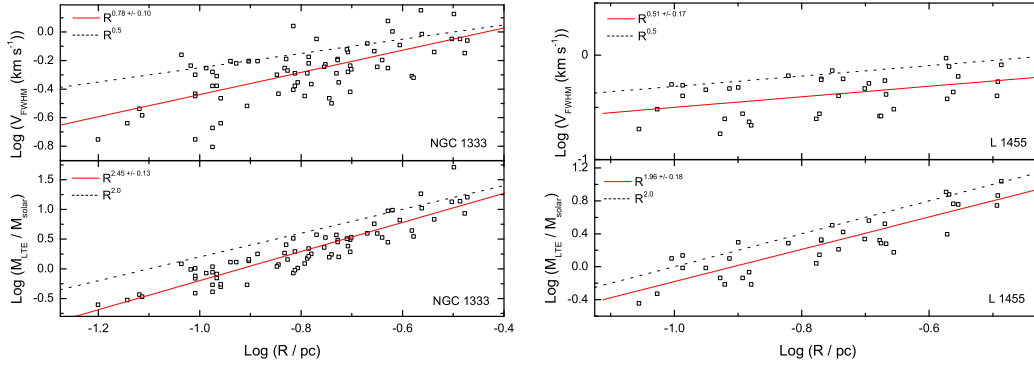


Figure 4.6: Same as Fig. 4.5, but for two examples of seven sub-regions: NGC 1333 and L 1455.

cloud complexes and high-density clumps to be $\alpha_{lw} = 0.5$ and $\alpha_m = 2$, which extend over several orders of magnitude in scale and with a small scatter (see the reviews by Myers, 1987; Scalo, 1987). Hence, those empirical values are in agreement with the assumption of gravitational virial equilibrium. In this work, the values of α_{lw} and α_m in the whole Perseus and NGC 1333 are very close to 0.5 and 2, respectively, especially in NGC 1333. The correlation between size and density and between size and line width is quite good. The two power law indices in those three regions (Perseus, NGC 1333 and L 1455) nearly fulfil the relation of $\alpha_{lw} = (\alpha_m - 1)/2$, which indicates a gravitational virial equilibrium in those three regions.

4.1.4 Equilibrium state of the clumps

In this section, I use the virial parameter $\alpha_G = M_{vir}/M_{LTE}$ (Bertoldi & McKee, 1992) to characterize the equilibrium state of a cloud or clump. The virial parameter is a measure of the ratio of kinetic to gravitational energy density.

As fitted to the observed data cubes by *Gaussclumps* have Gaussian density profiles (Stutzki & Güsten, 1990; Stutzki et al., 1998), I use the analytical expression for a Gaussian density distribution in the virial theorem to calculate virial masses of the decomposed clumps (Simon et al., 2001). In the absence of external pressure and magnetic fields, the virial theorem $2T_{kin} + W = 0$ for a Gaussian clump with a radial density distribution takes the form (Stutzki & Güsten, 1990)

$$3M\sigma^2 - \sqrt{\frac{\ln 2}{2\pi}} \frac{GM^2}{R} = 0, \quad (4.5)$$

where $G = 1/232$ is the gravitational constant in unit of $\text{km}^2 \text{s}^{-2} \text{pc } M_{\odot}^{-1}$; σ is the velocity dispersion in km s^{-1} ; and R denotes the radius of the clump in pc. So the

viral mass of a clump with Gaussian density distribution can be given by (Simon et al., 2001)

$$\frac{M_{\text{vir}}}{M_{\odot}} = 378 R \Delta v^2, \quad (4.6)$$

where Δv is the FWHM line width ($\Delta v = \sigma(8 \ln 2)$).

The ratio of virial to LTE clump mass as a function of LTE clump mass in the Perseus cloud and in the two sub-regions (NGC 1333 and L 1455) is presented in Fig. 4.7 and Fig. 4.8, respectively. In the two sub-regions, all clumps identified are found above $M_{\text{vir}}/M_{\text{LTE}} = 1$; in the Perseus cloud, only one clump is below $M_{\text{vir}}/M_{\text{LTE}} = 1$ and the rest are above that. The ratios of the virial to LTE mass for the Perseus cloud are between 0.77 (only 1 clump) and 13.61. And the same ratios are between 2.43 and 14.38 for NGC 1333, and from 1.94 to 11.98 for L 1455. This means that those clumps are not gravitationally bound. This results show the same trend as those found in the previous studies that clumps typically have ratios of virial to LTE mass well above the limit of virialization, $M_{\text{vir}}/M_{\text{LTE}} \simeq 1$ (Bertoldi & McKee, 1992; Williams et al., 1995; Heyer et al., 2001; Simon et al., 2001).

There is a tight correlation of the virial parameter with clump mass according to $\alpha_G = (M_0/M_{\text{LTE}})^{\frac{2}{3}}$ found by Bertoldi & McKee (1992); Williams et al. (1995); Heyer et al. (2001). Such correlation is theoretically expected for gravitationally unbound, pressure-confined clumps (Bertoldi & McKee, 1992). While in this work, the distributions of the virial parameter with clump mass for the clumps identified in both the whole Perseus cloud and in NGC 1333 and L 1455 show no trend of following this correlation as the also found by Kramer et al. (1996); Simon et al. (2001). However, for large values of α_G and masses above the completeness limit, the virial parameters for the clumps seem to follow the correlation. I also plot the power law index of $-\frac{2}{3}$ in Fig. 4.7 and Fig. 4.8 (solid lines in the figures).

The external pressures (P_{ex}) can be evaluated by adding the surface term $4\pi R^3 P_{\text{ex}}$ to the equation of virial equilibrium. So the binding pressure of a clump is written as

$$\frac{P_{\text{ex}}}{k} = 0.56 \frac{M}{R^2} \left(378 \frac{\Delta v^2}{R} - \frac{M}{R^2} \right) K \text{cm}^{-3}, \quad (4.7)$$

and it can also be given by

$$\frac{\sigma^2}{R} \propto \frac{P_{\text{ex}}}{k} \frac{1}{N(H_2)} + N(H_2). \quad (4.8)$$

The balance between the external pressure and the turbulent gas pressure is described by that equation. Clumps with $P_{\text{ex}} \simeq 0 \text{ K cm}^{-3}$ are gravitationally bound. Histograms of required external pressure were developed from the data in Fig. 4.9 for the Perseus cloud and Fig. 4.10 for NGC 1333 and L 1455. The

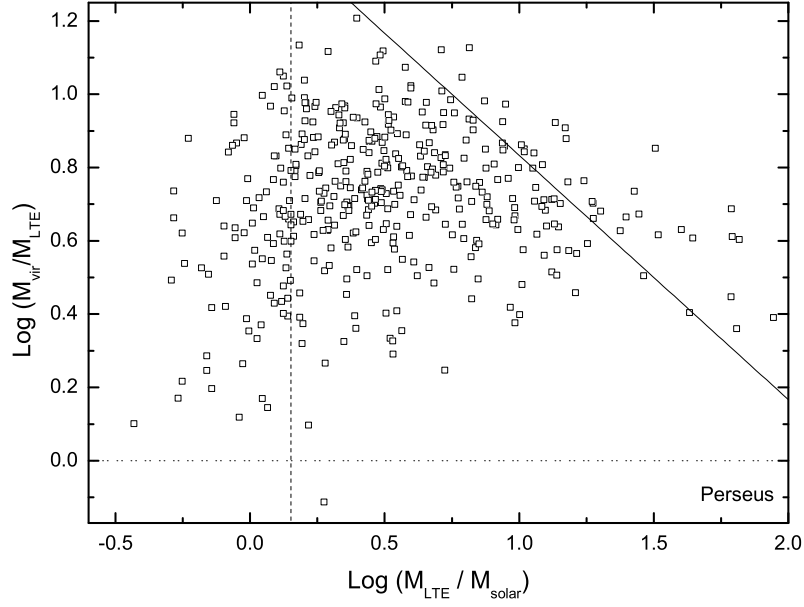


Figure 4.7: Ratio of virial to LTE mass as a function of LTE mass for the clumps in the Perseus cloud. The dotted line corresponds to $M_{\text{vir}} = M_{\text{LTE}}$; The dashed line shows the 10 times of the lower mass limits for M_{LTE} . The solid line presents a power law index of $-\frac{2}{3}$.

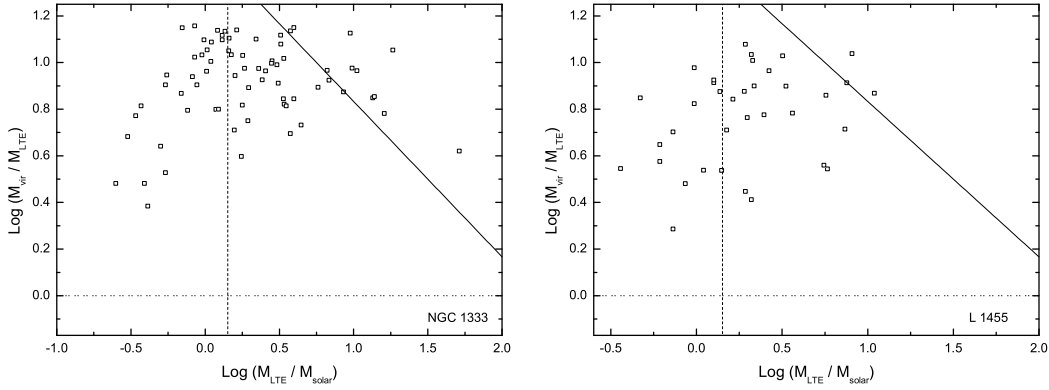


Figure 4.8: Same as Fig. 4.7, but for two examples of seven sub-regions: NGC 1333 and L 1455.

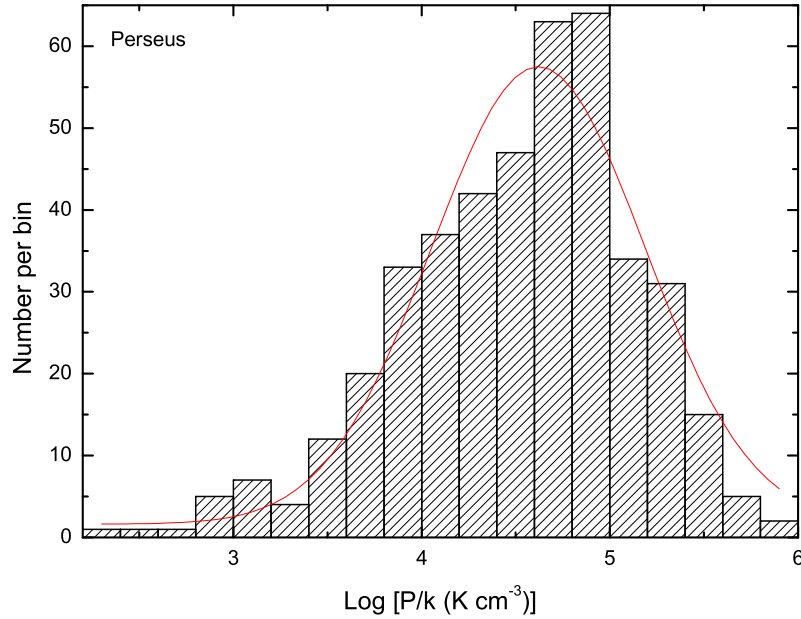


Figure 4.9: Histograms of the external pressures needed to bind the clumps for the whole Perseus cloud. The solid line donates a Gaussian fit to the results.

external pressures needed range mainly from 10^3 K cm^{-3} to 10^6 K cm^{-3} for the whole Perseus, while the ranges slightly vary: 10^3 K cm^{-3} to 10^5 K cm^{-3} for NGC 1333 and $10^{2.5} \text{ K cm}^{-3}$ to $10^{4.2} \text{ K cm}^{-3}$ for L 1455. The Gaussian fit to the histograms lie at $10^{4.6} \text{ K cm}^{-3}$ with a width of $10^{1.1} \text{ K cm}^{-3}$ for the Perseus cloud, $10^{3.7} \text{ K cm}^{-3}$ with a width of $10^{0.8} \text{ K cm}^{-3}$ for NGC 1333, and $10^{3.7} \text{ K cm}^{-3}$ with a width of $10^{0.3} \text{ K cm}^{-3}$ for L 1455.

The simulations together with the observed highly supersonic line widths suggest that if turbulence supports molecular clouds against star formation, it must be constantly driven or large molecular clouds would be transient, efficiently star-forming objects (Simon et al., 2001). Since dynamical timescale of clumps is much smaller than that of the cloud and the random, turbulent flow that creates local density enhancements can also disperse clumps. Clumps that are not self-gravitating will be rapidly dispersed if they are not confined by external pressure. The observed large number of clumps with high virial parameters implies that they are either unbound, dispersed, and reformed anew at a high rate or else bound by external pressure. Bertoldi & McKee (1992) suggest the latter to be the case since the magnitude of external pressures they estimate for the clouds in their study is similar to the required binding pressures for the clumps.

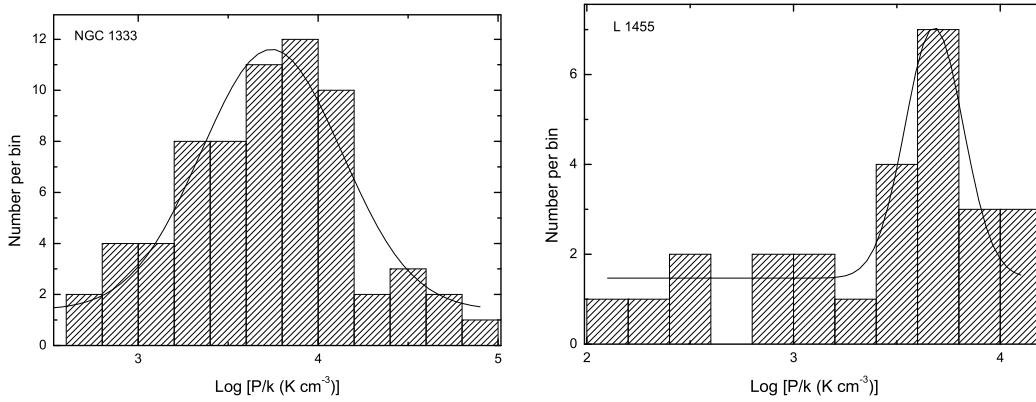


Figure 4.10: Same as Fig. 4.9, but for two examples of seven sub-regions: NGC 1333 and L 1455.

4.2 Summary

A three-dimensional Gaussian decomposition algorithm (*Gaussclumps*) has been used to identify clumps inside each cloud and to derive the clump properties as traced in ^{13}CO 1–0 and 2–1 in the Perseus cloud. A power law index of ~ 1.9 has been found for the whole observed Perseus cloud. When studying the seven sub-regions in the Perseus cloud, a common power law index of ~ 1.80 has been found, which may show a trend that clump mass spectra have a common power law index, independent of star formation activity, which have been found by Kramer et al. (1998b); Simon et al. (2001).

Relations of clump size with line width and mass have been studied. The obtained α_{lw} and α_{m} follow the relation of $\alpha_{\text{lw}} = (\alpha_{\text{m}} - 1)/2$ for both the Perseus cloud and the two examples of the seven sub-regions (NGC 1333 and L 1455), which implies that those clouds are in gravitational virial equilibrium. The values of α_{lw} and α_{m} confirm the standard Larson relations, especially of the Perseus cloud and NGC 1333.

I have used the virial parameter $\alpha_{\text{G}} = M_{\text{vir}}/M_{\text{LTE}}$ (Bertoldi & McKee, 1992) to characterize the equilibrium state of a cloud or clump. All clumps identified in NGC 1333 and L 1455 are found above $M_{\text{vir}}/M_{\text{LTE}} = 1$; And in the Perseus cloud, All except one clump is above $M_{\text{vir}}/M_{\text{LTE}} = 1$. The ratios of the virial to LTE mass for the Perseus cloud are between 0.77 (only 1 clump) and 13.61. And the same ratios are between 2.43 and 14.38 for NGC 1333, and from 1.94 to 11.98 for L 1455. It confirms the previous studies that clumps typically have ratios of virial to LTE mass well above the limit of virialization, $M_{\text{vir}}/M_{\text{LTE}} \simeq 1$.

As found by Kramer et al. (1996); Simon et al. (2001), this work does not

find a tight correlation of the virial parameter with clump mass according to $\alpha_G = (M_0/M_{\text{LTE}})^{\frac{2}{3}}$ found by Bertoldi & McKee (1992); Williams et al. (1995); Heyer et al. (2001). However, for large values of α_G and masses above the completeness limit, the virial parameters for the clumps seem to follow the correlation.

The external pressures needed to bind the clumps range mainly from 10^3 K cm^{-3} to 10^6 K cm^{-3} for the whole Perseus. In NGC 1333, the range varies from 10^3 K cm^{-3} to 10^5 K cm^{-3} and it is between $10^{2.5} \text{ K cm}^{-3}$ to $10^{4.2} \text{ K cm}^{-3}$ in L 1455.

In Chapter 3 and Chapter 4, I have presented the structure analysis using both Δ -variance and *Gaussclumps*. In the next two chapters, I will zoom into a particular part of the Perseus cloud (IC 348) and the Cepheus B cloud and study the structure and properties of those two clouds using an alternative method, the PDR analysis.

Chapter 5

Study of the photon dominated region in the IC 348 cloud

In this chapter, I will zoom into a particular sub-region in the Perseus cloud, IC 348 to study the photon dominated region in that sub-region. Here, I present large-scale ($20' \times 20'$) fully-sampled maps of the [C I] $^3P_1 - ^3P_0$ (hereafter [C I]) and ^{12}CO 4–3 emission from the IC 348 molecular cloud. The map coordinates in IC 348 refer to the (0,0) center position at $\alpha = 03^h44^m10^s$, $\delta = 32^\circ06'$ (J2000). At a common resolution of $70''$, I combine the data with the ^{12}CO 1–0, ^{13}CO 1–0 data from the Five College Radio Astronomy Observatory (FCRAO), and FIR continuum data from HIREs/IRAS. The goal of the analysis presented is to understand to what degree the observed line emission can be understood in the framework of a photon dominated region. The upper level energy of [C I] 1–0 is 24 K and the critical density is 10^3 cm^{-3} for collisions with H_2 (H) (Beuther et al., 2000). Hence this level is easily excited under standard molecular cloud conditions. Although chemical models predicted that neutral carbon occurs only in a thin layer between ionized carbon and molecular CO, many [C I] observations have indicated extended emission well correlated with low- J CO (see a review by Preibish et al., 1996; Schneider et al., 2003; Mookerjee et al., 2006).

Section 5.1 describes the KOSMA observations and the complementary datasets used for analysis. Section 5.2 discusses the general observational results. A Local Thermodynamic Equilibrium (LTE) analysis of the observed line intensities is presented in Section 5.3. Comparison of the observed line intensities and ratios with clumpy PDR models is in Section 5.4. Section 5.5 summarizes the results.

5.1 Datasets

5.1.1 [C I] and ^{12}CO 4–3 observations with KOSMA

I have used the Kölner Observatorium für Sub-Millimeter Astronomie (KOSMA) 3-m sub-millimeter telescope on Gornegrat, Switzerland (Winnewisser et al., 1986; Kramer et al., 1998a) to observe the emission of the fine structure line of neutral carbon at 492 GHz and ^{12}CO 4–3 at 461 GHz. I have used the Sub-Millimeter Array Receiver for Two frequencies (SMART) on KOSMA for these observations (Graf et al., 2002). SMART is an eight-pixel dual-frequency SIS-heterodyne receiver capable of observing in the 650 and 350 μm atmospheric windows (Graf et al., 2002). The IF signals were analyzed with two 4×1 GHz array-acousto-optical spectrometers with a spectral resolution of 1.5 MHz (Horn et al., 1999). The typical double side band receiver noise temperature at 492 GHz is about 150 K. The observations were performed in position-switched On-The-Fly (OTF) between December 2004 and February 2005. Owing to technical difficulties the higher frequency channel of SMART could not be used at the time of these observations.

I observed a fully sampled map of the IC 348 molecular cloud centered at $\alpha = 03^{\text{h}}44^{\text{m}}10^{\text{s}}$, $\delta = 32^{\circ}06'(\text{J2000})$, extending over $20' \times 20'$. For the observations, I used the position-switched on-the-fly (OTF) mode (Beuther et al., 2000) with a sampling of $29''$. The emission-free off position was selected from the ^{13}CO 1–0 FCRAO map, which is $(-8', 10')$ relative to the map center. I estimate the pointing accuracy to be better than $10''$. The half power beam width (HPBW) and the main beam efficiency (B_{eff}) were derived from continuum scans of the Sun and the Jupiter. The HPBW at both frequencies is $60''$ and the main beam efficiency is 50%. The forward efficiency F_{eff} of the telescope is $\sim 90\%$. Atmospheric calibration was done by measuring the atmospheric emission at the OFF-position and using a standard atmospheric model to fit the opacity taking into account the sideband imbalance (Cernicharo, 1985; Hiyama, 1998).

All data presented in this paper are in units of main beam temperature T_{mb} , calculated from the observed calibrated antenna temperature T_{A}^* using the derived beam and forward efficiencies, $T_{\text{mb}} = T_{\text{A}}^* (F_{\text{eff}}/B_{\text{eff}})$. Based on observations of reference sources such as W 3 and DR 21 I estimate the accuracy of the absolute intensity calibration to be better than 15%. The data reduction was carried out using the GILDAS¹ software package.

¹<http://www.iram.fr/IRAMFR/GILDAS/>

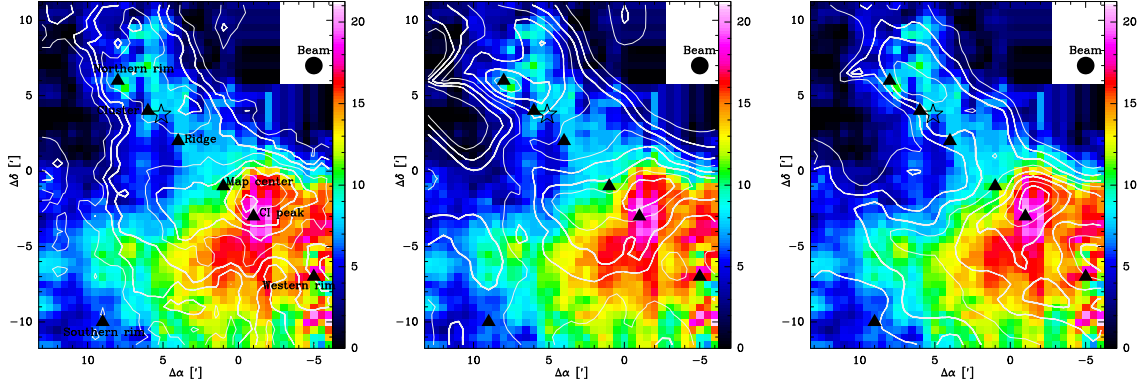


Figure 5.1: Velocity integrated intensities of [C I] emission (*color*) overlaid with contours of (a) ^{12}CO 4–3, (b) ^{12}CO 1–0 and (c) ^{13}CO 1–0 integrated intensities at a common angular resolution of $70''$. The center of the maps is at $\alpha = 03^{\text{h}}44^{\text{m}}10^{\text{s}}$, $\delta = 32^{\circ}06'$ (J2000). All tracers are integrated from $V_{\text{LSR}} 2 \text{ km s}^{-1}$ to 14 km s^{-1} . Contours range between 20% to 90% with a step of 10% of the peak intensities that are 73 K km s^{-1} for ^{12}CO 4–3, 72 K km s^{-1} for ^{12}CO 1–0 and 31 K km s^{-1} for ^{13}CO 1–0. The seven filled triangles indicates the positions where I carry out a detailed PDR analysis later. The black star denotes the position of HD 281159.

5.1.2 Complementary data sets

I have used the FCRAO ^{12}CO 1–0 and ^{13}CO 1–0 datasets with an resolution of $46''$ presented by Ridge et al. (2003) for comparison. For comparison, I have smoothed all CO and C I data to a common resolution of $70''$ assuming that both the FCRAO and KOSMA telescopes have a Gaussian beam.

Further, I have obtained HIRES processed IRAS maps of the dust continuum emission at 60 and $100 \mu\text{m}$ (Aumann et al., 1990). The dust continuum maps have resolution of $1'.5$, which is comparable to the submillimeter datasets.

5.2 Observational results

Figure 5.1 presents maps of integrated intensities of [C I], ^{12}CO 1–0, ^{13}CO 1–0 and ^{12}CO 4–3 observed in IC 348. All maps are integrated over the velocity range $V_{\text{LSR}} = 2 \text{ km s}^{-1}$ to 14 km s^{-1} .

The energy of the upper level for the [C I] 1–0 transition is 24 K and the critical density for this transition is 10^3 cm^{-3} for collisions with molecular H_2 (Schröder et al., 1991). This implies that [C I] 1–0 is easily excited and the line is easily detectable even when emitted by moderate density interstellar gas exposed to the average interstellar radiation field. Previous observations have found the [C I] to

be extended and well correlated with the low- J CO emission (see a review by Preibish et al., 1996; Schneider et al., 2003; Mookerjee et al., 2006). In IC 348 the [C I] emission peaks to the south-west of the mapped region with a value of 24 K km s^{-1} and I detect [C I] emission over a large region with a homogeneous intensity distribution at a level of 65% of the peak intensity. The [C I] emission is extended towards the east and north-east of the mapped region. This is consistent with the clumpy UV irradiated cloud scenario.

Globally the ^{12}CO 4–3 emission peaks at almost the same position as [C I] with an intensity of $\sim 66 \text{ K km s}^{-1}$. However, the ^{12}CO 4–3 emission shows two additional peaks, with intensities of about two-thirds of the global peak, which lie to the north of HD 281159 (a B 5 V star) and elongated along the north-south direction. The distribution of the ^{12}CO 4–3 emission agrees very well with that of ^{12}CO 3–2 (Sun et al., 2006). I attribute the difference in the intensity distributions of [C I] and ^{12}CO 4–3 to the fact that ^{12}CO 4–3 emission arises from regions of higher temperature and density, while [C I] emission can arise also from moderate to low density embedded PDR surfaces within the molecular clouds.

The ^{12}CO 1–0 emission is similar to that of ^{12}CO 4–3, with two similar intensity peaks. The ^{12}CO 1–0 emission is more extended than the ^{12}CO 4–3 emission and this is consistent with the fact that ^{12}CO 1–0 traces lower temperature and density. The morphologies of [C I] and ^{13}CO 1–0 appear to be very similar, implying that they trace the same material and both lines are effectively column density tracers.

I selected seven positions within IC 348 for a more detailed study. Six of the seven positions are oriented along a cut from the northern edge of the cloud, past HD 281159 and into the clouds. The seventh position is at the south-east edge of the cloud. Though emission at the seventh position (southern rim) is weak, it is clearly detected. The selected positions vary in their physical and chemical conditions. Spectra of [C I], ^{12}CO 4–3, ^{12}CO 1–0 and ^{13}CO 1–0 at those seven positions are displayed in Fig. 5.2.

The [C I] emission is centered at a velocity of $\sim 8 \text{ km s}^{-1}$. The lowest [C I] main beam brightness temperature ($\sim 2 \text{ K}$) occurs at the southern rim ($9', -10'$), while the highest temperatures of 7.0 K and 6.7 K are observed at the position of the [C I] peak ($-1', -3'$) and the western rim ($-5', -7'$), respectively. The line widths of [C I] spectra at the seven positions range between 2.0 km s^{-1} and 2.6 km s^{-1} .

The ^{12}CO 4–3 main beam brightness temperature varies between $\sim 3.6 \text{ K}$ at southern rim and 16.4 K at [C I] peak. The line width of the ^{12}CO 4–3 spectra ranges between 2.0 km s^{-1} and 2.7 km s^{-1} .

Both the ^{12}CO 1–0 and ^{13}CO 1–0 spectra consist of two velocity components: one is at $\sim 7 \text{ km s}^{-1}$ and the other lies at $\sim 8 \text{ km s}^{-1}$. The two components are most prominently visible at the southern rim, map center and the [C I] peak. For the 8 km s^{-1} component at the [C I] peak, the ^{13}CO 1–0 spectrum peaks at the

dip of the ^{12}CO 1–0 spectrum, which may indicate self-absorption effect for this component.

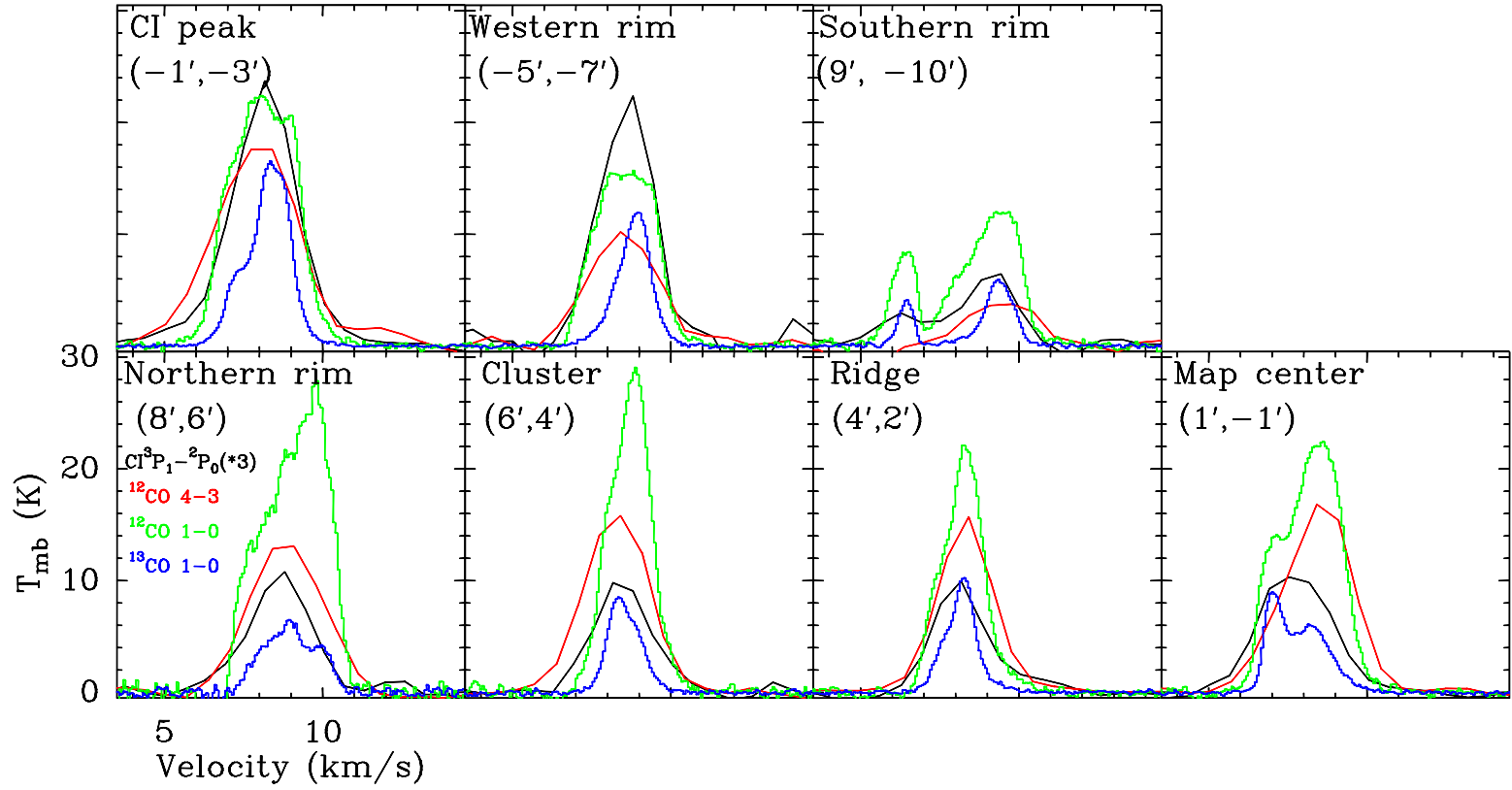


Figure 5.2: Spectra of the four different tracers on those six positions along the cut from the northern edge of the cloud into the cloud, and on the seventh position at the south of the cloud. [CI] spectra in all the positions have been multiplied by 3. All panels have the same x axis from 3.5 km s^{-1} to 14.5 km s^{-1} and the same y axis from -0.5 K to 30.5 K .

Table 5.1 presents the integrated intensities and line ratios at the seven selected positions. Figure 5.3 shows the variation of the integrated intensities and their ratios at these seven positions.

Table 5.1: The observed integrated line intensities (in $\text{erg s}^{-1} \text{sr}^{-1} \text{cm}^{-2}$) and line ratios at the seven selected positions. The errors on the integrated intensity are estimated to be $\sim 15\%$.

Position	$(\Delta\alpha,\Delta\delta)$	[C I]	$^{12}\text{CO 4-3}$	$^{12}\text{CO 1-0}$	$^{13}\text{CO 1-0}$	$\frac{[\text{C I}]1-0}{^{12}\text{CO4-3}}$	$\frac{[\text{C I}]1-0}{^{13}\text{CO1-0}}$	$\frac{^{12}\text{CO4-3}}{^{12}\text{CO1-0}}$
		$[10^{-8} \text{ erg s}^{-1} \text{ sr}^{-1} \text{ cm}^{-2}]$						
Northern rim	(8', 6')	96.56	336.43	9.59	1.74	0.29	55.51	35.07
Cluster	(6', 4')	81.99	365.30	7.14	1.41	0.22	58.01	51.15
Ridge	(4', 2')	75.09	313.20	5.37	1.61	0.24	46.59	58.38
map Center	(1',-1')	106.79	413.27	8.38	2.10	0.26	50.85	49.33
[C I] peak	(-1',-3')	226.61	548.04	9.31	3.70	0.41	61.23	58.85
Western rim	(-5',-7')	172.05	256.15	6.01	2.13	0.67	80.61	42.61
Southern rim	(9',-10')	72.71	60.21	5.50	1.35	1.21	54.02	10.95

In Fig. 5.3a I see that the intensities of [C I], ^{13}CO 1–0 and ^{12}CO 4–3 lines show similar trends, only the falling off of the intensity of ^{12}CO 4–3 is somewhat less drastic than [C I], ^{13}CO 1–0. As opposed to the single peak seen in [C I], ^{13}CO 1–0 and ^{12}CO 4–3, the ^{12}CO 1–0 intensity profile shows two peaks with comparable intensities, one at the northern rim and the other at the position of the [C I] peak.

Three independent line ratios, i.e., [C I] / ^{12}CO 4–3, [C I] / ^{13}CO 1–0 and ^{12}CO 4–3 / ^{12}CO 1–0, are presented in Table 5.1 and Fig. 5.3b (in $\text{erg s}^{-1} \text{sr}^{-1} \text{cm}^{-2}$). The largest [C I] / ^{12}CO 4–3 ratio (1.21) occurs at the southern rim and the second (0.67) and third (0.41) largest are at the western rim and [C I] peak, while the ratios at the other four positions are ~ 0.25 . When comparing with other star forming regions like W 3 Main, S 106 and Orion A etc. (see Table 3 by Kramer et al., 2004), the [C I] / ^{12}CO 4–3 ratio at the other five positions are within the range found in those star forming regions except for the western and southern rim. The highest ratio at the southern rim is close to the ratio found at the center of M 51 and the nucleus position of NGC 4826 (Israel & Baas., 2002). The ^{12}CO 4–3 / ^{12}CO 1–0 ratio peaks at [C I] peak and decreases for the positions further away with increasing distance. The [C I] / ^{13}CO 1–0 ratios are rather constant except for the western rim.

5.3 LTE Analysis

Figure 5.4 shows a map of the ^{12}CO 4–3 / ^{12}CO 1–0 line ratio in terms of line integrated temperatures (K km s^{-1}) overlaid by ^{12}CO 4–3 integrated intensities. The ratio has its minimum of ~ 0.3 at the edges of the cloud; ratios of ~ 0.9 are found at the ^{12}CO 4–3 peaks; maximum ratios between 1.1 and 1.5 occur close to HD 281159.

I first apply a Local Thermodynamic Equilibrium analysis as a simple approach to obtain the excitation conditions in the IC 348 cloud.

Assuming LTE and optically thick emission, the ^{12}CO 4–3 / ^{12}CO 1–0 ratio of 0.3 corresponds to an excitation temperature T_{ex} of ~ 10 K. The ratio grows to 0.85 for $T_{\text{ex}} \sim 50$ K and remains almost constant at even higher temperatures. Considering the calibration uncertainty, I set T_{ex} to 50 K in all the positions where the ratio falls above 0.85. I note that [C I] and ^{12}CO often have different excitation temperatures. However, $N(\text{C})_{\text{LTE}}$ only changes within 20% when the assumed excitation temperature varies between 20 and 150 K. So it is reasonable to assume that [C I] has the same excitation temperature as ^{12}CO for the first order estimation.

Using the temperature derived from the LTE estimate, I can compute the C column density, $N(\text{C})_{\text{LTE}}$, and the CO column density, $N(\text{CO})_{\text{LTE}}$, from the [C I]

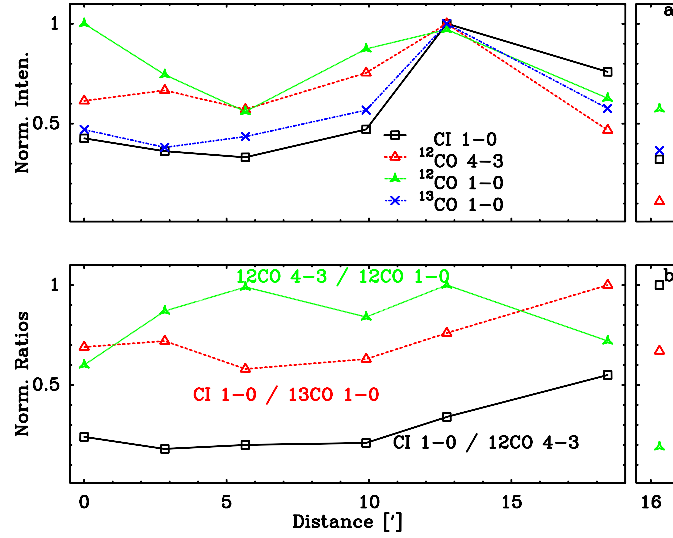


Figure 5.3: The top panel (a) presents the normalized integrated intensities of [C I], ^{12}CO 4-3, ^{12}CO 1-0 and ^{13}CO 1-0 in the seven selected positions. The typical errors of the intensities are about 15%; (b) displays integrated line intensity ratios. The x axes of all panels are the relative distance to the northern rim (8', 6') position. The southern rim is plotted in a separate box.

and ^{13}CO 1-0 line intensities assuming that both lines have the same excitation temperature as ^{12}CO and that they are optically thin.

I apply the relative abundance ratio $[\text{C I}]/[\text{CO}]$ of 65 (Langer et al., 1990) to translate ^{13}CO column densities into CO column densities. From the relative abundance ratio $[\text{CO}]/[\text{H}_2]$ of 8×10^{-5} (Frerking et al., 1982), I also derive the H_2 column density (see Table 5.2).

The resulting map of C/CO column density ratios is presented in Fig. 5.5. In most of the cloud, the C/CO ratio falls below 0.1. Higher values (up to 1.5) occur at the rim of the cloud where the ^{13}CO 1-0 emission is more diffuse. Values as low as 0.02 are found at the south-west of the cloud and along the ridge to the north-east. As ^{13}CO 1-0 roughly traces the H_2 column density, this plot indicates an anti-correlation between the C/CO ratio and the H_2 column density. The results are consistent with the conclusion of Mookerjee et al. (2006) that the [C I] line is not a tracer of optical extinction, total H_2 column density or total mass in the beam.

The seven positions, for which I will perform a detailed analysis within the context of a PDR model, exhibit C/CO column density ratios between about 0.05 and 0.5, i.e. they cover a relatively wide range (see Table 5.2).

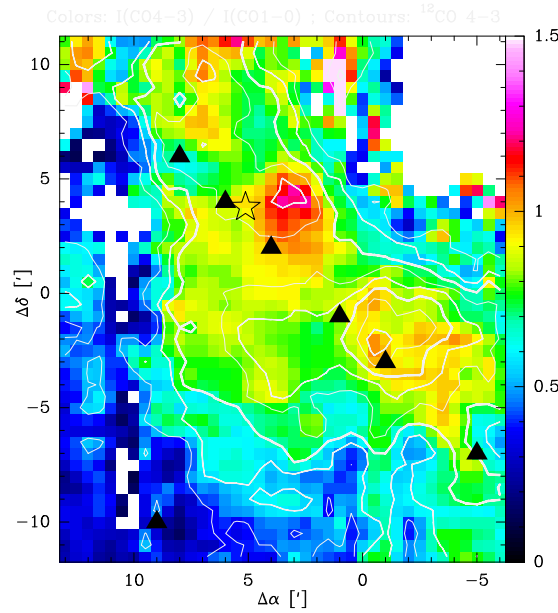


Figure 5.4: The color plot represents the ^{12}CO 4–3 / ^{12}CO 1–0 line intensity ratio (in units of K km s^{-1}) observed in the IC 348 cloud. The contours show the ^{12}CO 4–3 line intensity spaced at 10% intervals from 20% to 90% relative to the peak intensity of 73 K km s^{-1} . For line ratios, I only calculate for the positions where the line intensities of both tracer are larger than each 3 sigma value.

Table 5.2: Results of the LTE analysis. The excitation temperature T_{ex} is listed in Column (2); Column (3) - (5) present C, CO and H_2 column densities; the C/CO ratio is listed in Column (6). The uncertainties of the column densities are derived by varying the integrated intensities by $\pm 15\%$.

number	T_{ex} K	$N(\text{C})_{\text{LTE}}$ $10^{16}[\text{cm}^{-2}]$	$N(\text{CO})_{\text{LTE}}$ $10^{17}[\text{cm}^{-2}]$	$N(\text{H}_2)_{\text{LTE}}$ $10^{21}[\text{cm}^{-2}]$	$\text{C}/\text{CO}_{\text{LTE}}$
Northern rim	18^{47}_{15}	$12.08^{19.71}_{9.27}$	$9.56^{22.84}_{7.16}$	$12.50^{28.55}_{8.95}$	$0.13^{0.28}_{0.04}$
Cluster	50^{20}_{20}	$9.61^{11.17}_{7.77}$	$16.99^{19.54}_{7.33}$	$21.24^{24.43}_{9.16}$	$0.06^{0.15}_{0.04}$
Ridge	50^{28}_{28}	$9.04^{10.46}_{7.32}$	$19.37^{23.03}_{10.43}$	$24.21^{28.78}_{13.04}$	$0.05^{0.10}_{0.03}$
Map center	48^{50}_{18}	$13.09^{16.00}_{10.68}$	$24.39^{29.03}_{10.25}$	$30.49^{36.29}_{12.82}$	$0.05^{0.16}_{0.04}$
[C I] peak	50^{29}_{29}	$26.85^{30.88}_{21.71}$	$44.47^{51.14}_{24.56}$	$55.59^{63.93}_{30.70}$	$0.06^{0.13}_{0.04}$
Western rim	28^{50}_{15}	$19.72^{28.30}_{17.61}$	$16.25^{29.99}_{9.52}$	$20.31^{37.49}_{11.90}$	$0.12^{0.30}_{0.06}$
Southern rim	7^{8}_{6}	$37.50^{72.57}_{21.96}$	$6.66^{8.54}_{5.40}$	$8.32^{10.67}_{6.76}$	$0.56^{1.34}_{0.26}$

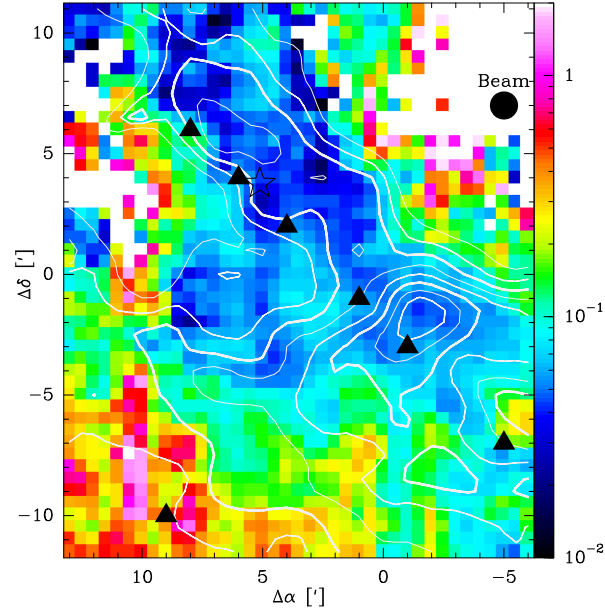


Figure 5.5: The C/CO column density ratio overlaid by ^{13}CO 1–0 integrated intensities contours. The contour levels are spaced at 10% intervals from 20% to 90% relative to the peak intensity of 31 K km s^{-1} . For column density ratios, I only calculate for the positions where the line intensities of ^{13}CO 1–0 are above the 3 sigma value.

5.4 PDR Model

I use the KOSMA - τ PDR model (Störzer et al., 1996; Röllig et al., 2006, 2007) to derive the physical conditions from the observed molecular and atomic emission lines in IC 348.

In the following, I first estimate the FUV field in IC 348 using the FIR continuum and the stellar radiation; then I compare the emission from an ensemble of PDR model clumps with the observed line intensity ratios to reproduce the observed absolute intensity. In the clumpy PDR scenarios, two clump ensembles are used: an ensemble of identical clumps and an ensemble with a distribution of clumps over a range of masses and sizes.

5.4.1 FUV intensity

5.4.1.1 Estimate from the FIR continuum

I use HIRES processed 60 and 100 μm IRAS data (Aumann et al., 1990) to generate a far-infrared intensity map I_{FIR} in IC 348. It represents the far-infrared intensity between 42.5 μm and 122.5 μm as measured by the two IRAS data sets (Nakagawa et al., 1998). Following Kaufman et al. (1999), I assume that the total FUV flux, χ_{FIR} , absorbed by the dust grains is re-radiated in the far-infrared. In this way I estimate the FUV field from the far-infrared field (cf. Kramer et al., 2005): $\chi_{\text{FIR}}/\chi_0 = 4\pi I_{\text{FIR}}$, where $\chi_0 = 2.7 \times 10^{-3} \text{ erg s}^{-1} \text{ cm}^{-2}$ (Draine, 1978; Draine & Bertoldi, 1996). The derived spatial distribution of the FUV intensity is presented in Fig. 5.6. In the mapped region, the FUV field χ_{FIR} varies between about 1 and 100 Draine units. For the seven selected positions χ_{FIR} is listed in Table 5.3.

5.4.1.2 Estimate from the stellar radiation

The primary source of UV radiation in the cloud is HD 281159. Assuming that the star is a black body at an effective temperature T_{eff} corresponding to its spectral type, I can estimate the FUV flux independently (Kramer et al., 1996; Beuther et al., 2000). A B5 V star has an effective temperature $\log(T_{\text{eff}}) = 4.182$ and a total luminosity L of $\log(L/L_{\odot}) = 2.681$ (de Jager & Nieuwenhuijzen, 1987). The FUV luminosity L_{FUV} and the FUV flux χ_{FUV} are defined as

$$L_{\text{FUV}} = L \cdot \frac{\Phi_{\text{UV}}}{\Phi_{\text{total}}}, \text{ and } \chi_{\text{FUV}} = \frac{L_{\text{FUV}}}{4\pi d^2}, \quad (5.1)$$

where Φ_{UV} is the FUV flux between 6 eV and 13.6 eV, Φ_{total} is the total flux, and d is the distance to the UV source. I compute the distance d in two ways: for the

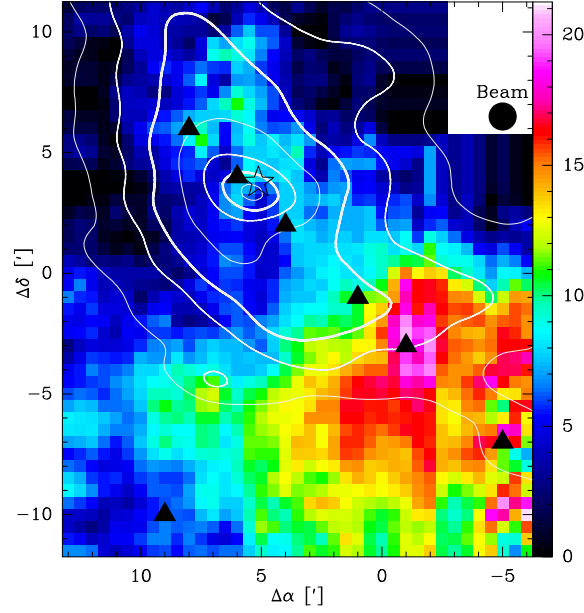


Figure 5.6: FUV intensity distribution (contours) in IC 348 estimated from the IRAS FIR fluxes, overlaid on the [C I] integrated intensities (colors). The FUV intensity χ_{FIR} contour levels run from 5, 10, 20 to 100 by steps of 20 Draine units, χ_0 .

point close to HD 281159 I use the optical radius of the cluster IC 348 of about 0.37 pc (Herbig, 1998) as the minimum distance between star and cloud. For all other points I assume that star and cloud are located in the same plane so that the distance is directly given by the observed separation. Finally I normalize the FUV field to units of χ_0 . The resulting FUV fields, χ_{star} , are also listed in Table 5.3 for the seven selected positions.

I see that both methods provide consistent FUV field values. Because of the uncertainty of the distance between star and cloud I consider the values χ_{FIR} , derived from the HIRES data, somewhat more reliable so that I will use them in the following. The FUV field χ at the seven positions ranges from about 1 to 90 Draine units.

In the next step I attempt to obtain a self-consistent model of the chemical and excitation structure of the cloud matching the observed C/CO ratios.

5.4.2 Clumpy PDR scenarios

Molecular clouds has been observed to be highly filamentary and clumpy, and often show self-similar structure over a wide range of scales (Dame et al., 2001; Heyer et al., 1998; Stutzki et al., 1988). Many theoretical work suggests that mag-

netic fields and/or turbulence can be proposed to influence the formation of molecular cloud filaments (Gehman et al., 1996; Nakajima & Hanawa, 1996; Padoan et al., 1998; Fiege & Pudritz, 2000; Klessen & Burkert, 2000; Ostriker et al., 2001). Furthermore, the observed structure further breaks up into substructures with increasing spatial resolution (Falgarone & Phillips, 1996; Bensch et al., 2001). So molecular clouds are filled with internal surfaces (Ossenkopf et al., 2007). This explains that [C I] acts as a molecular cloud volume tracer rather than a surface tracer, and [C II] emission extends far into molecular clouds which could not be explained by assuming a homogeneous cloud. The [C II] emission distribution can be well modelled within a clumpy cloud scenario (Stutzki et al., 1988; Howe et al., 1991; Stacey et al., 1993; Meixner & Tielens, 1993). In a clumpy cloud, the UV field can penetrate deep into the cloud and forms PDRs on the surface of the clumps. It is necessary to consider a clumpy molecular cloud structure.

I here apply two different clump ensembles to reproduce the observed line intensity ratios and absolute line intensities.

5.4.2.1 Ensemble of identical clumps

In the following, I first compare the emission from individual PDR model clumps to the observed line intensity ratios, then expand the analysis to an ensemble of identical clumps, to also reproduce the observed absolute intensity.

Single spherical PDR model. I perform a χ^2 fitting of the three line intensity ratios given in Table 5.1, using a single spherical PDR model, to determine the densities, FUV fields, and clump masses. Figure 5.7 presents an example of the χ^2 fitting for the map center ($1', -1'$). The left panel shows the fitting of clump mass M_{cl} and clump density n_0 and the right panel presents the fitting to obtain the FUV field χ and the clump density n_0 . It shows that all line ratios are good density tracers, but do not constrain the clump masses. The clump density is well constrained within $2.5 - 5.0 \cdot 10^5 \text{ cm}^{-3}$. But the reduced χ^2 changes only upto 2.5 when the clump mass varies from $10^{-2.0}$ to $10^{1.0} M_\odot$, when the clump density is kept at $10^{5.6} \text{ cm}^{-3}$ (see the left panel of Fig. 5.7).

The results from the single spherical PDR clump model analysis are presented in Table 5.3. The fitted FUV flux χ_{PDR} agrees with χ_{FIR} derived from the FIR continuum. The largest deviations differ by a factor of only 3.

The clump densities at the seven positions vary between $4.4 \cdot 10^4$ to $4.3 \cdot 10^5 \text{ cm}^{-3}$ and the highest clump density occurs at positions of the ridge and the map center. Though the clump masses are not well constrained, the best fitting clump masses lie between 0.1 and $0.4 M_\odot$.

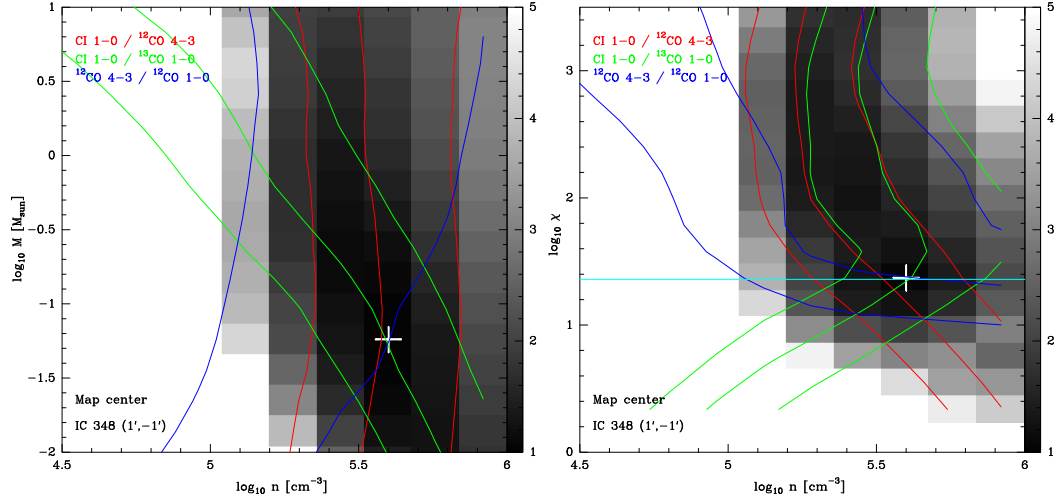


Figure 5.7: Comparison of the observed line intensity ratios $[\text{C I}]/^{12}\text{CO 4-3}$, $[\text{C I}]/^{13}\text{CO 1-0}$ and $^{12}\text{CO 4-3}/^{12}\text{CO 1-0}$ at $(1', -1')$ with the single clump KOSMA - τ PDR model calculations. The left figure shows the fitting of a clump mass and densities; the right one presents the fitting of the FUV field and clump densities. The middle drawn contours are the observed intensity ratios, and the outer two are those for the 20% uncertainty. The grey-scale images indicate the reduced χ^2 of the fit. The position of the minimum reduced χ^2 is marked using a white cross. The horizontal light blue line in the right panel shows the FUV flux χ_{FIR} from the HRES data.

Table 5.3: Physical parameters at selected positions in Fig 5.1, obtained by fitting the observed intensity ratios to the **single clump** KOSMA - τ PDR models. Columns (2) - (5) list the fitted clump densities, clump mass, clump radius and FUV field; the derived FUV field from the HIRES data and from the star are in Column (6) and (7); The distance to HD 281159 used for the calculation of χ_{star} is listed in Column (8); Column (9) is the minimum chi square of the PDR fit.

Position	n [10^5cm^{-3}]	M_{cl} M_{\odot}	R_{cl} pc	χ_{PDR}	χ_{FIR}	χ_{star}	d pc	χ_{min}^2
Northern rim	1.91	0.2	0.01	15	39	40	0.37	1.38
Cluster	2.75	0.1	0.01	98	84	40	0.37	1.05
Ridge	4.25	0.4	0.01	38	46	40	0.37	1.23
Map center	3.98	0.1	0.01	23	23	13	0.64	1.04
[C I] peak	1.91	0.1	0.02	23	11	7	0.90	1.96
Western rim	0.63	0.2	0.02	20	6	3	1.42	2.00
Southern rim	0.44	0.4	0.02	2	1	3	1.29	2.31

The clump masses of the best fit vary between $0.1 M_{\odot}$ and $0.4 M_{\odot}$ (Table 5.3), while the LTE analysis indicates that the total mass in the beam is a few solar masses. After correcting for beam and velocity filling, the absolute line intensities from the single spherical PDR model are much smaller than the observations. The single spherical PDR model constrains the clump density and FUV field well, but fails to explain the observed absolute line integrated intensities. An ensemble of clumps within the beam is needed, the intensities of which accumulate to the observed absolute intensity within the beam.

Ensemble of identical clumps. I consider an ensemble of identical clumps (hereafter Ensemble case 1). The total number of clumps in the beam N_{ens} is calculated from the comparison of the absolute line integrated intensities from the observations and models, correcting for both the velocity filling factor and the beam filling factor. The observed [C I] full width at half maximum (FWHM) Δv_{obs} varies from 2.0 to 2.6 km s⁻¹. The velocity dispersion of the gas of the KOSMA - τ model clump has a Gaussian FWHM of $\Delta v_{\text{mod}} = 1.7 \text{ km s}^{-1}$. The velocity filling factor is automatically taken into account by using line integrated intensities. A 70'' beam corresponds to a diameter of 0.10 pc at the distance of IC 348. The clump size obtained from the best fit models found in the previous section ranges from 0.01 to 0.02 pc. The beam filling factor $\eta_{\text{bf},i}$ of each clump is calculated as $\eta_{\text{bf},i} = \Omega_{\text{cl}}/\Omega_{\text{beam}}$, where Ω_{cl} and Ω_{beam} are the solid angles of a clump and the beam. $\Omega_{\text{cl}} = \pi R_{\text{cl}}^2/d^2$ is the solid angle of the individual clump and is the quantity to which the model output intensities are referred. d is the distance of the cloud; assuming a Gaussian beam shape, Ω_{beam} is computed as $\Omega_{\text{beam}} = \pi \theta_{\text{beam}}^2/4 \ln 2$, where θ_{beam} is the FWHM of the beam. The intensity correction for a single clump is $I'_i = I_{\text{mb},i}/\eta_{\text{bf},i}$, where $I_{\text{mb},i}$ is the beam averaged line intensity for that single clump. Since [C I] is the most optically thin one among the four tracers, I use its line intensity to derive the number of clumps in the beam N_{ens} (see Table 5.4) by dividing the observed intensities $I_{[\text{C I}]\text{obs}}$ by the intensities for a single clump $I_{[\text{C I}]\text{mod},i}$, corrected for both the velocity and beam filling, i.e.,

$$N_{\text{ens}} = \frac{I_{[\text{C I}]\text{obs}}}{I_{[\text{C I}]\text{mod},i} * \eta_{\text{bf},i}} = \frac{I_{[\text{C I}]\text{obs}}}{I_{[\text{C I}]\text{mod},i}} \times \frac{\Omega_{\text{beam}}}{\Omega_{\text{cl}}}. \quad (5.2)$$

Table 5.4: Results of ensemble of identical clumps, **Ensemble case 1**. The mass and FUV field for each single clump are listed in Column (2) and (3); Column (4) - (6) present the line intensity ratios between the ensemble models and observations of ^{12}CO 4–3, ^{12}CO 1–0 and ^{13}CO 1–0; The C, CO and H_2 column densities from the ensembles are presented in Column (7), (8) and (9); Column (10) is the C/CO ratios. The total number of the clumps in the ensemble and ensemble mass are listed in Column (11) and (12) The total ensemble mass M_{ens} listed in the table is computed as $M_{\text{ens}} = N_{\text{ens}} \times M_{\text{cl}}$, where M_{cl} is the mass of a clump.

Position	M_{cl} M_{\odot}	χ_{cl}	$R_{^{12}\text{CO}4-3}$	$R_{^{12}\text{CO}1-0}$	$R_{^{13}\text{CO}1-0}$	$N(\text{C})_{\text{ens}}$ $10^{16}[\text{cm}^{-2}]$	$N(\text{CO})_{\text{ens}}$ $10^{17}[\text{cm}^{-2}]$	$N(\text{H}_2)_{\text{ens}}$ $10^{21}[\text{cm}^{-2}]$	C/CO_{ens}	N_{ens}	M_{ens} M_{\odot}
Northern rim	0.32	10	0.63	0.67	0.87	13.97	18.58	7.72	0.075	4.59	1.47
Cluster	0.10	100	1.07	0.99	1.13	10.02	21.56	8.90	0.046	16.75	1.68
Ridge	0.32	32	0.95	1.13	0.95	8.90	29.49	11.29	0.030	6.72	2.15
Map center	0.10	32	0.94	1.05	0.97	13.25	34.24	13.05	0.039	24.56	2.46
[C I] peak	0.10	32	0.94	1.59	0.83	31.54	29.88	13.14	0.106	24.74	2.47
Western rim	0.10	10	0.78	1.43	0.71	24.52	9.33	6.10	0.263	11.51	1.15
Southern rim	0.32	1	0.84	0.81	0.74	14.62	6.28	3.03	0.233	5.70	1.82

Then I use N_{ens} to calculate the ratios R of line intensities between model ensemble and observations for the four tracers, where R is defined as follows:

$$R = \frac{N_{\text{ens}} \cdot I_{\text{mod},i}}{I_{\text{obs}}} \quad (5.3)$$

This allows easy judgment of the quality of the model fit, as a R value unity means that the model predicts exactly the observed intensity. I list the ratios of the remaining three tracers in Table 5.4. Considering the calibration uncertainty, a perfectly fitting model will yield a ratio R of 1 ± 0.15 . All three remaining tracers from Ensemble case 1 have a good agreement between the modelled and observed absolute line intensities.

5.4.2.2 Ensemble of power law clump mass distribution

Large-scale CO maps present the clumpy structure of the ISM with a mass distribution following a power law $dN/dM \propto M^{-\alpha}$, where N is the number of clumps and α has a value around 1.8 (Kramer et al., 1998b). Furthermore, the observations also show that there is a strong correlation of the density and mass of the clumps corresponding a mass-size relation $r \propto M^\gamma$ with $\gamma \approx 2.3$ (Heithausen et al., 1998). For an ensemble of randomly positioned clumps with a power law mass spectrum, there is a relation among the power law spectral index β of the power spectrum, α and γ : $\beta = \gamma(3 - \alpha)$ (Stutzki et al., 1998). Using the α and γ values above, $\beta = 2.76$, which is close to the power law index $\beta = 2.71$ of ^{13}CO 2–1 in IC 348 found by Sun et al. (2006).

I assume these characteristics to be universal and model the emission by ensemble averaging the PDR single clump results over such a clump distribution (Cubick, 2005; Cubick et al., 2008) (hereafter Ensemble case 2) to reproduce the observed line intensities. The mean solid angle Ω_i of each clump size at the given distance is evaluated to calculate the total flux F of the clump ensemble by using $F = \sum_i \Omega_i I_i$, where I_i are the clump integrated intensities. The mean intensity of the ensemble results in $I = F/\Omega_{\text{beam}}$, where Ω_{beam} is the beam solid angle.

The input parameters for the ensemble routines are the total mass within the beam M_{ens} ; the mean clump ensemble density n_{mean} ; the FUV field input χ_{ens} and the minimum and maximum clump mass, $m_{\text{cl}}^{\text{min}}$ and $m_{\text{cl}}^{\text{max}}$.

The total mass within the beam is initially set to be half of the total mass estimated from Ensemble case 1. at last, I obtain the total mass within the beam by comparing the observed absolute line intensity of [C I]. The upper mass limit, $m_{\text{cl}}^{\text{max}}$, is set close to the initial total mass. I set the lower mass limit, $m_{\text{cl}}^{\text{min}}$, to $10^{-2} M_\odot$. Considering that clumps have a FWHM of $\Delta v_{\text{mod}} = 1.7 \text{ km s}^{-1}$ in the KOSMA - τ model, I calculate the virial mass of the smallest clump, $M_{\text{vir}} \propto R \Delta v_{\text{mod}}^2$. The resulting virial mass is a factor of 400 larger than the smallest

clump. Such large ratio indicates that these small clumps can only exist transiently and evaporate on a time scale of ~ 5000 yrs Kramer et al. (2008).

The model output is insensitive to the value assumed for the lower and upper mass limits of the ensemble. Cubick et al. (2008) studied the dependencies of the clump model output from the upper and lower clump mass limits. They have found that some tracers, such as the high - J CO (like ^{12}CO 8–7), [C II] and [O I], are sensitive to the upper and lower clump mass limits. However, for the five tracers that I studied here, the modelled intensities change only by less than a factor of ~ 2 relative to the best fitting solution when varying one of the mass limits by one order of magnitude (Kramer et al., 2008; Cubick et al., 2008).

Similar to the single clump PDR analysis, I compare the observed line ratios with the results of Ensemble case 2 to fit the mean clump ensemble density and the FUV field. I compute the line intensities of all the remaining tracers with the same model (see Table 5.5). The beam averaged H_2 , C and CO column densities can be calculated as:

$$N(X)_{\text{ens}} = \sum N_i \cdot \eta_{\text{bf},i} \cdot N(X)_i; \quad (5.4)$$

where N_i and $N(X)_i$ are the number of clumps in each clump mass bin and the column density of tracer X of a single clump, respectively. $\eta_{\text{bf},i}$ is the beam filling factor for each clump. The results are presented in Table 5.5.

Table 5.5: Results of ensembles with a clump mass distribution and mass-size distribution, **Ensemble case 2**. Column (2) - (4) present the ratios (in $\text{erg s}^{-1} \text{sr}^{-1} \text{cm}^{-2}$) of the modelled and observed line intensities for ^{12}CO 4–3, ^{12}CO 1–0 and ^{13}CO 1–0; The mean clump ensemble density n_{mean} and the fitted FUV field χ_{ens} are presented in Column (5) and (6). The C, CO and H_2 column densities from the ensembles are presented in Column (7), (8) and (9); Column (10) is the C/CO ratios. The total masses are listed in Column (11).

Position	$R_{^{12}\text{CO}4-3}$	$R_{^{12}\text{CO}1-0}$	$R_{^{13}\text{CO}1-0}$	n_{mean} [10^5cm^{-3}]	χ_{ens}	$N(\text{C})_{\text{ens}}$ $10^{16} [\text{cm}^{-2}]$	$N(\text{CO})_{\text{ens}}$ $10^{17} [\text{cm}^{-2}]$	$N(\text{H}_2)_{\text{ens}}$ $10^{21} [\text{cm}^{-2}]$	C/CO_{ens}	M_{ens} M_{\odot}
Northern rim	1.00	1.04	1.44	3.2	3	14.36	51.82	19.28	0.028	3.84
Cluster	1.06	1.03	1.13	3.2	100	9.88	25.58	9.93	0.039	1.97
Ridge	1.13	1.26	0.91	3.2	32	9.05	23.43	9.10	0.039	1.83
Map center	1.08	1.19	1.08	3.2	10	13.78	40.71	15.39	0.034	3.07
[C I] peak	1.13	1.73	0.86	1.0	10	31.24	40.16	16.61	0.078	2.88
Western rim	1.83	2.03	1.13	1.0	10	30.49	23.72	12.61	0.078	2.19
Southern rim	1.06	0.84	0.66	0.3	1	13.58	5.24	2.62	0.259	0.53

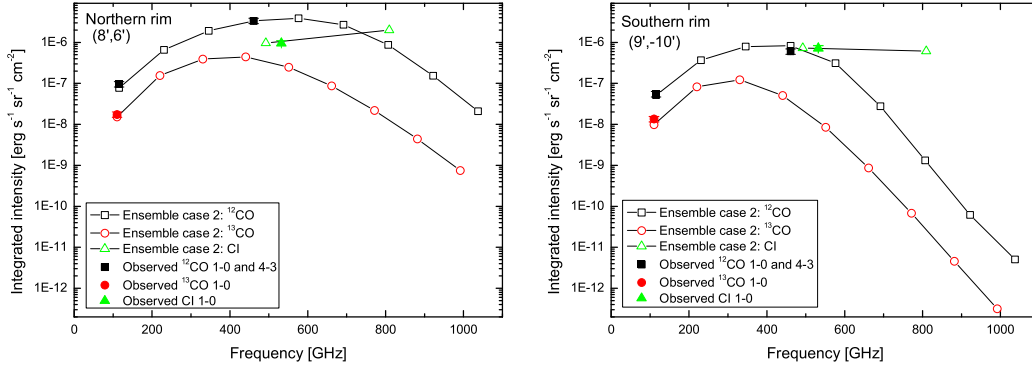


Figure 5.8: Observed (filled symbols) and modelled (drawn lines with open symbols) line intensities of ^{12}CO , ^{13}CO , and $[\text{C I}]$ from Ensemble case 2 at the northern rim (left panel) and the southern rim (right panel). To better display the data, I artificially shift the $[\text{C I}]$ frequency by +40 GHz for the observed intensity.

Table 5.5 shows a reasonable agreement between the modelled line intensities from Ensemble case 2 and the observed ones. The intensity ratios between Ensemble case 2 and observations range between 0.7 and 2.0. The fit is not better than for an ensemble of identical clumps (Ensemble case 1).

To compare the observed absolute line intensities with the model prediction from Ensemble case 2, I show two examples of observed and modelled integrated intensities versus frequency, i.e. the cooling curves of ^{12}CO , ^{13}CO (upto $J = 9-8$) and $[\text{C I}]$ for the best-fit Ensemble case 2 model at the northern rim and the southern rim (see Fig. 5.8). At those two positions the modelled and observed line intensities agree very well. Fig. 5.8 also provides a prediction for line intensities of $[\text{C I}]$ $^3\text{P}_2 - ^3\text{P}_1$, ^{12}CO 7-6, ^{13}CO 8-7 and etc.

Based on the CO and H_2 column densities from the PDR analysis, I find the averaged CO relative abundance $[\text{CO}]/[\text{H}_2]$ is $\sim 2.4 \cdot 10^{-4}$, which is 3 times larger than the canonical ratio $[\text{CO}]/[\text{H}_2]$ of $8 \cdot 10^{-5}$ (Frerking et al. , 1982) that I used in the LTE analysis.

The beam averaged C/CO abundance ratio (Table 5.5) varies by a factor 10 between 0.03 at the northern rim, which shows the highest column density of all studied positions of $2 \cdot 10^{21} \text{ cm}^{-2}$, and 0.26 at the southern rim, which shows the lowest H_2 column density of $3 \cdot 10^{21} \text{ cm}^{-2}$. The observed anti-correlation between C/CO and $\text{N}(\text{H}_2)$ and also the absolute values resemble those found in many other Galactic molecular clouds as compiled recently by Mookerjee et al. (2006). They used the KOSMA- τ model to interpret data taken in the Cepheus B star forming region. They suggested that the emission of high column density peaks is dominated by massive clumps exhibiting low C/CO ratios, while positions of low col-

umn densities are dominated by smaller clumps, exhibiting higher C/CO ratios. This scenario is confirmed in IC 348 by a more complete analysis using clump mass ensembles following the canonical mass and size distributions. However, the scatter of the present data is large. Observations of an optical thin tracer like $C^{18}O$ and observations of the higher lying transitions of $[C\ I]$ and CO are needed to further improve the analysis.

5.5 Summary and Conclusions

I have presented fully sampled $[C\ I]$ and ^{12}CO 4–3 maps of the IC 348 molecular cloud, covering a region of $20' \times 20'$. The observed ^{12}CO 4–3/ ^{12}CO 1–0 ratios vary between 0.2 and 1.5. High ^{12}CO 4–3/ ^{12}CO 1–0 ratios occur near the B 5 star, at the cloud center and northern edge of the cloud.

I have estimated the FUV field from the FIR continuum intensities obtained from the 60 and 100 μm HIRES/IRAS images. The FUV field in the whole observed region ranges between 1 and 100 Draine units. I also used HD 281159, the primary source of UV radiation in this region, to estimate the FUV field for the seven studied regions and the FUV field varies between 3 to 40 Draine units.

I applied the KOSMA - τ PDR model at seven selected positions by examining the three independent line ratios: $[C\ I] / ^{12}CO$ 4–3, $[C\ I] / ^{13}CO$ 1–0 and ^{12}CO 4–3 / ^{12}CO 1–0 to derive the local physical condition. First I compared the emission from individual PDR model clumps to the observed line intensity ratios. The clump density in those seven positions falls between $4.4 \times 10^4 \text{ cm}^{-3}$ and $4.3 \times 10^5 \text{ cm}^{-3}$. The FUV field fitted from the model is between 2 to 100 Draine units, consistent within a factor of 3 with independent estimates for the FUV field derived from the FIR continuum maps by IRAS and from the stellar radiation.

The single spherical PDR model constrains the clump density and FUV field well, although it fails to explain the observed absolute line integrated intensities. Hence I expanded the analysis to an ensemble of identical clumps (Ensemble case 1) and furthermore I considered a distribution of clumps over a range of masses and sizes (Ensemble case 2). Both Ensemble case 1 and Ensemble case 2 produce model line intensities which are in good agreement to within a factor of ~ 2 with the observed intensities. I also predicted the line intensities for $[C\ I] \ ^3P_2 - ^3P_1$, ^{12}CO 7–6, ^{13}CO 8–7 and etc., which can be confirmed by the future observations.

By using a more complete analysis of clump mass ensembles following the canonical mass and size distributions, I confirmed the anti-correlation between C/CO abundance ratio and hydrogen column density found in many regions and explained by Mookerjea et al. (2006).

In the next chapter, I will present the results on a multi-line study in another nearby star forming region: Cepheus B.

Chapter 6

Multi-line study of the Cepheus B cloud

The Cepheus B cloud, at a distance of 730 pc (Blaauw, 1964) is a typical example for triggered star formation. To the north-west lie the [H II] region S 155 and the Cepheus OB3 association. The primary sources of UV radiation are an O7 star at a distance of ~ 1.2 pc to the north-west of the hot core position, and a B1 star at a projected distance of 0.7 pc to the west. Based on the FIR continuum, the FUV radiation field varies between 1500 Draine units at the interface and ~ 25 Draine units in the inner core (Mookerjea et al., 2006). The proximity of Cepheus B allows to spatially resolve the PDR: $10''$ correspond to 0.035 pc. Hence, the Cepheus B cloud represents the class of PDRs with moderately strong UV field.

Following up on the previous low-resolution ($\sim 1'$) studies of low - J CO, [C II] and far-infrared continuum (Beuther et al., 2000; Mookerjea et al., 2006), I try to understand photo-induced chemistry of the photon dominated regions using the higher resolution ($\sim 20''$) molecular line data at 3 mm and 1 mm data observed with the IRAM 30m telescope at Pico Veleta. The aim of the study is to resolve the temperature, chemical, and excitation structure of the transition zone from the [H II] region to the dense molecular cloud in a PDR which is subject only to moderately strong UV fields.

In this chapter, I study two cuts through the interfaces into the main cloud. Particularly, I select two positions at the interface for more detailed studies (see Fig. 6.1). The study covers the frequency range from 85 GHz to 272 GHz and includes 21 transitions of 13 molecules and their isotopomers: HCN, H^{13}CN , HNC, HCO^+ , H^{13}CO^+ , HCO, CN, CS, C^{34}S , C_2H , C_2S , HCS^+ and $\text{c-C}_3\text{H}_2$. Combined with low - J CO maps of this region (Ungerechts et al., 2000), I calculate the integrated intensity distribution along the cuts and line ratios between different tracers and transitions. The H_2 column density along the cuts has been estimated under the Local Thermodynamic Equilibrium assumption. The integrated line intensi-

ties shows a clear change from the [H II] region into the molecular clouds. There is an intensity enhancement of all the tracers at the two interface positions.

Observations are presented in Section 1; Section 2 describes the diagnostic values of the observed tracers; The selection of the two cuts is presented in Section 3; The spectral results and a basic LTE analysis are presented in Section 4. Section 5 is the summary and an outlook for future studies.

6.1 The IRAM 30m telescope observations

I carried out a molecular line survey with the IRAM 30m telescope at Pico Veleta (Spain) in one week during July and August 2006. I observed two cuts running through the interfaces (between S 155 and the Cepheus B cloud) into the main cloud and thus allow to trace several interface regions. Particularly, I select two positions at the interface for a more detailed study. The studied frequency covers from 85 GHz to 272 GHz and includes 21 transitions of 11 molecules, such as HCN, HCO^+ , CN, CS and CCH (See Table 6.1).

I used all the eight receivers for the observations and a maximum of four heterodyne receivers can be used simultaneously. Those eight receivers are A 100, B 100, C 150, D 150, A 230, B 230, C 270 and D 270. The numbers indicate the typical frequency for each receiver. During the observations, I used both the 1 MHz backends (resolution 1 MHz) with an effective total bandwidth of 512 MHz and VESPA with a resolution of 3.3 kHz - 1.25 MHz and bandwidth of 10 - 512 MHz. The HPBW of each frequency can be well fit by: $\text{HPBW}('') = 2460/\text{freq}(\text{GHz})$. The beam efficiency B_{eff} can be calculated by $B_{\text{eff}} = 0.828 \exp[-(0.28\pi/\lambda)^2]$. The forward efficiency F_{eff} is 0.95 for receiver A 100 and B 100, 0.93 for receiver C 150 and D 150, 0.91 for receiver A 230 and B 230, and 0.88 for receiver C 270 and D 270. Using the beam efficiency and the forward efficiency F_{eff} , I convert the data to main beam temperature scales.

6.2 Chemical tracers at the PDR interfaces

Recent observations of photon dominated regions have revealed an unexpected richness in chemical species. The CF^+ ion (Neufeld et al., 2006) and DCN (Leurini et al., 2006) have been detected in the Orion Bar region. Moreover, a number of carbon chain molecules and other carbon-rich species, such as C_2H , C_4H and $\text{c-C}_3\text{H}_2$ have been detected toward several spots in IC 63, L 1688-W and the Horsehead nebula with abundances that are often close to those in the TMC-1 dark cloud. HC_3N was only observed toward the Hydrocarbon peak of the latter while both C_3H isomers have been seen only toward the IR peak (Teyssier et

Table 6.1: Rest frequencies of observed spectral lines

Molecule	Transition	Rest frequency [GHz]
HCN	J=1-0	88.6316
	J=2-1	177.2611
	J=3-2	265.8864
H ¹³ CN	J=1-0	86.3399
HNC	J=1-0	90.6636
	J=2-1	181.3248
	J=3-2	267.5575
HCO ⁺	J=1-0	89.1885
	J=2-1	178.3750
	J=3-2	267.5575
H ¹³ CO ⁺	J=1-0	86.7543
CS	J=2-1	97.9810
	J=3-2	146.9690
	J=5-4	244.9356
C ³⁴ S	J=2-1	96.4129
	J=3-2	144.6171
CN	N(J,F)=1($\frac{1}{2}, \frac{1}{2}$) - 0($\frac{1}{2}, \frac{3}{2}$)	113.1442
	N(J,F)=1($\frac{1}{2}, \frac{3}{2}$) - 0($\frac{1}{2}, \frac{1}{2}$)	113.1705
	N(J,F)=1($\frac{1}{2}, \frac{3}{2}$) - 0($\frac{1}{2}, \frac{3}{2}$)	113.1913
	N(J,F)=1($\frac{3}{2}, \frac{3}{2}$) - 0($\frac{1}{2}, \frac{1}{2}$)	113.4881
	N(J,F)=1($\frac{3}{2}, \frac{5}{2}$) - 0($\frac{1}{2}, \frac{3}{2}$)	113.4910
	N(J,F)=1($\frac{3}{2}, \frac{1}{2}$) - 0($\frac{1}{2}, \frac{1}{2}$)	113.4996
	N(J,F)=1($\frac{3}{2}, \frac{3}{2}$) - 0($\frac{1}{2}, \frac{3}{2}$)	113.5089
	N(J,F)=2($\frac{3}{2}, \frac{5}{2}$) - 1($\frac{3}{2}, \frac{5}{2}$)	226.3600
	N(J,F)=2($\frac{3}{2}, \frac{5}{2}$) - 1($\frac{1}{2}, \frac{3}{2}$)	226.6595
	N(J,F)=2($\frac{3}{2}, \frac{1}{2}$) - 1($\frac{1}{2}, \frac{1}{2}$)	226.6337
	N(J,F)=2($\frac{5}{2}, \frac{5}{2}$) - 1($\frac{3}{2}, \frac{3}{2}$)	226.8748
	N(J,F)=1($\frac{3}{2}, 2$) - 0($\frac{1}{2}, 1$)	87.3169
CCH	N(J,F)=1($\frac{3}{2}, 1$) - 0($\frac{1}{2}, 0$)	87.3286
	N(J,F)=1($\frac{1}{2}, 1$) - 0($\frac{1}{2}, 1$)	87.4020
	N(J,F)=1($\frac{1}{2}, 0$) - 0($\frac{1}{2}, 1$)	87.4072
	N(J,F)=2($\frac{5}{2}, 3$) - 1($\frac{3}{2}, 2$)	174.6637
	N(J,F)=2($\frac{5}{2}, 2$) - 1($\frac{3}{2}, 1$)	174.6881
	N(J,F)=2($\frac{3}{2}, 2$) - 1($\frac{1}{2}, 1$)	174.7222
	N(J,F)=2($\frac{3}{2}, 1$) - 1($\frac{1}{2}, 0$)	174.7285
	N(J,F)=3($\frac{7}{2}, 4$) - 2($\frac{5}{2}, 3$)	262.0045
	N(J,F)=3($\frac{7}{2}, 3$) - 2($\frac{5}{2}, 2$)	262.0068
	N(J,F)=3($\frac{5}{2}, 3$) - 2($\frac{3}{2}, 2$)	262.0651
	N(J,F)=3($\frac{5}{2}, 2$) - 2($\frac{3}{2}, 1$)	262.0658
HCS ⁺	J=2-1	85.3479
c-C ₃ H ₂	N(J,F)=2(1,2)-1(0,1)	85.3389

al., 2004). These findings warrant detailed investigations into the chemical complexity of a representative ensemble of PDRs in order to test and improve PDR models and thus facilitate the understanding of this important part of the interstellar medium.

HCN and HCO^+ are sensitive tracers of the chemistry and the ionization fraction in photon dominated regions (Boger & Sternberg, 2005). The ion fraction has a very strong impact on the abundances of these species (and others like HOC^+).

The CN/HCN line ratio has been identified as an important indicator of the physics of dense PDRs (Boger & Sternberg, 2005; Meijerink & Spaans, 2005). High ratios are observed in PDRs near the illuminated surfaces (e.g. Fuente et al., 1993). However, different scenarios are suggested to explain the observations. New observations of higher excited lines and of more species are needed to improve on this analysis.

Chemical stratification of CN and CS sub-millimeter emission have been observed in Orion Bar (Simon et al., 1997).

C_2H abundance could probe the low density envelop interclump medium where grains are fragmented (Fuente et al., 1993; Pety et al., 2005). At present its high obscured abundance can not be reproduced by PDR models.

The high spatial resolution achieved by the 30m is essential for this project. Data will be interpreted using the KOSMA- τ model (Röllig et al., 2006).

6.3 Two observed cuts

Cepheus B exhibits PDRs which are subject to only moderately strong UV field of $\chi \approx 10^3$ in contrast to most of the classical PDRs like the Orion Bar, MonR2, M17SW which are subject to much strong UV fields. Moreover, the western PDR of Cepheus B allows to study the stratification of chemical abundances expected from PDR models. A recent detailed comparison of various PDR models (Röllig et al., 2006) showed that observations of specific tracer molecules are needed to test the models.

Two cuts through different environments of $5'$ length each have been observed in the Cepheus B cloud (see Fig. 6.1). The map coordinates in the Cepheus B cloud refer to the (0,0) center position at $\alpha = 22^h57^m07^s$, $\delta = 62^\circ37'33''$ (J2000). Both cuts run through the interfaces into the main cloud and thus allow to trace several interface regions where I expect to trace the stratified structure of the PDR as a function of the distance from the illuminating sources. To focus on the effect of the combination of density structure and radiation field, I avoid the hot core region, where the gas is affected by shocks and the interaction with the newly born IR cluster. I also pick up two interface positions for a more detailed study. Those two positions are $(60'', -185'')$ and $(20'', -50'')$, which lie on the two cuts.

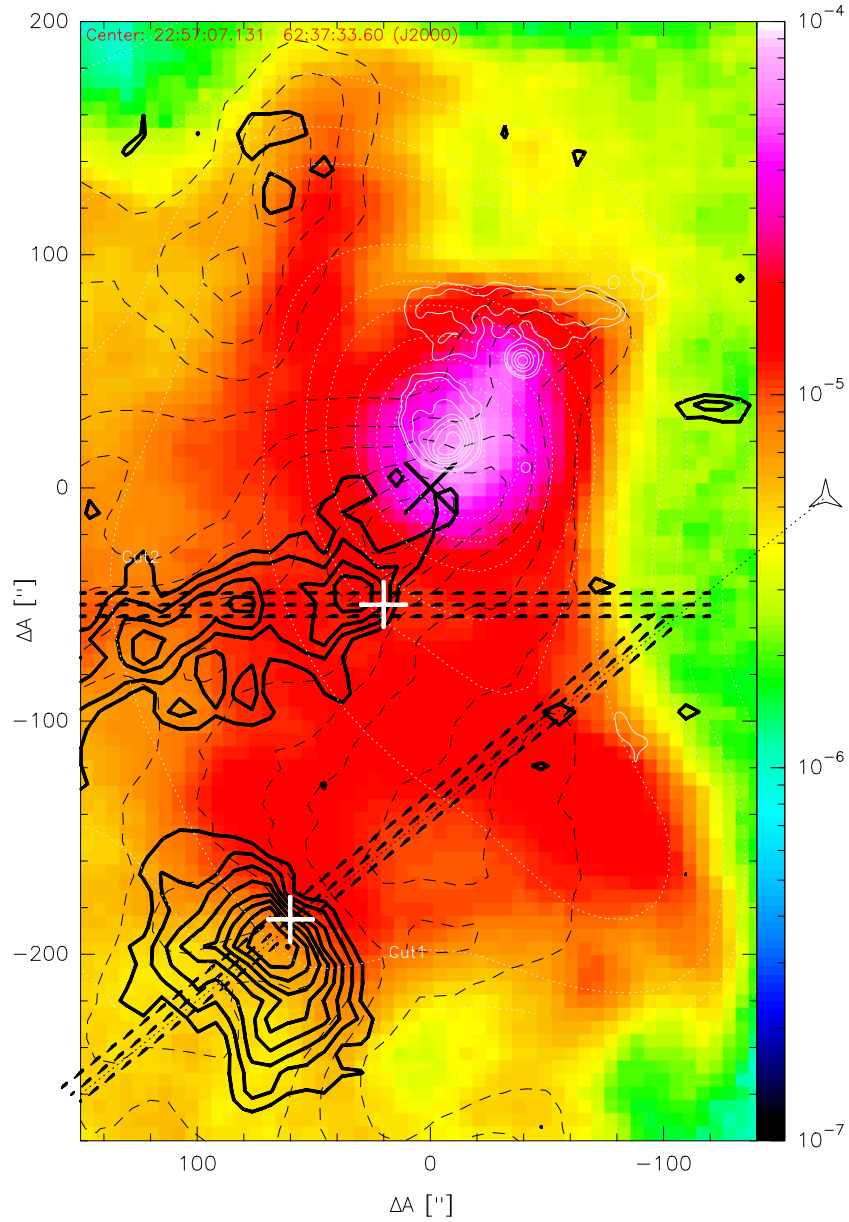


Figure 6.1: The MSX 8 micron PAH map of the Cepheus B PDRs overlaid by C^{18}O 1–0 (thick black contours), ^{12}CO 1–0 (dashed black contours), radio continuum (white contours) and FUV field (dotted white contours). The two sets of three dashed lines in a row indicate the cuts I observed; the two white crosses show the two interface positions. The B 1 star, HD 217061 is denoted as an open triangle. The center (0,0) is corresponding to $\alpha = 22^{\text{h}}57^{\text{m}}07^{\text{s}}$, $\delta = 62^{\circ}37'33''$ (J2000).

6.4 Results

6.4.1 Spectra at the two interface positions

Spectra of the observed lines at the two observed positions are shown in Fig. 6.2 - Fig. 6.4. The rest frequencies of those lines are presented in Table 6.1. All the spectra presented here are all in main beam temperature scales. The velocity range is fixed from -25 km s^{-1} to 0 km s^{-1} and the main beam temperature is fixed from -0.5 K to 3 K . All tracers have been detected at $(60'', -185'')$. The weakest line is HCS^+ 2-1, which is about 80 mK . Both C^{34}S 2-1 and 3-2 are around 200 mK . As seen from those figures, the strongest line is ^{12}CO 1-0: $\sim 45 \text{ K}$ at $(60'', -185'')$ and $\sim 41 \text{ K}$ at $(20'', -50'')$. Besides for CO and its isotopes, strong lines were observed for all these species with T_{mb} peaking near $\sim 10 \text{ K}$. Except for CO lines, the strongest emission is HCN 1-0. The ratios of CN 1-0 / HCN 1-0 and CN 2-1 / HCN 2-1 are 0.92 and 1.16, respectively. Fairly strong ($\sim 0.5 \text{ K}$) lines have been seen for the ubiquitous $\text{c-C}_3\text{H}_2$ while weak lines have been detected for HCO, HC_3N , and HCS^+ . The line intensities are also list in Table 6.2.

The observed hyperfine spectra depend on the total optical depth, the line width, the Doppler velocity of the source and the amplitude factor. All those parameters can be derived by a least square fit to the observed spectrum using the CLASS software (<http://www.iram.es/IRAMFR/GILDAS/>). The results of such least square fit for HCN, CN and C_2H at the two interface positions are shown in Fig. 6.3 and Fig. 6.4, respectively. To fit the line profile I assumed optical depth ratios between individual hyperfine components that are consistent with the relative intensities. The results of the fit are listed in Table 6.3. Due to bad signal to noise ratios for C_2H 3-2 and CN 2-1 at $(20'', -50'')$, the opacity derived there is not very reliable.

I have detected four strongest ones of six hyperfine transitions of C_2H 1-0 (Ziurys et al., 1982) and five of eleven hyperfine transitions of C_2H 2-1 (Ziurys et al., 1982) at both positions. And four of eleven hyperfine transitions of C_2H 3-2 (Ziurys et al., 1982) are detected at $(60'', -185'')$, while the C_2H 3-2 transition is very weak at $(20'', -50'')$. C_2H lines are believed to be optically thin, as suggested by their hyperfine-split intensity ratios and line-widths (Tucker et al., 1974). From the hyperfine structure fit, the obtained opacities of C_2H 1-0 at $(60'', -185'')$ and $(20'', -50'')$ are 0.65 and 0.69, respectively. And the opacities of C_2H 2-1 are around 1. So C_2H lines are not really optically thin.

The hyperfine structure upto the $J = 3-2$ transition of HCN has been well resolved at $(60'', -185'')$. While only the hyperfine structure of the $J = 1-0$ transition of HCN is resolved at $(20'', -50'')$. HCN 1-0 at both positions are optically thin, the opacities are 0.43 at $(60'', -185'')$ and 0.1 at $20'', -50''$. While the HCN 2-1 transitions are optically thick at both positions, especially at $(60'',$

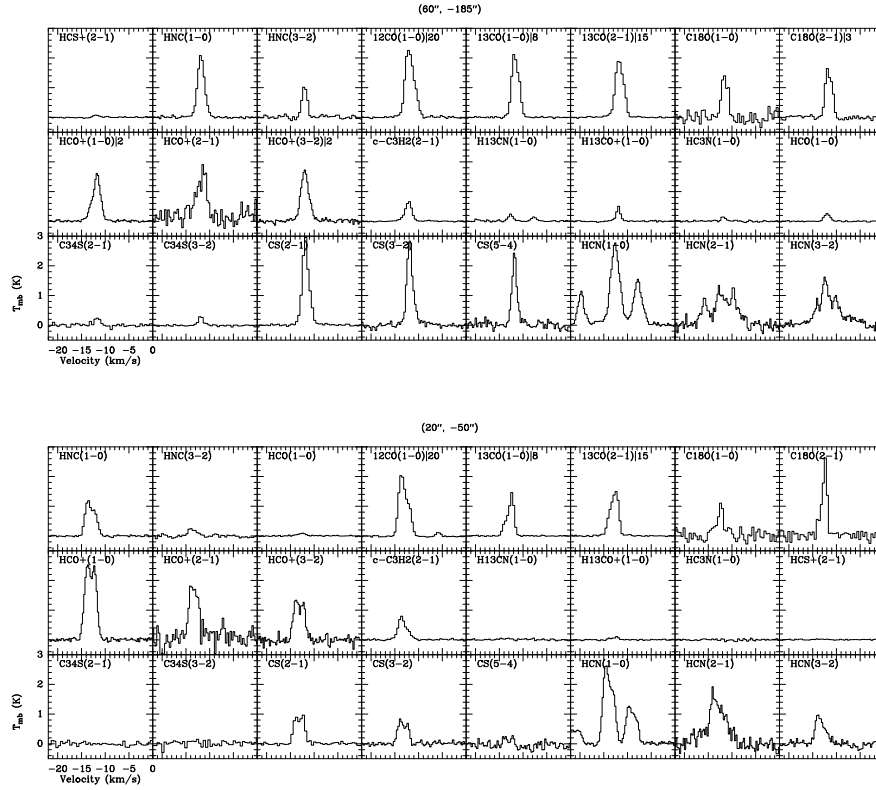


Figure 6.2: The spectra of $\text{HCS}^+ 2-1$, $\text{HNC } 1-0$, $\text{HNC } 3-2$, $^{12}\text{CO } 1-0$, $^{13}\text{CO } 1-0$, $^{13}\text{CO } 2-1$, $\text{C}^{18}\text{O } 1-0$, $\text{C}^{18}\text{O } 2-1$, $\text{HCO}^+ 1-0$, $\text{HCO}^+ 2-1$, $\text{HCO}^+ 3-2$, $c\text{-C}_3\text{H}_2 2_{1,2}-1_{0,1}$, $\text{H}^{13}\text{CN } 1-0$, $\text{H}^{13}\text{C}^+ 1-0$, $\text{HC}_3\text{N } 1-0$, $\text{HCO } 1-0$, $\text{C}^{34}\text{S } 2-1$, $\text{C}^{34}\text{S } 3-2$, $\text{CS } 2-1$, $\text{CS } 3-2$, $\text{CS } 5-4$, $\text{HCN } 1-0$, $\text{HCN } 2-1$ and $\text{HCN } 3-2$ at the two interface positions.

Table 6.2: Line Parameters on the two interface positions besides for CO and its isotopes. ND is indicates non-detection.

Molecule	Transition	(60'',-185'') I_{mb} (K km s ⁻¹)	(20'',-50'') I_{mb} K km s ⁻¹)
C ³⁴ S	2-1	0.452	0.503
C ³⁴ S	3-2	0.584	0.630
c-C ₃ H ₂	2 _{1,2} -1 _{0,1}	1.213	1.757
C ₂ H	1-0	7.140	5.048
C ₂ H	2-1	6.950	4.794
C ₂ H	3-2	6.981	1.850
CN	1-0	11.076	9.811
CN	2-0	8.045	6.249
CS	2-1	4.973	2.471
CS	3-2	4.193	2.076
CS	5-4	3.539	0.428
H ¹³ CN	1-0	0.679	0.194
H ¹³ CO ⁺	1-0	0.578	0.177
HC ₃ N	10-9	0.260	ND
HCN	1-0	12.125	11.044
HCN	2-1	6.860	6.506
HCN	3-2	6.463	2.276
HCO	1-0	0.384	0.163
HCO ⁺	1-0	6.772	7.240
HCO ⁺	2-1	8.315	7.251
HCO ⁺	3-2	7.344	3.269
HCS ⁺	2-1	0.105	0.123
HNC	1-0	3.875	2.850
HNC	1-0	1.498	0.141

Table 6.3: The results of hyperfine transition fitting for C₂H, CN and HCN.

	(60'', -185'')		(20'', -50'')	
	$T_{\text{mb}} * \tau_{\text{tot}}$	τ_{tot}	$T_{\text{mb}} * \tau_{\text{tot}}$	τ_{tot}
C ₂ H 1-0	4.252 ± 0.133	0.653 ± 0.191	2.524 ± 0.089	0.690 ± 0.221
C ₂ H 2-1	5.583 ± 0.663	1.825 ± 1.004	2.327 ± 0.161	0.100 ± 1.157
C ₂ H 3-2	3.536 ± 0.494	0.402 ± 1.060	3.507 ± 3.890	7.245 ± 8.857
CN 1-0	11.570 ± 0.517	4.581 ± 0.454	5.809 ± 0.075	0.100 ± 0.045
CN 2-1	10.215 ± 0.735	7.912 ± 1.031	3.220 ± 0.450	0.100 ± 0.707
HCN 1-0	5.295 ± 0.104	0.434 ± 0.087	4.471 ± 0.031	0.100 ± 0.007
HCN 2-1	10.919 ± 0.917	12.163 ± 1.284	4.648 ± 0.864	2.877 ± 0.763
HCN 3-2	1.259 ± 0.041	0.100 ± 0.090	1.761 ± 1.061	1.437 ± 1.762

-185'') where the opacity for HCN 2-1 is 12.16. However, the opacity of HCN 3-2 is again optically thin at (60'', -185''). Fig. 6.3 and Fig. 6.4 indicate that the LTE intensities can not reproduce the observed HCN line intensities, especially at (60'', -185''). For example, the ratios $R_{1_{-12}} = I(F = 1 - 1)/I(F = 2 - 1)$ and $R_{1_{-02}} = I(F = 0 - 1)/I(F = 2 - 1)$ for HCN J = 1-0 are 0.54 and 0.40 at (60'', -185''), respectively. And the ratios at (20'', -50'') are $R_{1_{-12}} = 0.49$ and $R_{1_{-02}} = 0.20$. The LTE ratios are $R_{1_{-12}} = 0.6$ and $R_{1_{-02}} = 0.2$ (Baudry et al., 1980). These anomalous ratios of hyperfine components can not be interpreted in terms of a single excitation temperature. Rapidly collapsing or expanding cloud models have previously been utilized to explain anomalies in the ratios $R_{1_{-12}}$ and $R_{1_{-02}}$ (Gottlieb et al., 1975; Baudry et al., 1980).

At both positions, the peak temperatures of CN 1-0 are higher than those of CN 2-1. Both observed CN transitions are optically thick (4.58 and 7.91 for CN 1-0 and 2-1, respectively) at (60'', -185''), while they are optically thin at (20'', -50''). There is no deviation from LTE for the CN lines at (60'', -185''), especially for CN 1-0. Although the intensity of N(J,F) = 2(3/2, 3/2)-1(1/2, 1/2) is higher than the LTE prediction ($\sim 20\%$) at (60'', -185''), which was also found for Orion A by Greaves & White (1992). And they attributed their finding to non-LTE effects affecting the CN 2-1 line fine structure levels. But considering the observational uncertainties, it is not confirmed in this case. For CN N 1-0 at (20'', -50''), there are some evidence of self-absorption for N(J,F) = 1(3/2, 3/2)-0(1/2, 1/2), 1(3/2, 1/2)-0(1/2, 1/2), and 1(3/2, 3/2)-0(1/2, 3/2). The self-absorption effects were also found in TMC-1 and ρ Ophiuchus by Crutcher et al. (1984); Simon et al. (1997).

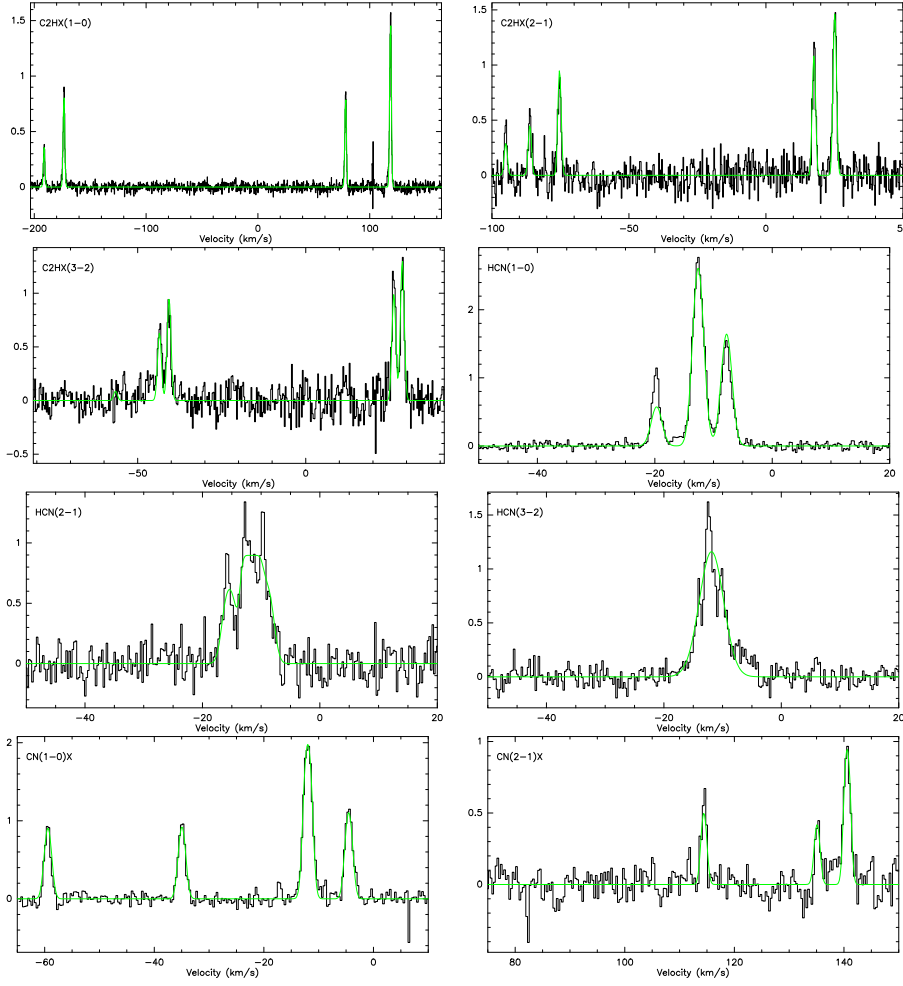


Figure 6.3: Spectra at the interface ($60''$, $-185''$). In the sequence of left to right and top to bottom, there are C₂H 1–0, 2–1, 3–2, HCN 1–0, 2–1, 3–2 and part of CN 1–0 and 2–1. The green lines are the results from the hyperfine structure fit.

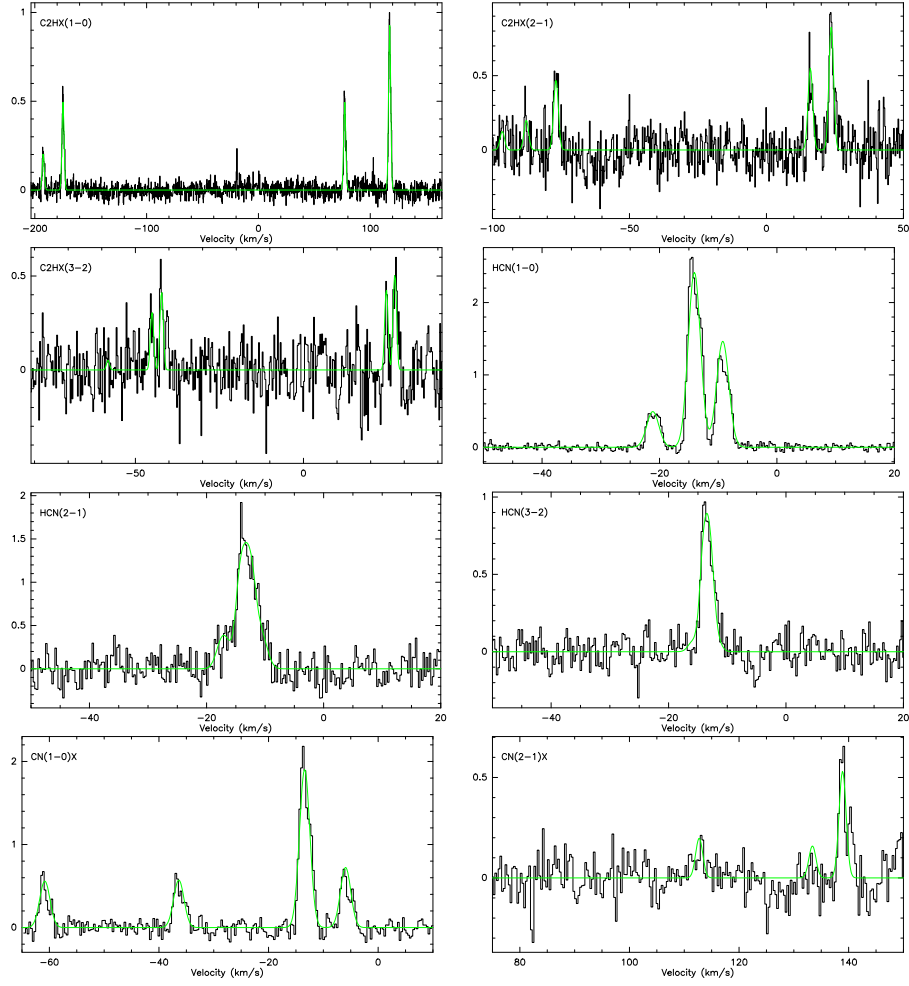


Figure 6.4: Spectra at the interface ($20''$, $-50''$). In the sequence of left to right and top to bottom, there are C_2H 1–0, 2–1, 3–2, HCN 1–0, 2–1, 3–2 and part of CN 1–0 and 2–1. The green lines are the results from the hyperfine structure fit.

6.4.2 Integrated intensities along the two cuts

Fig. 6.5 presents the distribution of integrated intensities along the two cuts. For some positions where there is no detection, I take the 3-sigma values as upper limits. For all the tracers, line intensities behave very similar: they increase from the H_{II} region to the interface position, then decrease when going into the clouds. The strongest intensity of each tracers occurs at the interfacer positions. Among all tracers, the strongest is HCN 1–0 and the second strongest tracer is CN 1–0. The ratio of CN 1–0 / HCN 1–0 is rather constant along both cuts. The CN/HCN line ratio has been identified as an important indicator of the physics of dense PDRs (Meijerink & Spaans, 2005). The weakest transitions are C₃₄S 2–1 and 3–2. They only show up at the two interface positions with an integrated intensity of ~ 300 mK km s^{–1}. For cut1, the line intensities drop fast after the interface position; while for cut2, the intensities extend into the cloud.

6.4.3 LTE analysis

In this subsection, I present the results from a LTE analysis at the two interface positions. The results include opacity and excitation temperature estimations and column density calculations.

Opacity of each tracers is calculated from the line intensity ratios between isotopomers except for HCN. The opacities of HCN is derived from the hyperfine structure fit.

To derive the excitation temperature T_{ex} , the line intensity ratios of two transitions of each molecules are used. I also assume that ¹²CO, ¹³CO and C¹⁸O have the same excitation temperature. And this assumption also applied to CS and C³⁴S, HCO⁺ and H¹³CO⁺. For those molecules observed only one transition like HCS⁺ and HCO, I assume an excitation temperature of 10 K.

I use Equation A.11 in Appendix A to calculate column densities for ¹²CO, ¹³CO, C¹⁸O, CS, C³⁴S, HCO⁺, H¹³CO⁺, HCN, HNC, HCS⁺ and HCO at the two interface positions. A optical thick correction for all the column densities (except for HNC, HCS⁺ and HCO) is the factor of $\frac{\tau}{1-\exp(-\tau)}$. The permanent dipole moment μ and the rotational constant B of each tracer used in the column density calculations are list in Table 6.4.

The details on opacity, excitation temperature and column density calculations can be found in Appendix A. All the results are listed in Table 6.5.

The line intensity ratio of ¹²CO 1–0 and ¹³CO 1–0 is used to derive the optical depth (opacity) for those two transitions, taking account of the [¹²CO]/[¹³CO] of 65 (Langer et al., 1990). Then I use the intensity ratio of ¹³CO 1–0 and C¹⁸O 1–0 and the ¹³CO 1–0 opacity to estimate the opacity of C¹⁸O 1–0. As expected, ¹²CO 1–0 transition is optically thick, while ¹³CO 1–0 and C¹⁸O 1–0 are optically thin,

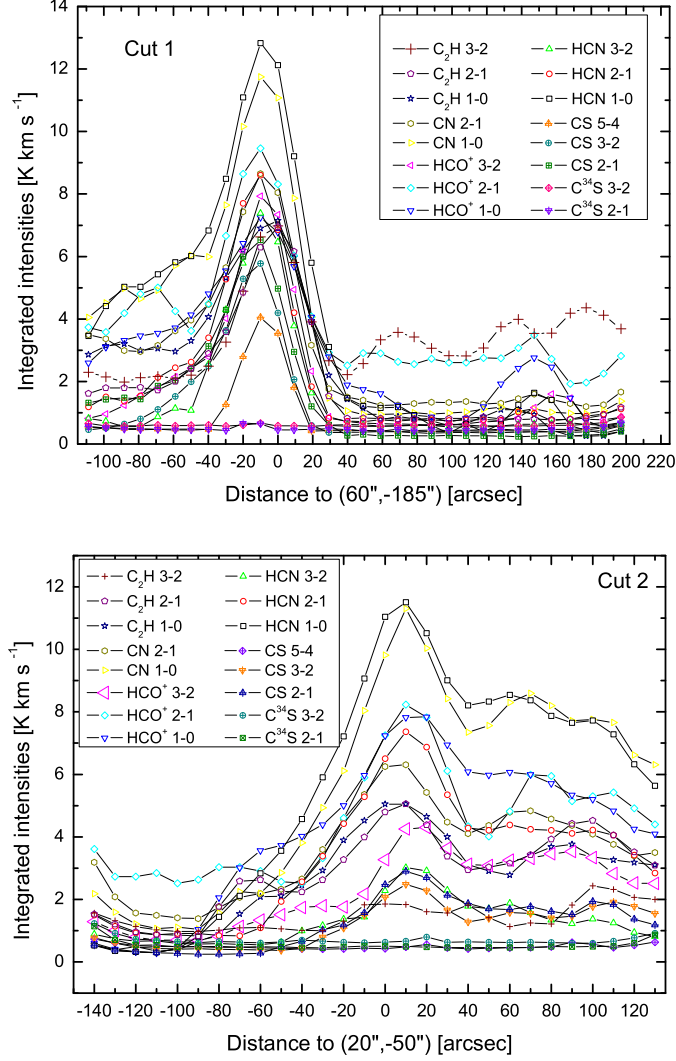


Figure 6.5: The distribution of integrated intensities along the two cuts. The x axis indicates the relative distance to those two interface positions. Negative and positive distances are assigned to the west and east of those two interface positions, respectively.

Table 6.4: Molecular constants used for column density calculations. μ is permanent dipole moment and B is rotational constant. All the data are taken from the Cologne Database for Molecular Spectroscopy (CDMS, see <http://www.astro.uni-koeln.de/vorhersagen/>)

Molecular	μ (Debye)	B (MHz)
^{12}CO	0.1101	57635.968
^{13}CO	0.1105	55101.012
C^{18}O	0.1105	54891.421
CS	1.958	24495.56
C^{34}S	1.958	24103.55
HCO^+	3.90	44594.43
H^{13}CO^+	3.90	43377.30
HCN	2.985	44315.976
HNC	3.05	45331.98

especially the latter at both interface position. Opacities are 19.77 and 11.43 for $(60'', -185'')$ and $(20'', -50'')$, respectively. The excitation temperatures derived from ^{12}CO 1–0 transition are 110 K and 95 K for $(60'', -185'')$ and $(20'', -50'')$, respectively.

The intensity ratio of CS 2–1 and C^{34}S 2–1 is used to estimate the opacities assuming a terrestrial isotope ratio of 22.5 (Lapinov et al., 1998). CS 2–1 at both positions are optically thick with an opacity of 1.65 and 4.53 for the two interface positions, respectively. The optical depth of CS 2–1 at $(60'', -185'')$ is bigger than that at $(20'', -50'')$. C^{34}S 2–1 is optically thin, especially at $(60'', -185'')$. The line intensity ratio between CS 5–4 and CS 3–2 is used to derive the excitation temperature, which is ~ 8 K at $(60'', -185'')$ and ~ 5 K at $(20'', -50'')$.

I use the intensity ratio of HCO^+ 1–0 and H^{13}CO^+ 1–0 to derive the opacities, assuming a terrestrial isotope ratio of 65 (Hogerheijde et al., 1997). The opacities of HCO^+ 1–0 are 5.53 and 1.01 for $(60'', -185'')$ and $(20'', -50'')$, respectively. And H^{13}CO^+ 1–0 is optically thin at both positions. The excitation temperature for HCO^+ is estimated using the intensity ratio of HCO^+ 3–2 and 2–1. And it is ~ 13 K at $(60'', -185'')$ and ~ 8 K at $(20'', -50'')$.

The opacity of HCN 1–0 is obtained from the hyperfine structure fit as mention above. The line intensity ratio of HCN 3–2 and 2–1 is considered to obtain the excitation temperature of HCN , which is ~ 11 K for both positions. I use the intensity ratio of HNC 2–1 and 1–0 to derive the excitation temperature of HNC , which is ~ 7 K for both interface positions.

I use ^{12}CO 1–0, ^{13}CO 1–0, C^{18}O 1–0, CS 2–1, C^{34}S 2–1, HCO^+ 1–0, H^{13}CO^+ 1–0, HCN 1–0, HNC 1–0, HCS^+ 2–1 and HCO 1–0 to calculate the corresponding

Table 6.5: LTE analysis for CO, CS, HCO^+ , HCN, HNC, HCS^+ and HCO at the two interface positions. The opacities of ^{12}CO 1–0, ^{13}CO 1–0, C^{18}O 1–0, CS 2–1, C^{34}S 2–1, HCO^+ 1–0, H^{13}CO^+ 1–0, HCN 1–0, HNC 1–0, HCS^+ 2–1 and HCO 1–0 are listed at the top. The excitation temperatures of CO, CS, HCO^+ , HCN, HNC, HCS^+ and HCO are listed in the middle. The column densities of H_2 , ^{12}CO , ^{13}CO , C^{18}O , CS, C^{34}S , HCO^+ , H^{13}CO^+ , HCN, HNC, HCS^+ and HCO are listed at the bottom.

	(60'', -185'')	(20'', -50'')
$\tau_{^{12}\text{CO}1-0}$	19.77	11.43
$\tau_{^{13}\text{CO}1-0}$	0.30	0.18
$\tau_{\text{C}^{18}\text{O}1-0}$	0.02	0.01
$\tau_{\text{CS}2-1}$	1.65	4.53
$\tau_{\text{C}^{34}\text{S}2-1}$	0.07	0.20
τ_{HCO^+1-0}	5.53	1.01
$\tau_{\text{H}^{13}\text{CO}^+1-0}$	0.09	0.02
$\tau_{\text{HCN}1-0}$	0.43	0.10
$T_{\text{ex}}^{\text{CO}}$ (K)	111.00	95.46
$T_{\text{ex}}^{\text{CS}}$ (K)	8.01	5.44
$T_{\text{ex}}^{\text{HCO}^+}$ (K)	13.26	8.20
$T_{\text{ex}}^{\text{HCN}}$ (K)	10.97	10.59
$T_{\text{ex}}^{\text{HNC}}$ (K)	6.93	5.87
$N(\text{H}_2)^b$ (cm^{-2})	7.64×10^{22}	2.75×10^{22}
$N(^{12}\text{CO})$ (cm^{-2})	1.08×10^{19}	4.66×10^{18}
$N(^{13}\text{CO})$ (cm^{-2})	2.09×10^{17}	8.45×10^{16}
$N(\text{C}^{18}\text{O})$ (cm^{-2})	1.30×10^{16}	4.68×10^{15}
$N(\text{CS})$ (cm^{-2})	2.40×10^{13}	2.13×10^{13}
$N(\text{C}^{34}\text{S})$ (cm^{-2})	1.05×10^{12}	9.91×10^{11}
$N(\text{HCO}^+)$ (cm^{-2})	2.19×10^{13}	4.27×10^{12}
$N(\text{H}^{13}\text{CO}^+)$ (cm^{-2})	3.30×10^{11}	6.22×10^{10}
$N(\text{HCN})$ (cm^{-2})	1.22×10^{13}	9.20×10^{12}
$N(\text{HNC})$ (cm^{-2})	2.10×10^{12}	1.33×10^{12}

^a excitation temperatures are assumed to be 10 K; ^b H_2 column density is calculated from the C^{18}O column density using the canonical abundance ratios of $[^{12}\text{CO}]/[\text{C}^{18}\text{O}]$ of 470 (Langer et al., 1990) and $[\text{CO}]/[\text{H}_2]$ of 8×10^{-5} (Frerking et al., 1982).

Table 6.6: Results of the relative column densities to H_2 column density at two interface positions. $X(Y)$ is the fractional abundance of tracer Y relative to H_2 : $N(Y)/N(\text{H}_2)$.

	(60'', -185'')	(20'', -50'')
$X(^{12}\text{CO})$	1.41×10^{-4}	1.69×10^{-4}
$X(^{13}\text{CO})$	2.74×10^{-6}	3.07×10^{-6}
$X(\text{C}^{18}\text{O})$	1.70×10^{-7}	1.70×10^{-7}
$X(\text{CS})$	3.14×10^{-10}	7.75×10^{-10}
$X(\text{C}^{34}\text{S})$	1.37×10^{-11}	3.60×10^{-11}
$X(\text{HCO}^+)$	2.87×10^{-10}	1.55×10^{-10}
$X(\text{H}^{13}\text{CO}^+)$	4.32×10^{-12}	2.26×10^{-12}
$X(\text{HCN})$	1.60×10^{-10}	3.35×10^{-10}
$X(\text{HNC})$	2.75×10^{-11}	4.84×10^{-11}

column densities of each molecule. I also estimate the H_2 from the C^{18}O column density using the canonical abundance ratios of $[^{12}\text{CO}]/[\text{C}^{18}\text{O}]$ of 470 (Langer et al., 1990) and $[\text{CO}]/[\text{H}_2]$ of 8×10^{-5} (Frerking et al., 1982). The H_2 column densities I obtain are 7.64×10^{22} at (60'', -185'') and 2.75×10^{22} at (20'', -50''), which are at the same order of the H_2 column densities in Cepheus B calculated by Beuther et al. (2000).

The column densities of $N(\text{CS})$, $N(\text{C}^{34}\text{S})$, $N(\text{HCO}^+)$, $N(\text{H}^{13}\text{CO}^+)$, $N(\text{HCN})$ (cm^{-2}), $N(\text{HNC})$ (cm^{-2}) are very similar with those found in N 159W, but bigger than those in N 159S, N 160, 30 Dor-10, 30 Dor-27, N 27 in Magellanic clouds (Heikkilä et al., 1999).

I also calculate the fractional abundance of each molecules relative to H_2 column density (see Table 6.6). I find the $X(\text{HCO}^+) \sim 10^{-10}$, which is smaller to previous studies (Hogerheijde et al., 1997). Hogerheijde et al. (1997) found $X(\text{HCO}^+)$ of 1.2×10^{-8} in L 1489 IRS, T Tau, Haro 6-10, L 1551 IRS 5, L 1535 IRS, TMR 1, TMC 1A, L 1527 IRS and TMC 1.

6.5 Summary and outlook

I have presented the first results of a multi-line study in the Cepheus B molecular clouds. I have recorded two 5' long cuts for up to three transitions of the CS, HCO^+ , HCN, HNC, CN, and C_2H molecules. Strong lines were observed for all these species with T_{mb} peaking ~ 10 K range. I calculate the integrated intensity distribution along the cuts. I use a least square fit to the observed hyperfine structure of C_2H , CN and HCN to derive the opacities.

At the two interface positions, column densities of H_2 , ^{12}CO , ^{13}CO , C^{18}O ,

CS, $C^{34}S$, HCO^+ , $H^{13}CO^+$, HCN, HNC, HCS^+ and HCO are estimated under the LTE assumption. The fractional abundance of each molecules relative to H_2 column density is also calculated.

The study in Cepheus B cloud has not been finished yet. The column densities of C_2H and CN are needed to be estimated. A more detailed comparison with literature is also needed. And follow-up study will be a radiative transfer analysis using large velocity gradient codes and a detailed PDR model analysis.

Chapter 7

Summary and future prospects

7.1 Summary of results

This thesis work is on the structure of the interstellar medium. I have studied two topics: a.) use large scale surveys of Galactic molecular clouds (the Perseus molecular cloud) to study their structural properties; b.) study the physical properties of the transition layers on the surface of molecular clouds as traced by emission from [C II], [C I], and CO, which reflects the structure of molecular clouds. The aim is to understand the energy balance of photon dominated regions, photo-induced chemistry, and PDR dynamics and kinematics.

To study large scale structural properties, I mapped the nearby low-mass star-forming regions Perseus in ^{12}CO 3–2 and ^{13}CO 2–1 with the KOSMA 3m telescope. The Δ - variance method was used to study the spatial structure of line-integrated and velocity channel maps in Perseus. I estimated the spectral index β of the corresponding power spectrum and studied its variation across the cloud and across the lines. I found that the overall mapped region follows a power law with an index of $\beta = 2.9 - 3.0$ for scales between 0.2 and 3 pc. This agrees with the results obtained by Padoan et al. (2003b) who studied structure functions of a ^{13}CO 1–0 map of Perseus. While for the individual sub-regions, the resulting power spectral indices vary significantly: the active star-forming region NGC 1333 shows high spectral indices ($\beta = 3.5 - 3.8$), while the dark cloud L 1455 shows low indices of 2.9. Then I applied the same method to individual velocity channel maps. I found an asymmetry of the power law indices of the channel maps relative to the line centrum, which is a hint towards a peculiar velocity structure of the Perseus cloud complex. The indices with increasing velocity width are almost constant. A continuous increase of the index with varying velocity channel width is observed in the blue wings, which can be explained by a shock running through the region creating a filamentary structure preferentially at low velocities. And it

is coincident with an expanding shell of neutral hydrogen which was created by a supernova in the Per OB2 association a few 10^6 years ago (Sancisi, 1974).

GAUSSCLUMPS is used to identify clumps for the whole observed Perseus cloud and seven sub-regions as the same as in the Δ - variance method analysis, and to derive the clump properties as traced in ^{13}CO 1–0 and 2–1. Using the KOSMA ^{13}CO 2–1 data, there are 341 clumps found, the mass range of which is between $0.54 M_{\odot}$ and $87.98 M_{\odot}$. And I find 737 clumps using the FCRAO ^{13}CO 1–0 data and the clump mass ranges from $0.28 M_{\odot}$ and $140.90 M_{\odot}$. A power law index ~ 1.9 of clump mass spectra is found. Studies of the relations of clump sizes with line widths and clump masses confirm the standard Larson relations. The virial parameter, which is the ratio between virial mass and the mass estimated from the Local Thermodynamic Equilibrium analysis, is used to characterize the equilibrium state of a clump. All clumps identified in both NGC 1333 and L 1455 are found with a virial parameter above 1. The external pressures needed to bind the clumps fall within 10^3 K cm^{-3} and 10^6 K cm^{-3} for the whole observed Perseus cloud.

I applied the KOSMA - τ photon dominated region model at seven selected positions in IC 348 by examining the three independent line ratios to derive the local physical condition. The clump density in those seven positions falls between $4.4 \cdot 10^4 \text{ cm}^{-3}$ and $4.3 \cdot 10^5 \text{ cm}^{-3}$. The FUV field fitted from the model is consistent with independent estimates for the FUV field derived from the FIR continuum maps by IRAS and from the stellar radiation. Then I expanded the analysis to a clumpy PDR scenario with a distribution of clumps over a range of masses and sizes. This clumpy PDR model produces model line intensities which are in good agreement within a factor of ~ 2 with the observed intensities. I also predicted the line intensities for $[\text{C I}] \ ^3\text{P}_2 - ^3\text{P}_1$, ^{12}CO 7–6, ^{13}CO 8–7 which can be confirmed by future observations. Finally, I confirmed the anti-correlation between C/CO abundance ratio and hydrogen column density. This anti-correlation has been found in many regions and has been explained by Mookerjee et al. (2006).

To understand photo-induced chemistry of the photon dominated regions, I carried out a multi-line study of two cuts in the nearby star forming region Cepheus B using the IRAM 30m telescope at Pico Veleta. Cepheus B is particularly well suited as a PDR candidate because it is relatively close (730 pc) and fairly extended (more than $5' \times 5'$) thus permitting the PDR to be resolved spatially. To the north-west lie the HII region S 155 and the Cepheus OB3 association. Based on the FIR continuum, the FUV radiation field varies between $1500 G_0$ at the interface and $\sim 25 G_0$ in the inner core (Mookerjee et al., 2006). Thus, Cepheus B represents a class of PDRs with moderately strong UV field. I have recorded two $5'$ long cuts for up to three transitions of the CS, HCO^+ , HCN, HNC, CN, and C_2H molecules. Strong lines were observed for all these species with T_A^* peaking in the 1 – 3 K range. Other species were searched for in two positions at the in-

interfaces. Fairly strong (~ 0.5 K) lines were seen for the ubiquitous $c\text{-C}_3\text{H}_2$ while weak lines were detected for HCO, HC_3N , and HCS^+ along with some isotopic species of the molecules seen very strongly. Data at the two cuts were combined with low - J ^{12}CO , ^{13}CO , and C^{18}O IRAM-30m maps of Cepheus B (Ungerechts et al., 2000). In the first step, I estimated the relative abundance of each molecule along the cuts assuming Local Thermodynamic Equilibrium (LTE). The follow-up study will be a detailed PDR model analysis.

7.2 Future prospects

More follow-up studies are needed on the velocity channel analysis using CO data. As CO is an optical thick and cold tracer (compared with HI clouds), the velocity channel analysis (VCA) in CO data provides complementary information on the VCA theory (Lazarian & Pogosyan, 2000), which only deals with optical thin tracers and the line center.

Another study is to determine the cross correlation between different tracers and different regions (as different sub-regions in the Perseus molecular cloud). Such studies will provide the comparison between star formation regions and quiescent dark clouds, and also the structure between different tracers.

Future observations will be useful to test the results and assess the importance of different parameters used in the clumpy PDR models. The tracers such as ^{12}CO 7–6, ^{13}CO 8–7 and $[\text{C I}]$ $^3\text{P}_2 - ^3\text{P}_1$ are essential to constrain the models. This needs further NANTEN 2 telescope observations. SOFIA and Herschel will provide observations in the Terahertz regime of the electromagnetic spectrum such as the $[\text{C II}]$ fine structure transitions. The $[\text{C II}]$ emission is important to study the physical properties of the transition layers on the surface of molecular clouds. Velocity-resolved observations of this transition are important to distinguish its emission from that emerging from the ambient WIM.

There are more studies which can be carried out in the Cepheus B molecular cloud. Cepheus B exhibits PDRs which are subject to only moderately strong UV field of $\sim 10^3 G_0$ in contrast to most of the classical PDRs like the Orion Bar, MonR2, M17SW which are subject to much strong UV fields. Moreover, the western PDR of Cepheus B is seen almost edge-on, thus allowing to study the stratification of chemical abundances expected from PDR models. So study the PDRs in Cepheus B can be a complementary sample to the Herschel Guaranteed Time Key Project, the warm and dense ISM. Furthermore, some tracers observed in the Cepheus B cloud like C_2H , could probe the low density envelop-interclump medium where grains are fragmented. At present its high obscured abundance can not be reproduced by PDR models. So further studies on Cepheus B can test current PDR models and may also provide information to implement

them.

The thesis presents the comparison of the structural properties for entire surveys and sub-sets of the Perseus molecular cloud, as well as the velocity channel analysis, provide additional, significant characteristics of the ISM in observed CO spectral line maps. These quantities are useful for a comparison of the structure observed in different clouds, possibly providing a diagnostic tool to characterize the star-formation activity and providing additional constraints for numerical simulations of the ISM structure. The thesis also studies different PDRs subject to low and intermediate FUV fields using the clumpy KOSMA - τ PDR model. Future observations will be useful to constrain the models and to judge the importance of different input parameters used. A better knowledge of these conditions in IC 348 and Cepheus B will provide a template for future studies of Galactic PDRs and the ISM in external galaxies.

Appendix A

Local thermodynamic equilibrium analysis

I have used the local thermodynamic equilibrium (LTE) analysis in Chapter 4, Chapter 5, and Chapter 6. To present more details in LTE, I will here present the basic analysis of opacity, excitation temperature, column densities and masses under the local thermodynamic equilibrium assumption.

A.1 Opacity

If one considers the coupling of the telescope beam to the source via coupling efficiency η_c , the detection equation is written as

$$T_R^* = \eta_c [J_\nu(T_{\text{ex}}) - J_\nu(T_{\text{bg}})] [1 - \exp(-\tau)], \quad \text{with } J_\nu(T) = \frac{h\nu}{k} \frac{1}{\exp(h\nu/kT) - 1} \quad (\text{A.1})$$

where $J_\nu(T)$ is the normalized Plank intensity, T_{ex} is the excitation temperature, k is the Boltzmann constant, T_{bg} is the 2.74 K black body radiation of the Cosmic back ground, τ is the opacity and T_R^* is the antenna temperature.

Under the LTE assumption, the opacity τ of a tracer X can be obtained when comparing the line intensity ratio of X and its isotopomer Y. It can be written as

$$\frac{T_R^*(X)}{T_R^*(Y)} \approx \frac{1 - \exp(-\tau_X)}{1 - \exp(-\tau_Y)} = \frac{1 - \exp(-\tau_X)}{1 - \exp(-\tau_X/I_{\text{fac}})}, \quad (\text{A.2})$$

where τ_X and τ_Y are the opacity for X and Y, and I_{fac} is the isotopic abundance ratio of [X/Y]. In the above equation, the assumption is that both X and Y are characterized by the same excitation temperature.

A.2 Excitation temperature

The excitation temperature T_{ex} for tracer X can be derived using the intensity ratio R_c of different transitions of tracer X with frequencies of ν_1 and ν_2 .

$$R_c = \frac{[J_{\nu_1}(T_{\text{ex}}) - J_{\nu_1}(T_{\text{bg}})][1 - \exp(-\tau_1)]}{[J_{\nu_2}(T_{\text{ex}}) - J_{\nu_2}(T_{\text{bg}})][1 - \exp(-\tau_2)]} \approx \frac{J_{\nu_1}(T_{\text{ex}}) - J_{\nu_1}(T_{\text{bg}})}{J_{\nu_2}(T_{\text{ex}}) - J_{\nu_2}(T_{\text{bg}})}, \quad (\text{A.3})$$

where τ_1 and τ_2 are the opacity of the transitions corresponding to ν_1 and ν_2 . There is an assumption that both transitions are optically thick.

If both transitions are optically thin, then the Equation A.3 can be written as

$$R_c \approx \frac{[J_{\nu_1}(T_{\text{ex}}) - J_{\nu_1}(T_{\text{bg}})]\tau_1}{[J_{\nu_2}(T_{\text{ex}}) - J_{\nu_2}(T_{\text{bg}})]\tau_2}, \quad (\text{A.4})$$

If there is only one transition with frequency ν measured for tracer X, then the excitation temperature can be estimated from the peak brightness temperature T_{mb} assuming this transition is optically thick and the beam filling factor f of 1. The equation is written as

$$T_{\text{mb}} = f[J_{\nu}(T_{\text{ex}}) - J_{\nu}(T_{\text{bg}})][1 - \exp(-\tau)] \approx J_{\nu}(T_{\text{ex}}) - J_{\nu}(T_{\text{bg}}). \quad (\text{A.5})$$

If this transition is optically thin, then the Equation A.5 can be expressed as

$$T_{\text{mb}} \approx [J_{\nu}(T_{\text{ex}}) - J_{\nu}(T_{\text{bg}})]\tau. \quad (\text{A.6})$$

In Chapter 5, I used Equation A.3 to derive CO excitation temperatures. In Chapter 6, I used both Equation A.3 and A.4 depending on the opacity of the tracers, and I also used Equation A.5 when there is no one transition observed.

A.3 Column density

For a molecule Y in LTE, the line opacity τ_{ν} , and excitation temperature T_{ex} , the column density of tracer Y, can be estimated using the expression for column density in a single rotational level (Scoville et al., 1986):

$$N_J(Y) = \frac{8\pi\nu^3}{c^3 A_{J+1,J}} \frac{g_J}{g_{J+1}} [1 - \exp(-\frac{h\nu}{kT_{\text{ex}}})] \int \tau_{\nu} d\nu, \quad (\text{A.7})$$

where N_J is the total column density of the lower level, c is the velocity of light, h is the Planck constant, J is the rotational quantum number of the lower state, $g_J (= 2J + 1)$, $g_{J+1} (= 2J + 3)$ are the statistical weights of the lower and upper rotational

levels and $A_{J+1,J}$ is the Einstein coefficient for spontaneous transitions from upper levels to the lower level, and v is the velocity (noting that $dv/v = dv/v$).

The Einstein coefficient for a spontaneous electric dipole transition is

$$A_{J+1,J} = \frac{64\pi^4\nu^3}{3hc^3} \mu^2 \frac{J+1}{g_{J+1}}, \quad (\text{A.8})$$

where μ is the permanent dipole moment of the molecule. The column density N_J is related to the total column density N_{tot} summed over all levels (Garden et al., 1991)

$$N_J(Y) = \frac{g_J}{Q(T_{\text{ex}})} N_{\text{tot}} \exp\left[-\frac{hBJ(J+1)}{kT_{\text{ex}}}\right], \quad (\text{A.9})$$

where B is the rotational constant of the molecular and $Q(T_{\text{ex}})$ is the partition function, which can be expressed as

$$Q(T_{\text{ex}}) = \sum_{J=0}^{\infty} g_J \exp\left[-\frac{hBJ(J+1)}{kT_{\text{ex}}}\right] \approx \frac{k(T_{\text{ex}} + hB)}{3hkB}, \quad (\text{A.10})$$

,

Finally, the total column density N_{tot} can be written as (Scoville et al., 1986; Garden et al., 1991)

$$N_{\text{tot}}(Y) = \frac{3k}{8\pi^3 B \mu^2} \frac{e^{hBJ(J+1)/kT_{\text{ex}}}}{J+1} \frac{T_{\text{ex}} + hB/3k}{1 - e^{-h\nu/kT_{\text{ex}}}} \int \tau dv, \quad (\text{A.11})$$

A.4 Mass

Then the total mass of gas in the source is given by (Scoville et al., 1986)

$$M = N_{\text{tot}}(Y) \left[\frac{H_2}{Y}\right] \mu_G m_{H_2} \frac{\pi \theta^2}{4} d^2, \quad (\text{A.12})$$

where $[\frac{H_2}{Y}]$ is the H_2 to Y abundance ratio, μ_G is the mean atomic weight of the gas, m_{H_2} is the mass of a H_2 molecule, θ is the angular diameter of the source and d is the distance of the source.

Appendix B

A new atmospheric calibration method

B.1 Introduction

Astronomical instruments have been developed rapidly (KOSMA, NANTEN 2, SOFIA and etc.). Stratospheric Observatory for Infrared Astronomy (SOFIA) is one of them. SOFIA is an airborne observatory that will study the universe in the infrared spectrum, which will fly at around 13 km high. At such high altitude, the air contains only about 20% of the molecules present at sea level. All those current/new observatories demand a new and more precise atmospheric calibration routine.

Different to the traditional calibration approach that determines the atmospheric transmission as an average over a representative section of each receiver band individually, this new atmospheric calibration scheme uses a single, free parameter, the precipitable water vapor (pwv) which is fitted to the observed atmospheric emission spectrum derived from HOT/COLD/SKY-measurements in the standard calibration cycle.

Currently there are two programs to convert raw fits data into CLASS data, one is called *Offlinecal* and the other is *Kalibrate*. In other word, those two programs will transform backend counts (raw fits data) to antenna temperatures (CLASS data). In *Offlinecal*, the traditional (Hiyama calibration) atmospheric calibration routines are used, and In *Kalibrate*, the new atmospheric calibration routines are used. Here I compared both *Kalibrate* and *Offlinecal* to test the two different atmospheric calibration methods on both simulation and real observed data. *Note that all the tests here are based on the observational data from the NANTEN 2 telescope in 2006 and the simulation data that are based on the similar setting as the NANTEN 2 observatory.*

Here are the terms that will be used later.

C	counts; a subscript indicates for ZERO, COLD, HOT, SKY or OFF
T	temperature; a subscript indicates for COLD, HOT, AMBIENT or SKY
$\eta_{\text{fe,mb}}$	forward efficiency or main beam efficiency
T_{cal}	calibration factor
f_{amb}	fraction of ambient material in main beam
$G_{\text{s,i}}$	receiver gain in the signal and image sideband $G_s + G_i = 1 \Rightarrow G_s = \frac{1}{1 + G_i/G_s}$
$x_{\text{s,i}}$	response in signal (image) band to sky port
$b_{\text{s,i}}, c_{\text{s,i}}$	b and c coefficients from the atm lookup table
pwv	water vapor
τ_v	opacity, $\tau_v = b_{\text{s,i}} * pwv + c_{\text{s,i}}$
$t_{\text{as,i,v}}$	atmospheric transmission, $t_{\text{as,i,v}} = \exp(-\tau_v)$
A	airmass, $A = 1 / \sin(\text{elevation})$

A term with a variable A with \bar{A} indicates a channel averaged value; a term with a subscript i indicates a value for a single channel.

B.1.1 Atmospheric model

In our calibration, Atmospheric Transmission at Microwaves (ATM) model (Pardo et al., 2001, 2005) is used.

The ATM model is based on recent broadband measurements and calculations. Its primary goal is to simulate the atmospheric spectrum in the millimeter and sub-millimeter regions of the electromagnetic spectrum under a wide range of conditions and geometries. The model is fully applicable from 0 to 2 THz while including lines up to 10 THz (Pardo et al., 2001). for high and dry mountain sites by means of ground-based Fourier Transform Spectroscopy measurements.

Line-by-line calculations of the absorption are performed using a line data base generated from the latest available spectroscopic constants for all relevant atmospheric species. The line widths have been obtained from published laboratory data. The excess of absorption in the long-wave range that cannot be explained by the resonant spectrum is modelled by introducing two different (dry and wet) continuum-like terms that have been precisely quantified by our measurement and that are theoretically explainable. Phase delays near H_2O , O_2 and O_3 resonances up to 10 THz are also described in the model since they affect the interferometric phase. The frequency-dependent (resonant) phase delay function is formally related to the absorption line shape via the Kramers-Kronig dispersion theory, and this relation has been used for modelling them (Pardo et al., 2001).

Especial effects involving polarization, such as the Zeeman Effect, reflection on the oceanic surface, or scattering by aerosols or hydrometeors (rain, ice, snow...), can also be simulated (Pardo et al., 2001).

B.2 The previous calibration (Hiyama's)

The previous calibration method used in the KOSMA and NANTEN 2 is called Hiyama calibration. It was developed by Hiyama (1998) as a diploma thesis in Universität zu Köln. Hiyama calibration works as the following:

- For each connected backend, *Offlinecal* reads the ZERO, COLD, HOT and SKY (or OFF) counts from the raw fits data ; then it does the average over the whole channels after zero subtraction;
- Hiyama's calibration calculates a mean atmospheric transmission by

$$\bar{t}_a = (\bar{C}_{\text{hot}} - \bar{C}_{\text{sky}}^{\text{mean}}) / (\bar{\gamma} * A_{\text{eff}} * (1 - f_{\text{amb}}) * T_{\text{hot,eff}}) - (1 - A_{\text{eff}}) / A_{\text{eff}}, \quad (\text{B.1})$$

where $\bar{\gamma}$ is defined as

$$\bar{\gamma} = \frac{\bar{C}_{\text{hot}} - \bar{C}_{\text{cold}}}{T_{\text{hot}} - T_{\text{cold}}}; \quad (\text{B.2})$$

$T_{\text{hot,eff}}$ is the effective HOT load temperature, which is defined as

$$T_{\text{hot,eff}} = \frac{T_{\text{hot}} - f_{\text{amb}} * T_{\text{amb}}}{1 - f_{\text{amb}}}; \quad (\text{B.3})$$

A_{eff} is defined as

$$A_{\text{eff}} = \frac{T_{\text{sky}}}{T_{\text{hot,eff}}}. \quad (\text{B.4})$$

- Then it does an iteration (maximum 300 times) on the α function to derive the water vapor with an initial value of 1 for α . The α function is defined as following:

$$\alpha = \frac{1 + \frac{G_i x_i}{G_s x_s}}{1 + \frac{\bar{t}_{a_i}}{\bar{t}_{a_s}} \frac{G_i x_i}{G_s x_s}} \quad (\text{B.5})$$

where \bar{t}_{a_s} and \bar{t}_{a_i} are

$$\bar{t}_a = \exp(-A * (b_i * pwv + c_i)) \quad (\text{B.6})$$

and water vapor pwv is defined

$$pwv = \frac{-\frac{1}{A} \ln \bar{t}_{a_s} - c_s}{b_s} \quad (\text{B.7})$$

- Then it calculates a constant calibration factor for each connected backend, which is computed as

$$\mathbf{T}_{\text{cal}} = (\mathbf{1} + \mathbf{Z}) * \frac{\mathbf{T}_{\text{hot}} - \mathbf{T}_{\text{cold}}}{\eta * \mathbf{t}_{\text{a,s}}}; \quad (\text{B.8})$$

to convert to T_{A}^* scales, η is the forward efficiency; to convert to main beam scales, η is the beam efficiency. Z is defined as $\frac{G_i x_i}{G_s x_s}$.

- At the end this constant T_{cal} is applied to each spectral channel to convert the counts to Kelvin scales.
- For common calibration, *Offlinecal* will carry it out after single calibration. Then it weights the individual water vapor from each connected backend by system temperature to calculate a common water vapor. At last it applies this common water vapor for calculating T_{cal} of each connected backend.

B.3 The new calibration scheme

The new atmospheric calibration is carried out as following:

- the new calibration fits all the input channels simultaneously by using the formulae below:

$$f(pwv) = T_{\text{A,sky}} - T_{\text{A,hot}} = (1 - f_{\text{ramb}}) \quad (\text{B.9})$$

$$[(1 - t_{\text{as}})G_s x_s + (1 - t_{\text{ai}})G_i x_i] \quad (\text{B.10})$$

$$T_{\text{sky}} + f_{\text{amb}}(G_s x_s + G_i x_i)T_{\text{hot}} \quad (\text{B.11})$$

$$-(G_s x_s + G_i x_i)T_{\text{hot}}$$

$$= -\frac{A_{\text{eff}}}{\alpha} T_{\text{hot}} (1 - f_{\text{amb}}) (G_s x_s + G_i x_i) \quad (\text{B.12})$$

$$\left(t_{\text{as}} + \alpha \frac{1 - A_{\text{eff}}}{A_{\text{eff}}} \right) \quad (\text{B.13})$$

$$= -\frac{A_{\text{eff}}}{\alpha} T_{\text{hot}} (\mathbf{1} - \mathbf{f}_{\text{amb}}) \mathbf{G}_s \mathbf{x}_s \quad (\text{B.14})$$

$$\left(\mathbf{1} + \frac{\mathbf{G}_i \mathbf{x}_i}{\mathbf{G}_s \mathbf{x}_s} \right) \left(t_{\text{as}} + \alpha \frac{1 - A_{\text{eff}}}{A_{\text{eff}}} \right) \quad (\text{B.15})$$

$$f(pwv) = T_{\text{A,sky}} - T_{\text{A,hot}} = \frac{1}{\gamma} (\mathbf{C}_{\text{sky}} - \mathbf{C}_{\text{hot}}) (\mathbf{G}_s \mathbf{x}_s + \mathbf{G}_i \mathbf{x}_i) \quad (\text{B.16})$$

with

$$t_{a,s,i} = \exp(-A[b(v_{s,i})pwv + c(v_{s,i})]) \quad (\text{B.17})$$

By using the $f(pwv)$ formulae in the equation (10) and (11) and weighted by receiver temperatures, one can fit the water vapor value.

- Then it uses the same calibration factor formula as the Hiyama calibration but calculates the calibration factor for each channel (each frequency), $T_{cal,v}$; then for each channel, it converts the counts to Kelvin scales by applying the corresponding $T_{cal,v}$.
- The new calibration supports both single and common calibration modes and treat both modes same. For a single calibration, the input channels are from each connected receiver band separately; for a common, the input channels are from all the connected receiver bands simultaneously.

Below is the **Flow chart of CALIBRATIONFACTOR.f** which is the main calibration routine and sends back an array of $T_{cal,v}$ to *Kalibrate*.

B.4 Testing the new calibration

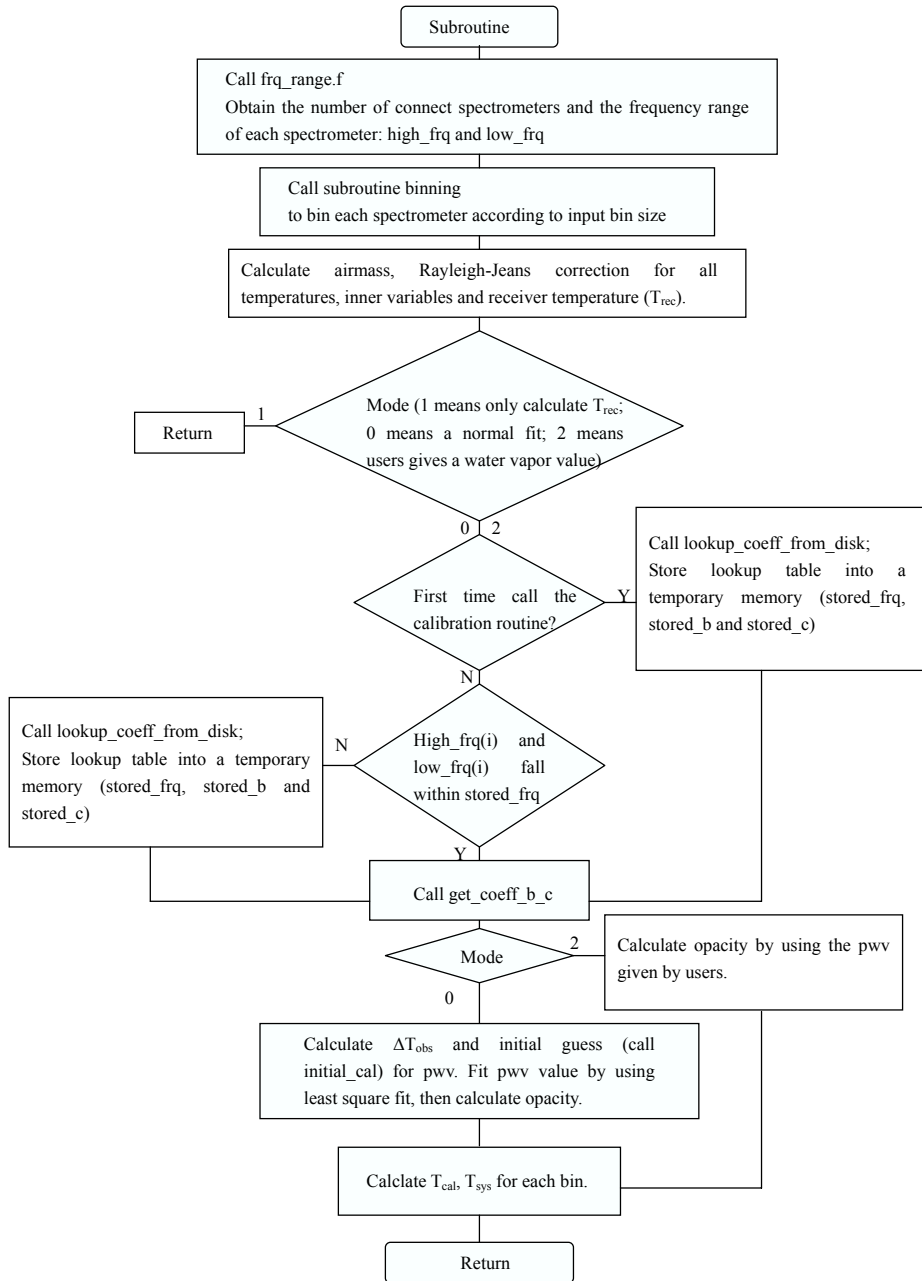
To verify the new calibration routines, I did the comparison with the Hiyama calibration both on the simulation and real observational data. The observational data are from the NANTEN 2 telescope in 2006 and the simulation data are based on the similar setting as the NANTEN 2 observatory.

B.4.1 How to use *Kalibrate*

Here I first give a brief introduction on how to use *Kalibrate*.

1. By typing *kalibrate -h*, one can list all the options for *kalibrate*.

```
Usage: kalibrate [OPTIONS] offlinecal program Options:
-h, --help                this help text
-o, --outputformat <f>   output to class,
                           fits format or none
-O, --offlinemode         Set Offline mode
                           (with KOSMA_file_io)
                           Hint:-OO will skip all
                           not yet written scans
                           and wait for new
```



```

-S, --start-channel      Start Channel (default:700)
-E, --end-channel        End Channel (default:1300)
-s, --scan start[,end]   Scan-Range (default:10000,
                          10008)
-c, --classfile <name>   Set default output file name
                          red
-a, --atmfile <name>      Set default atm file name
                          Default is :/opt/kosma_control
                          /share/atm-table.dat
-d, --datapath <name>    Set default input data path
                          of FITS RAW data
                          Default is :/data1/kosma_control
                          /tmp
-m, --method <name>      Set calibration method (-m help
                          for a list)
-v, --verbose             Increase Verbose level
-G, --guimode             Open display window
                          (offlinecalplot)

```

Send bugs to <jakob@ph1.uni-koeln.de>

The import ones are option *-d* to set input raw data path, option *-a* to give the atm look-up table path;

2. Option *-m* provides interaction between users and the program. By using *kalibrate -m help*, one can list all the available sub-options as shown below:

Help for option *-m*:

```

prefetch=<n>              Prefetch n Scans to catch
                          following load scans
                          (default:1)
interpolate=-1/0/1/2      Allow interpolation between
                          two scans (mode 1)
                          If mode is -1 no interpolation is
                          done and last scans will be used
                          In mode 0 no interpolation is done,
                          but use closest scans
                          In mode 2 extrapolation is
                          also allowed
common=0/1                Common calibration

```

	(default:single)
dsb=0/1	0 - singesideband, 1 - doublesideband
usequality=0/1	If set (default 1) flag output quality
calfactors=0/1	Write out the calibration factors used
tau=0/1	Write out the signal and image band zenit tau
skyhotobs=0/1	Wrtie observed SKY-HOT (default:0)
skyhotfit=0/1	Write fitted SKY-HOT (default:0)
write_loadscans=0/1	Write Trec-Load scans (default:1)
write_combscans=0/1	Write Comb scans (default:1)
write_offscans=0/1	Write Ref scans (default:1)
atmcode=hiyama/kefeng	Choose Fitting code (default:hiyama)
airmass=0/1	Correct airmass between ON and REF
doppler=0/1	Correct doppler velocity for each scan
otfoff=0/1	Create difference scans between two OFFs
expandotf=0/1	Create and calibrate individual spectra for each OTF ON position
pvotf=0/1	Write OTF data in 2dim format
allowskip=<n>	Allows to override n missing subscans (default:5)
tcold=<t>	Override cold load temperature
thot=<t>	Override hot load temperature
tamb=<t>	Override ambient temperature
tsky=<t>	Override sky temperature. If negative, then subtract from tamb
forweff=default	e.g. b0=0.9:b1=0.87
feff=0..1	Override forward efficiency

```

pwv=(>0)           Use this water vapor value
weight=            Weight parameter for individual
                   backends/channels
                   e.g. b0=0.4:b1=1:b2:s0:e2047=0
                   Some global keywords are none
                   /trec/tsys
*azoff=<offset in arcsec>
*eloff=<offset in arcsec>
help               This help text

```

Sub-option *atmcod* (hiyama or kefeng) gives a possibility to switch between the Hiyama atmospheric calibration method and the new atmospheric calibration method. Sub-option *common* (0/1 for single or common calibration). One important option under *-m* is *interpolate*, which allow interpolation between two OFF scans (mode 1) and mode -1 means no interpolation and last OFF scan will be used; mode 0 means no interpolation and the closest OFF scan in time serial will be used; in mode 2 extrapolation is also allowed. For the new calibration, it is also possible to write T_{cal} and $T_{A,sky} - T_{A,hot}$ from observations and fitting out to a CLASS file by setting *calfactors*, *skyhotobs*, *skyhotfit* to 1. Forward efficiency, cold, hot, sky and ambient temperature etc. are also possible to be overwritten via *-m* options;

3. Here I give an example of running *Kalibrate* by giving a raw data path, a atm look-up table, specifying atmcode, overwriting the forward efficiency, and writing T_{cal} , and $T_{A,sky} - T_{A,hot}$ from observations and fitting out to a CLASS file.

```

kalibrate -s 2995,3021 -a /home/kontrol
/nanten2_recalibration/offlinecal_feoff
/atmfeb05_nanten.dat
-d /kosmadaten/raw/kosma_control
/nanten2_thotproblem/complete_data/sep06
-m feff=0.86
-m atmcode=kefeng -m interpolate=-1

```

B.4.2 On simulations

I have tested on several sets of simulation data under different conditions mainly based on the similar setting as the NANTEN 2 observatory. For each simulation data, the input water vapor always varies from 0.2 mm to 2 mm with a step of 0.2 mm. Then I ran *Offlinecal* and *Kalibrate* in both single and common calibration on output raw data and used the same atm look-up table.

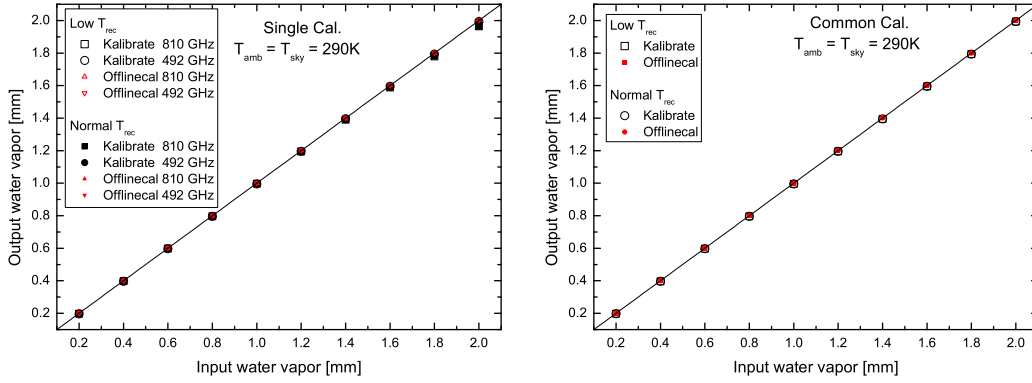


Figure B.1: The the water vapor comparison between the input and calibrated values for low and normal receiver temperatures. The left panel shows the comparison for single calibration and the right panel presents the comparison for common calibration.

In the simulations, one can set ambient temperature T_{amb} and sky temperature T_{sky} using the command *Kset_dummy_atm*. In the raw data fits header there is no item for sky temperature. So the sky temperature is taken as the ambient temperature in data calibration.

The following cases I have tested are a.) different receiver temperature and b.) different ambient temperature T_{amb} and sky temperature T_{sky} relationship with $T_{amb} = T_{sky}$, $T_{amb} > T_{sky}$ and $T_{amb} < T_{sky}$.

B.4.2.1 Different receiver temperature

I used the simulation to test the effect from different receiver temperature on data calibration.

I compared the output water vapor values for both low (~ 40 K for both 810 GHz and 492 GHz) and normal (~ 441 K for 492 GHz and ~ 1336 K for 810 GHz) receiver temperature by using both *OfflineCal* and *Kalibrate*. The results are presented in Figure B.1. For both low and normal receiver temperature, there is no difference in the output water vapor from both *OfflineCal* and *Kalibrate* in single and common calibration modes. And low receiver temperature has no effect on output water vapors, because it has the same output water vapors as normal receiver temperature for both single and calibration modes.

B.4.2.2 Different ambient temperature T_{amb} and sky temperature T_{sky}

As mentioned before, one can set both ambient temperature T_{amb} and sky temperature T_{sky} in the simulations, but sky temperature in the calibration is always set

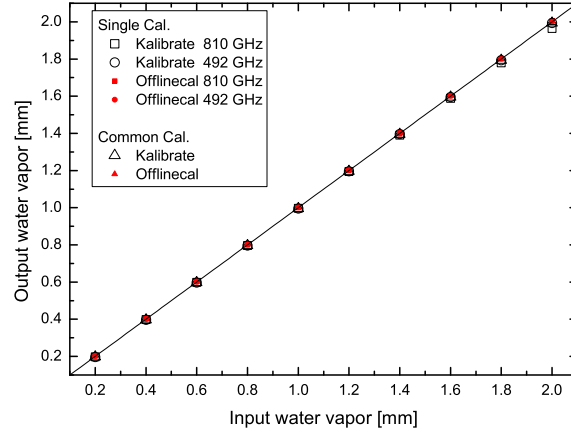


Figure B.2: The the water vapor comparison between the input and calibrated values when T_{amb} is equal to T_{sky} .

to be ambient temperature. In the real data, there are cases that sky temperature is different to ambient temperature. So in this section, I try to simulate the output water vapor behaviors with different ambient temperature and sky temperature relationship.

$$T_{amb} = T_{sky}$$

The ideal case is that sky temperature is equal to ambient temperature. The results are presented in Figure B.2. Within the numerical uncertainty, the output water vapor is the same as the simulation input for both single and common calibrations and both *Offlinecal* and *Kalibrate* give the identical results.

$$T_{amb} > T_{sky}$$

For real data, sky temperature is often lower than ambient temperature. Here, I simulated the that sky temperature is 5 K and 10 K lower than ambient temperature (Note: Although in the simulation T_{amb} is larger T_{sky} , the hardware does not know that. Hence in the calibration, T_{sky} is set to be T_{amb}). The results are presented in Figure B.3.

Within the numerical uncertainty, the output water vapor for single calibrations is identical for both *Offlinecal* and *Kalibrate*, but it is smaller than the input values, especially for the bad water (water vapor > 1.0 mm). At the very bad weather (water vapor > 1.2 mm), the output water vapor for the 810 GHz deviated from the input values bigger than that for the 492 GHz;

The water vapor from the common calibration from both calibration methods is also similar and close to that for 492 GHz from a single calibration. At the bad

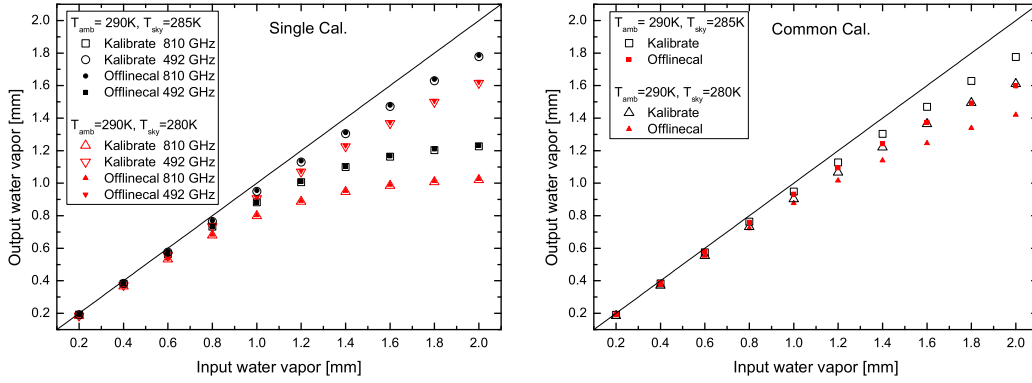


Figure B.3: The the water vapor comparison between the input and calibrated values for sky temperature lower than ambient temperature. The left panel shows the comparison for single calibration and the right panel presents the comparison for common calibration.

weather (water vapor > 1.2 mm) in common calibration, the output water vapor from *Kalibrate* is closer to the input values than that from *Offlinecal*.

For both single and common calibration modes, the lower sky temperature is than ambient temperature, the lower output water vapor is than the input value.

$$T_{amb} < T_{sky}$$

For comparison, I simulated the that sky temperature is 5 K and 10 K greater than ambient temperature (Note: Although in the simulation T_{amb} is lower T_{sky} , the hardware does not know that. Hence in the calibration, T_{sky} is set to be T_{amb}). The results are presented in Figure B.4.

Within the numerical uncertainty, the output water vapor for single calibrations is identical for both *Offlinecal* and *Kalibrate*, but it is greater than the input values, especially for the bad water. At the very bad weather (water vapor ≥ 1.4 mm for the case that T_{sky} is 5 K greater than T_{amb} and water vapor ≥ 1.2 mm for the case that T_{sky} is 10 K greater than T_{amb}), there is no solution of output water vapor for the 810 GHz for both *Kalibrate* and *Offlinecal*;

The water vapor from the common calibration from both calibration methods is also similar and close to that for 492 GHz from a single calibration. While the output water vapor from *Kalibrate* is closer to the input values than that from *Offlinecal*. In the common calibration, *Offlinecal* takes the water vapor for 492 GHz from a single calibration as the common water vapor value when there is no solution for 810 GHz from a single calibration, while *Kalibrate* treats differently by using a receiver temperature weighted method.

For both single and common calibration modes, the greater sky temperature is

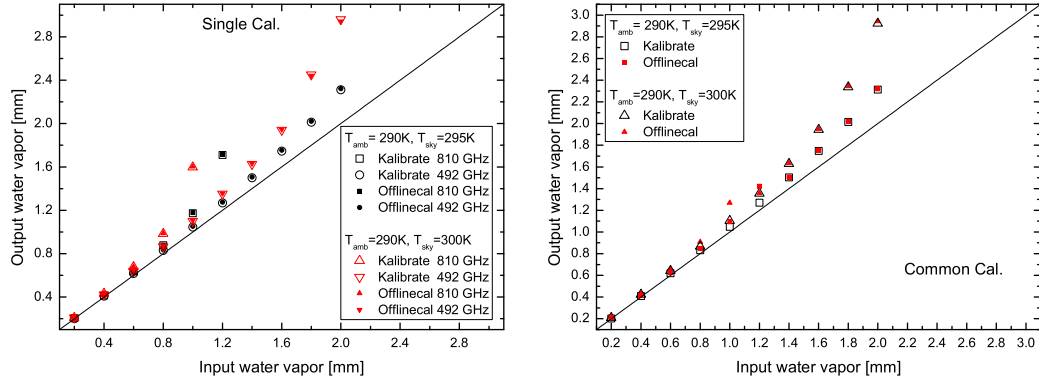


Figure B.4: The the water vapor comparison between the input and calibrated values for sky temperature greater than ambient temperature. The left panel shows the comparison for single calibration and the right panel presents the comparison for common calibration.

than ambient temperature, the larger output water vapor is than the input value.

B.4.3 On real data

I compared water vapor between the Hiyama and the new calibration methods in single calibration mode (Figure B.5) for all NANTEN2 data (both 810 GHz and 492 GHz) observed during September, 2006. For most of data, those two methods give very similar water vapor.

B.5 Conclusion

Receiver temperature has little effect on the output water vapor. Both simulation and real data show that *Kalibrate* and *Offlinecal* give very similar water vapor, especially for the single calibration mode. For common calibration mode, the fitted output water vapor from *Kalibrate* is closer to the input value than that from *Offlinecal*;

In real data, T_{sky} is always set to be T_{amb} . The fitted output water has a strong connection with the relationship between T_{sky} and T_{amb} . The fitted output and input water vapor is identical when $T_{\text{sky}} = T_{\text{amb}}$; the fitted output water vapor is less than input water vapor when $T_{\text{sky}} < T_{\text{amb}}$; the fitted output water vapor is greater than input water vapor when $T_{\text{sky}} > T_{\text{amb}}$. The T_{sky} is assumed to be the same as T_{amb} currently. While the difference between T_{sky} and T_{amb} will different output water vapor, it may be worth fitting both water vapor and T_{sky} in the future.

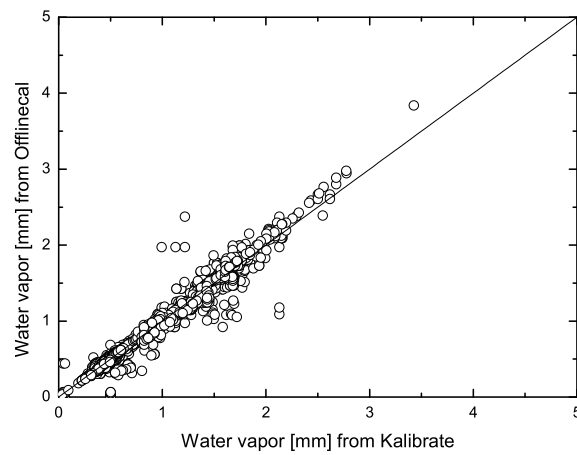


Figure B.5: The water vapor comparison between the Hiyama and the new calibration methods. The drawn lines are where the two methods give the same water vapor.

Generally, common calibration give a more reliable output water vapor.

Appendix C

A uniform observing script

In this appendix, I will describe a uniform observing script for the KOSMA control software, which is a state of art telescope control software developed in I. Physikalisches Institut, Universität zu Köln. Currently this observing script is used in the NANTEN 2 observatory.

The NANTEN 2 Observatory (NANTEN is japanese for southern sky) is a collaboration between research institutes in Japan (Nagoya and Osaka University), South Korea (Seoul National University), Germany (KOSMA, Universität zu Köln, Argelander-Institut Universität Bonn), and Chile (Universidad de Chile). The observatory is located at 4900 m altitude on Pampa la Bola in the Atacama desert, Chile. Equipped with a 4 m submillimeter telescope, NANTEN 2 will be used to survey the southern sky in molecular and atomic spectral lines between 110 and 880 GHz (<http://www.astro.uni-koeln.de/nanten2/>).

At the beginning of observing with the NANTEN 2 telescope, every observer has to write his own observing script for each of his project, even for each different observing mode: position switch mode, on-the-fly mode and etc.. So it is difficult for a fresh observer to start his observation immediately. Furthermore, because each observer uses his own script, it is hard to track the observation history such as the ON time, the map size and so on.

Under such condition, a uniform and easily-used observing script is essentially needed. I created a uniform observing script using Linux shell language, which works as an interface between observers and telescope control software (the KOSMA control software). It has been installed and used at the NANTEN 2 observatory since 2006.

This observing script contains two parts: one is the main program in linux shell scripts and the other is a simple ASCII input file that can be modified to different observations. In addition, the script also supports the input parameters using command lines.

Observing.sh is a uniform observing script now and it is in */home/observer/bin*

of the **kosma** pc at the NANTEN2 site. So there is no need to copy it into different source directories.

To set up observing parameters, one can use input file, command line or both. The basic usage is below.

- *observing.sh -h*; give the help;
- *observing.sh -N n*; disable display of the input parameters (the default option is *yes*);
- *observing.sh*; the script will take the default input parameter file *in.par* in the directory where the script is running.
- *observing.sh -f filename (or path+filename)*; the script will take the given input file;
- *observing.sh -GhfmSRlbtMOgLBadcnoCse values*; give the options via command line. For example:
 - *observing.sh -S sourcename -R refname -l mapcenterlam -b mapcenterbet*; in this case, the script will take the source name, reference name, map center (or desired position for psw) in lam and map center (or desired position for psw) in bet from the command line and the rest parameters from the default input file *in.par*.
 - *observing.sh -S sourcename -R refname -f inputfile*; in this case, the script will take the source name and reference name from the command line and the rest parameters from the give input file

Parameters given from command line have a higher priority. It means if one sets the same parameter both in the input file and via command line, only the one from the command line will be taken.

If option *-N* is *yes*, the script will first display the parameters again in the screen before starting an observation. One has to type *y(Y) + Enter* to continue and type *n(N) + Enter* to quit.

The default log file is stored in a file called *observinglogs* in the same directory where one runs the script. One can use the option *-G logfile (or path+logfile)* to set up a log file.

Below are some examples for carrying out different observing modes (the examples here are using the input parameter file, one can also carry out the same observations by using the proper options via command line).

- absolute or relative reference positions. to use an absolute reference, just give the ref name in *refname*; to use a relative reference, one need to do the following: set *refname* to **NAN**; then give the relative offsets (arcsec) in *reffl* and *reffb*.
- otf map. set mode to *otfl* or *otfb* (*otfl* means otf scans in +l direction; *otfb* means otf scans in +b direction. The otf mode used in the former version of the script will be automatically set to *otfl*); give source name and ref name in *source* and *refname*; give the center of the map in *lam* and *bet*; give the ON time in *ton* (this is the ON time per dump! The OFF time is calculated from ON time); set map step in *step* (for the test receiver, 10'' is used for a fully sampled map); set map size in *mapsize_l* and *mapsize_b*; set the map and ref coord. system in *cormap* and *corref*.
- psw observation. set mode to *psw*; give source name and ref name in *source* and *refname*; give the observed position in *lam* and *bet*; give the ON time in *ton* (OFF time is the same as ON time); set how many cycles and scans in *ncycle* and *nscans* (In each cycle, there is a calibration comb/sky.) set the map and ref coord. system in *cormap* and *corref*.
- pswcross. set mode to *pswcross*; give source name and ref name in *source* and *refname*; give the center of the cross in *lam* and *bet*; give the integration time in *ton* (OFF time is the same as ON time); set cross step in *step* (for the test receiver, 10'' is used for a fully sampled map); if one wants to do a 3×3 cross, then set the *crossnum* as 3; set the map and ref coord. system in *cormap* and *corref*.
- pswrast map. set mode to *pswrast*; give source name and ref name in *source* and *refname*; give the center of the map in *lam* and *bet*; give the ON time in *ton*; set the *onsperoff* value (it will calculate OFF time means how many ONs after one OFF); set map step in *step*; set map size in *mapsize_l* and *mapsize_b*; set the map and ref coord. system in *cormap* and *corref*.
- pswmap. set mode to *pswmap*; give source name and ref name in *source* and *refname*; give the center of the map in *lam* and *bet*; give the ON time in *ton* (OFF time is the same as ON time); set map step in *step*; set map size in *mapsize_l* and *mapsize_b*; set the map and ref coord. system in *cormap* and *corref*.
- dbs observations (the same for swa and swb observations). set mode to *dbs* (or *swa* or *swb*) give source name in *source*; give the observed position in *lam* and *bet*; give the beam switch time in *ton*; map and ref coord. system are always **HORIZON** no matter what is set in *cormap* and *corref*; wobbler

amplitude (*chop_amp*) and frequency (*chop_frq*) are fixed to be 82'' in Az and 1.01 Hz, respectively for the NANTEN2, unless there will be new measurements to indicate a different value. for dbs mode, one can use *dbs_num* to set numbers of dbs cycle; to observe a single position, a cross or a map, the rest parameters are the same as for psw mode.

Bibliography

- Adams, W. S. 1941, ApJ, 98, 11
- Allan, D. W. 1966, Proc. IEEE, 54, 221
- Alten, V. P., Bally, J., Devine, D. & Miller, G. J. 1997, in IAU Symp. 182 Poster Proc., Low Mass Star Formation Infall to Outflow, ed. F. Malbet & A. Castets (Grenoble, Obs. Grenoble) 51
- Alves et al. 2005 in preparation
- Aspin, C., Sandell, G. & Russel, A. P. G. 1994, A&AS, 106,165
- Aumann, H. H., Fowler, J. W., & Melnyk, M. 1990, AJ, 99, 1674
- Bachiller, R. 1985, Ph.D Thesis, Université de Grenoble
- Bachiller, R. & Cernicharo, J. 1984, A&A, 140, 414
- Bachiller, R. & Cernicharo, J. 1986, A&A, 168, 262
- Bachiller, R.; Martin-Pintado, J. & Planesas,P. 1991, A&A, 251,639
- Bachiller, R., Menten, K. M. & del Rio-Alvarez, S. 1990, A&A, 236,461
- Bally, J.; Devine, D.; Alten, V. & Sutherland, R. S. 1999, AJ, 478,603
- Bally, J., Devine, D. & Reipurth, B. 1996, ApJ, 473,L49
- Bally, J.; Stark, A. A.; Wilson, R. W. & Langer, W. D. 1987,ApJ, 312, 45
- Barnard, E. E. 1919, AJ, 49, 1
- Baudry, A., Combes, F., Perault, M. & Dickman, R. 1980, A&A, 85, 244
- Beech, M. 1986, Astrophys. Space Sci., 133, 193

- Bell, T. A., Viti, S., Williams, D. A., Crawford, I. A. & Price, R. J. 2005, MNRAS, 357, 961
- Bensch, F. & Simon, R. Poster in Star Formation Workshop, July 14-19, 2001, Santa Cruz, CA, USA
- Bensch, F., Stutzki, J. & Ossenkopf, V. 2001, A&A, 366, 636
- Bergin, E. A., Kaufman, M. J., Melnick, G. J. et al. 2003, ApJ, 582, 830
- Bertoldi, F. & Draine, B. T 1996, ApJ, 458, 222
- Bertoldi, F. & McKee, C. F. 1992, ApJ, 395, 140
- Beuther, H. 1999, On The Fly Kartierung und Multilinienanalyse der interstellaren Molekülwolke Cepheus B, Diploma thesis, Universität zu Köln
- Beuther, H., Kramer, C., Deiss, B. & Stutzki, J. 2000, A&A, 362, 1109
- Blaauw, A. 1964, ARA&A, 2, 213
- Blake, G. A.; Sutton, E. C.; Masson, C. R. & Phillips, T. G. 1987, ApJ, 315, 621
- Blitz, L. 1993, Giant Molecular Clouds. In: Levy E.H., Lunine J.I. (eds.), Protostars and Planets III. The University of Arizona Press, Tuscon & London
- Boger, G. I. & Sternberg, A. 2005, ApJ, 632, 302
- Bohlin, R. C., Savage, B. D. & Drake, J. F. 1978, ApJ, 224, 132
- Borgman, J. & Blaauw, A. J. 1964, Bull. Astron. Inst. Netherlands, 17, 358
- Boulares, A. & Cox, D. P. 1990, ApJ, 365, 544
- Burke, B. F. & Graham-Smith, F. 2002, An introduction to Radio Astronomy, second edition, Cambridge University press
- Carr, J. S. 1987, ApJ, 323, 170
- Cazaux, S. & Tielens, A. G. G. M. 2004, ApJ, 604, 222
- Ceccarelli, C., Caux, E., Tielens, A. G. G. M., Kemper, F., Waters, L. B. F. M. & Phillips, T 2002, A&A, 395, L29
- Cernis, K. 1990, ApJS166, 315
- Cernicharo, J. 1985, ATM: A program to compute theoretical atmospheric opacity for frequencies ≤ 1000 GHz, Tech. rep., IRAM

- Cheung, A. C., Rank, D. M., Townes, C. H., Thornton, D. D. & Welch, W. J. 1968, *Phys. Rev. Lett.*, 21, 1701
- Combes, F. 2001, *ApSSS*, 277, 29
- Corneliussen, U., 1996, Ph.D. thesis, University of Cologne
- Cox, D. P. 2005, *ARA&A*, 43, 337
- Crovisier, J. & Dickey, M. 1983, *A&A*, 122, 282
- Crutcher, R. M., Churchwell, E. & Ziurys, L. M. 1984, *ApJ*, 321, 516
- Crutcher, R. M., Troland, T. H., Goodman, A. A., Heiles, C., I., Kazès, & Myers, P. C. 1993, *ApJ*, 407, 175
- Cubick, M. 2005, The contribution of photon dominated regions to the far-infrared emission of the Milky Way: construction of PDR models, Diploma thesis, Universität zu Köln
- Cubick, M., Röllig, M., Ossenkopf, V., Kramer, C., & Stutzki, J. 2008, submitted to *A&A*,
- Cubick M., Roellig M., Ossenkopf V., Kramer C., Stutzki J. 2007, *A&A*, in prep.
- Dame, T., Elmegreen, B. G., Cohen, R. & Thaddeus, P. 1986, *ApJ*, 305, 892
- Dame, T. M., Hartmann, D., & Thaddeus, P. 2001, *ApJ*, 547, 792
- de Boisanger, C. B., Chieze, J. P. & Meltz, B. 1992, *ApJ*, 401, 182
- de Jager, C. & Nieuwenhuijzen, H. 1987, *A&A*, 177, 217
- de Jong, T., Boland, W. & Dalgarno, A. 1980, *A&A*, 91, 68
- di Francesco, J., Myers, P. C., Wilner, D. J., Ohashi, N. & Mardones, D. 2002, *Hot Star Workshop III: The Earliest Stages of Massive Star Birth*. ASP Conference Proceedings, Vol. 267. Edited by Paul A. Crowther. ISBN: 1-58381-107-9. San Francisco, Astronomical Society of the Pacific, p.365
- Dickey, J. M., McClure-Griffiths, N. M., Stanimirović, S., Gaensler, B. M. & Green, A. J. 2001, *ApJ*, 561, 264
- Dobashi, K., Bernard, J. P. & Fukui, Y. 1996, *ApJ*, 466, 282
- Draine, B. T. 1978, *ApJS*, 36, 595

- Draine, B. T. & Bertoldi, F. 1996, *ApJ*, 468, 269
- Eisloffel, J., Froebrich, D.; Stanke, T. & McCaughrean, M. J. 2003, *ApJ*, 595, 259
- Elmegreen, B. G. 1991, In *The Physics of Star Formation and Early Stellar Evolution*, ed. CJ Lada, ND Kylafis, pp. 35C60. Dordrecht: Kluwer
- Elmegreen, B. G. 1999, *ApJ*, 527, 266
- Elmegreen, B. G. & Falgarone, E. 1996, *ApJ*, 471, 816
- Elmegreen, B. G., Kim, S. & Staveley-Smith, L. 2001, *ApJ*, 548, 749
- Elmegreen, B. G. & Scalo, J. 2004, *ARA&A*, 42, 211
- Esquivel, A., Lazarian, A., Pogosyan, D., Cho, J. 2003, *MNRAS*, 342, 325
- Esquivel, A., Lazarian, A., Horibe, S. et al. 2007, *MNRAS*, 381, 1733
- Evans II, N. J., Allen, L. E., Blake, G. A. et al. 2003, *PASP*, 115, 965
- Ewen, H. & Purcel, E. 1951, *Nature* 168, 356
- Falgarone, E., Hily-Blant, P., Levrier, F. 2004, *Ap&SS*, 292, 89
- Falgarone, E., & Phillips, T. G. 1996, *ApJ*, 472, 191
- Falgarone, E., Phillips, T. G. & Walker, C. K. 1991, *ApJ*, 378, 186
- Felli, M., Tofani, G., Harten, R. H. & Panagia, N. 1978, *A&A*, 69, 199
- Ferrière, K. M. 2001, *Rev. of Mod. Phys.*, 73, 1031
- Fiege, J. D., & Pudritz, R. E. 2000, *MNRAS*, 311, 105
- Field, G. B., Somerville, W. B. & Dressler, K. 1966, *ARA&A*, 4, 207
- Flannery, B.P., Roberge, W. & Rybicki, G.B. 1980, *ApJ*, 236, 598
- Frerking, M. A., Langer, W. D. & Wilson, R. W. 1982, *ApJ*, 262, 590
- Fuente, A., Martín-Pintado, J., Cernicharo, J. & Bachiller, R. 1993, *A&A*, 276, 473
- García-Burillo, S., Martín-Pintado, J., Fuente, A., Usero, A. & Neri, R. 2002, *ApJ*, 575, L55

- Garden, R. P., Hayashi, M., Gatley, I., Hasegawa, T. & Kaifu, N. 1991, *ApJ*, 374, 540
- Gehman, C. S., Adams, F. C., & Watkins, R. 1996, *ApJ*, 472, 673
- Getman, K., Feigelson, E., Townsley, L., Bally, J., Lada, C. & Reipurth, B. 2002, *ApJ*, 575, 354
- Glada, G. & Rodríguez, L. F. 2002, *Revista Mexicana de Astronomía y Astrofísica* Vol. 38, pp. 13-21
- Glassgold, A. E. & Langer, W. D. 1975, *ApJ*, 197, 347
- Goodman, A. A. 2004, *ASP Conference Series*, 323, 171
- Goodman, A. A., Crutcher, R. M., Heiles, C., Meyers, P. C., & Troland, T. H. 1989, *ApJ*, 338, L61
- Gottlieb, C. A., Lada, C. J. Gottlieb, E. W., Lilley, A. E. & Litvak, M. M. 1975, *ApJ*, 202, 655
- Graf, U.U., Honingh, C. E., Jacobs, K., Schieder, R., Stutzki, J. 1998, In *Astronomische Gesellschaft Meeting Abstracts*, 14, 120
- Graf, U. U., Heyminck, S., Michael, E. A., et al. 2002, in *Millimeter and Submillimeter Detectors for Astronomy*, ed. T. G. Phillips, & J. Zmuidzinas, *Proc. SPIE*, Hawaii/USA, 4855, 99, 167
- Greaves, J. S. & White, G.J. 1992, *MNRAS*, 259, 457
- Green, D. A. 1993, *MNRAS*, 262, 327
- Habing, H. J. 1968, *Bull. Astron. Inst. Netherlands* 19, 421.
- Hatchell, J.; Richer, J. S.; Fuller, G. A.; Qualtrough, C. J.; Ladd, E. F. & Chandler, C. J. 2005, *A&A*, 440, 151
- Heger, M. L. 1922, Further study of the sodium lines in class B stars ; The spectra of certain class B stars in the regions 5630A-6680A and 3280A-3380A ; Note on the spectrum of [gamma] Cassiopeiae between 5860A and 6600A. *Lick Observatory bulletin* ; no. 337; *Lick Observatory bulletins* ; no. 337., Berkeley : University of California Press, [1922], p. 141-148
- Hegmann, M. & Kegel, W. H. 1996, *MNRAS*, 283, 167
- Heikkilä, A., Johansson, L. E. B. & Olofsson, H. 1999, *A&A*, 344, 817

- Heithausen, A. 1996, A&A, 314, 251
- Heithausen, A.; Bensch, F.; Stutzki, J.; Falgarone, E. & Panis, J. F. 1998, A&A, 331, 65
- Heitsch, F., Mac Low M. M., Klessen, R. S. 2001, ApJ, 547, 280
- Herbertz, R., 1992, Ph.D. thesis, University of Cologne
- Herbig, G. H. 1974, Draft catalog of Herbig-Haro object No.1, IBVS, no.832
- Herbig, G. H. 1998, AJ, 497, 736
- Herbig, G. H. & Jones, B. F. 1983, AJ, 88, 1040
- Herbst, W., Maley, J. A. & Williams, E. C. 2000, AJ, 120,349
- Heyer, M. H., Brunt, C., Snell, R. L., Howe, J. E., Schloerb, F. P. & Carpenter, J. M. 1998, ApJS, 115, 241
- Heyer, M. H., Carpenter, J. M. & Snell, R. L. 2001, ApJ, 551, 852
- Heyer, M. H. & Schloerb, F. P. 1997, ApJ, 475, 173
- Heyer, M. H. & Terebey, S. 1998, ApJ, 502, 265
- Hill, J. K. & Hollenbach, D. J. 1978, ApJ, 225, 390
- Hiltner, W. A. 1949, ApJ, 109, 471
- Hiyama, S. 1998, Seitenbandkalibration radioastronomischer Linienbeobachtungen, Diploma thesis, Universität zu Köln
- Hirano, N., Kamazaki, T., Mikami, H., Saito, S., Umemoto, T. & Yamamoto, S. 1999, ApJ, 478,631
- Hobson, M.P., 1992, MNRAS, 256, 457
- Hobson, M.P., Jenness, T., Padman, R. & Scott, P.F., 1994, MNRAS, 266, 972
- Hodapp, K. W. & Ladd, E. F. 1995, ApJ, 453,715
- Hogerheijde, M. R., van Dishoeck, E. F., Blake, G. A. & van Langevelde, H. J. 1997, ApJ, 489, 293
- Hollenbach, D. & Salpeter, E. E. 1971, ApJ, 163, 155
- Hollenbach, D. J. & Tielens, A. G. G. M. 1997, ARA&A, 35, 179

- Hollenbach, D. J. & Tielens, A. G. G. M. 1999, *Rev of Mod. Phhys.*, 71, 173
- Horn, J., Siebertz, O., Schmülling, F., et al. 1999, *Exp. Astron.*, 9, 17
- Hollenbach, D., Werner, M. W. & Salpeter, E. E. 1971, *ApJ*, 163, 165
- Hossack, W. R. & Hogg, F. S. 1949, *AJ*, 54, R189
- Howe, J. E., Jaffe, D. T., Genzel, R. & Stacey, G. J. 1991, *ApJ*, 373, 158
- Israel, F. P., & Baas, F. 2002, *A&A*, 383, 82
- Itoh, M., Fukunaga, H., Sekimoto, Y., Tatematsu, K. & Koyama, K. 1999, *sf99. proc 100*
- Jenkins, E. B., Jura, M. & Loewenstein, M. 1983, *ApJ*, 270, 88.
- Jennings, R. E., Cameron, D. H. M., Cudlip, W. & Hirst, C. J. 1987, *MNRAS*, 226, 461
- Johnen, C., 1992, *Diplom thesis, University of Cologne*
- Johnstone, D. & Bally, J. 2006, *ApJ*, 653, 383
- Johnstone, D., Wilson, C. D., Moriarty-Schieven, G. et al. 2000, *ApJ*, 545, 327
- Juan, J., Bachiller, R., Koempe, C. & Martin-Pintado, J. 2000, *A&A*, 270, 432
- Jura, M. 1974, *ApJ*, 191, 375
- Jura, M. 1976, *AJ*, 204, 12.
- Kaufman, M., Wolfire, M., Hollenbach, D., & Luhman, M. 1999, *ApJ*, 527, 795
- Kirk, H., Johnstone, D. & Di Francesco, J. 2006, *ApJ*, 646, 1009
- Klein, S. C. & Dickman, R. L. 1984, *ApJ*, 286, 255
- Klein, S. C. & Dickman, R. L. 1987, *ApJ*, 312, 837
- Klessen, R. S., & Burkert, A. 2000, *ApJS*, 128, 287
- Kolmogorov AN. 1941. *Proc. R. Soc. London Ser. A* 434:9C13. Reprinted in 1991
- Kramer, C., Beuther, H., Simon, R., Stutzki, J., & Winnewisser, G. 1999, *Imaging at radio through submillimetre wavelength*, ed. J. G. Mangum, & S. J. E. Radford, *Astronomical Society of the Pacific*, CF-217

- Kramer, C., Cubick, M., Röllig, M., et al. 2008, *A&A*, 477, 547
- Kramer, C., Degiacomi, C., Graf, U., et al. 1998, in *Advanced Technology MMV, Radio, and Terahertz Telescopes*, ed. T. Phillips, *Proc. SPIE*, Kona/Hawaii/USA, 3357, 71
- Kramer, C., Jakob, H., Mookerjea, B., Schneider, N., Brüll, M. & Stutzki, J. 2004, *A&A*, 424, 887
- Kramer C., Mookerjea B., Bayet E., Garcia-Burillo S., Gerin M., Israel F. P., Stutzki J. & Wouterloot J.G.A, 2005, *A&A*, 441, 961
- Kramer, C., Stutzki, J., Röhrig, R. & Corneliussen, U. 1998, *A&A*, 329, 249
- Kramer C., Stutzki J. & Winnewisser, G. 1996, *A&A*, 307, 915
- Kulkarni, S. R. & Heiles, C. 1987, in *Interstellar Processes*, edited by D. J. Hollenbach and H. A. Thronson (Reidel, Dordrecht), p. 87
- Langer, W. D. & Penzias, A. A. 1990, *ApJ*, 357, 477
- Larson, R. B. 1981, *MNRAS*, 194, 809
- Lazarian, A. & Pogosyan, D. 2000, *ApJ*, 537, 720
- Lazarian, A. & Pogosyan, D. 2004, *ApJ*, 616, 943
- Lada, C. J., Alves, A. & Lada, E. A. 1996, *AJ*, 111, 1964
- Lada, E.A., Bally, J. & Stark, A. A. 1991, *ApJ*, 368, 432
- Lada, E. A., & Lada, C. J. 1995, *AJ*, 109, 1682
- Ladd, E. F., Lada, E.A. & Myers, P. C. 1993, *ApJ*, 410, 168
- Langer, W. D. & Penzias, A. A. 1990, *ApJ*, 357, 477
- Langer, W. D., Wilson, R.W. & Anderson, C. H. 1993, *ApJ*, 408, L45
- Lapinov, A. V., Schilke, P., Juvela, M. & Zinchenko, I. I. 1998, *A&A*, 336, 1007
- Lazarian, A. & Pogosyan, D. 2000, *ApJ*, 537, 720
- Lazarian, A. & Pogosyan, D. 2004, *ApJ*, 616, 943
- Lazarian, A.; Pogosyan, D.; Vázquez-Semadeni, E. & Pichardo, B. 2001, *ApJ*, 555, 130

- Le Bourlot, J., Pineau Des Forêts, G., Roueff, E. & Flower, D. R. 1993, A&A, 267, 233
- Leung, C. M., Kutner, M. L. & Mead, K. N. 1983, ApJ, 262, 583
- Leurini, S., Rolffs, R., Thorwirth, S. et al. 2006, A&A, 454, L47
- Little, L. T & Matheson, D. N. 1973, MNRAS, 162, 329C38
- Lis, D. C., Roueff, E., Gerin, M., Phillips, T. G., Coudert, L. H., van der Tak, F. F. S. & Schilke, P 2001, ApJ, 571,L55
- Liseau, R., Sandell, G. & Knee, L. B. G. 1988, A&A, 192,153
- Loren, R. B. 1989, ApJ, 338, 902
- Luhman, K. L., Lada, E. A., Muench, A. A, & Elston, R. J. 2005, ApJ, 618, 810
- Luhman, K. L., Rieke, G. H., Lada, C. J, & Lada, E. A. 1998, ApJ, 508, 347
- Luhman, K. L., Stauffer, J. R. & Muench, A. A, et al. 2003, ApJ, 593, 1093
- Maron, J. & Goldreich, P. 2001, ApJ, 554,1175
- Masur, M. 2005, Diploma thesis, Universität zu Köln
- Matthews, B. C. & Wilson, C. D 2003, ApJ, 574,822
- McKee, C. F.& Ostriker, E. C. 2007, ARA&A, 45, 565
- McKee, C. F. & Ostriker, J. P. 1977, ApJ, 218, 148
- McKellar, A. 1940, PASP, 52, 187
- Meijerink, R. & Spaans, M. 2005, A&A, 436, 397
- Meixner, M., & Tielens, A. G. G. M. 1993, ApJ, 405, 216
- Miesch, M. S. & Bally, J. 1994, ApJ, 429, 645
- Minchin, N. R., Ward-Thompson, D. & White, G. J. 1992, A&A, 265, 733
- Minkowski, R. 1955. In Gas Dynamics of Cosmic Clouds, ed. J. M. Burgers, H. C. van de Hulst, pp. 3C12. Amsterdam: North Holland
- Mookerjea, B., Kramer, C., Nielbock, M. & Nyman, L. A&A, 2004, A&A, 426, 119

- Mookerjea, B., Kramer, C., Röllig, M. & Masur, M. 2006, *A&A*, 456, 235
- Moreno-Corral, M., Chavarria, K.C., Lara, E. & Wagner, S. 1993, *A&A*, 98, 295
- Nozawa, S., Mizuno, A., Teshima, Y., et al. 1991, *ApJS*, 77, 647
- Muller, C. A. & Oort, J. H. 1951, *Nature*, 168, 357
- Myers, P. C. 1983, *ApJ*, 270, 105
- Myers, P. C. 1987, in *Interstellar Processes*, ed. D. J. Hollenbach & H. A. Thronson (Dordrecht: Reidel), 71
- Myers, P. C. & Goodman, A. A. 1988, *ApJ*, 329, 392
- Najita, J. R., Tiede, G. P. & Carr, J. S. 2000, *ApJ*, 541, 977
- Nakagawa, T., Yui, Y. Y., & Doi, et al. 1998, *ApJS*, 115, 259
- Nakajima, Y., & Hanawa, T. 1996, *ApJ*, 467, 321
- Nejad, L. A. M. & Wagenblast, R. 1999, *A&A*, 350, 204
- Neufeld, D. A., Schilke, P., Menten, K. M. et al. 2006, *A&A*, 454, L37
- Oka, T., Iwata, M., Maezawa, H., Ikeda, M., Ito, T., Kamegai, K., Sakai, T. & Yamamoto, S. 2004, *ApJ*, 602, 803
- Ossenkopf, V., Esquivel, A., Lazarian, A. & Stutzki, J. 2006, *A&A*, 452, 223
- Ossenkopf, V., Klessen, R. S. & Heitsch, F. 2001, *A&A*, 379, 1005
- Ossenkopf, V. & Mac Low, M. M. 2002, *A&A*, 390, 307
- Ossenkopf, V., Röllig, M., Cubick, M., & Stutzki, J. 2007, *Molecules in Space & Laboratory*, Paris, ed. J. L. Lemaire & F. Combes, 950
- Ostriker, E. C., Stone, J. M., Gammie, C. F. 2001, *ApJ*, 546, 980
- Padoan, P., Boldyrev, S., Langer, W. & Nordlund, Å, 2003a, *ApJ*, 583, 308
- Padoan, P., Bally, J., Billawala, Y., Juvela, M. & Nordlund, Å. 1999, *ApJ*, 525, 318
- Padoan, P., Goodman, A. A. & Juvela, M. 2003b, *ApJ*, 588, 881
- Padoan, P., Juvela, M., Bally, J., & Nordlund, Å. 1998, *ApJ*, 504, 300

- Panagia, N. & Thum, C. 1981, *A&A*, 98, 295
- Pardo, J. R., Cernicharo, J & Serabyn, E. 2001, *IEEE Trans. on Antennas and Propagation*, 49/12, 1683
- Pardo, Serabyn, E., Wiedner, M. C. & J. R., Cernicharo, J, 2005, *J. Quant. Spec. and Radiat. Transfer* 96/3-4, 537
- Patrikeev, I., Fletcher, A., Stepanov, R. et al. 2006, *A&A*, 458, 441
- Pety, J., Teyssier, D., Fossé, D., Gerin, M., Roueff, E. et al. 2005, *A&A*, 435, 885
- Pérault, M., Falgarone, E. & Puget, J. L. 1986, *A&A*, 157, 139
- Plume, R., Bensch, F., Howe, J. E. et al. 2000, *ApJ*, 539, L133
- Plume, R., Jaffe, D., Tatematsu, K., et al. 1999, *ApJ*, 512, 768
- Preibisch, T. 2003, *A&A*, 401,543
- Preibisch, T. & Zinnecker, H. 2001, *AJ*, 122, 866
- Preibisch, T. & Zinnecker, H. 2002, *AJ*, 123,1613
- Preibisch, T., Zinnecker, H. & Herbig, G. H. 1996, *A&A*, 310, 456
- Rebull, L. M., Cole, D. M., Stapelfeldt, K. R. & Werner, M. W. 2003, *AJ*, 125,2568
- Rickett, B. J. 1970, *MNRAS*, 150,67
- Ridge, N. A., Wilson, T. L., Megeath, S. T., Allen, L. E., & Myers, P. C. 2003, *AJ*, 126, 286
- Rosolowsky, E. W., Goodman, A. A., Wilner, D. J. & Williams, J. P. 1999, *ApJ*, 524, 887
- Röhrig, R., 1996, Ph.D. thesis, University of Cologne
- Röllig, M., Abel, N. P., Bell, T. et al. 2007, *A&A*, 467, 187
- Röllig, M., Hegmann, M., Kegel, W. H. 2002, *A&A*, 392, 1081
- Röllig, M., Ossenkopf, V., Jeyakumar, S. & Stutzki, J. 2006, *A&A*, 451, 917
- Rudolph, A. L., Bachiller, R., Rieu, N. Q., Trune, D. V., Palmer, P. & Welch, W. J. 2001, *ApJ*, 558,204

- Salpeter, E. E. 1955, *ApJ*, 121, 161
- Sancisi, R. 1974, *IAUS*, 60, 115
- Sandell, G., Aspin, C., Duncan, W. D., Russell, A. P. G. & Robson, E. I. 1991, *ApJ*, 376,L17
- Sandell, G., Knee, L. B. G., Aspin, C., Robson, I. E. & Russell, A. P. G. 1994, *A&A*, 285,L1
- Sanders, D. B., Scoville, N. Z. & Solomon, P. M. 1985, *ApJ*, 289, 373
- Sargent, A. I. 1979, *ApJ*, 233, 163
- Scalo, J. M. 1984. *ApJ*, 277,556
- Scalo, J. M. 1987, in *Plasma Turbulence and Energetic Particles*, ed. M. Ostrowski & R. Schlickeiser (Kraków: Univ. Jagiellonski Astro. Obs.), 1
- Scalo, J. & Elmegreen, B. G. 2004, *ARA&A*, 42, 275
- Schieder, R., Tolls, V., Winnewisser, G. 1989, *Exp. Astron.*, 1, 101
- Schneider, N., Simon, R., Kramer, C., Kraemer, K., Stutzki, J. & Mookerje, B. 2003, *A&A*, 406, 915
- Schröder, K., Staemmler, V., Smith, M. D., Flower, D. R., & Jaquet, R. 1991, *J. Phys. B*, 24, 2487
- Scoville, N. Z., Sargent, A. I., Sanders, D. B., Claussen, M. J. et al. 1986, *ApJ*, 303, 416
- Sharpless, S. 1959, *ApJS*, 4, 257
- Simon, R. 1997, Ph.D. thesis, University of Cologne
- Simon, R., Jackson, J. M., Clemens, D. P., Bania, T. M. & Heyer, M. H. 2001, *ApJ*, 551, 747
- Simon, R., Stutzki, J., Sternberg A. & Winnewisser, G. 1997, *A&A*, 327, 9
- Snow, T. P. & McCall, B. J. 2006, *ARA&A*, 44, 367
- Solomon, P. M., Rivolo, A. R., Barrett, J. & Yahil, A. 1987, *ApJ*, 319, 730
- Spaans, M. 1996, *A&A*, 307, 271

- Spitzer, L. 1978, *Physical Processes in the Interstellar Medium*, Wiley
- Stacey, G. J., Jaffe, D. T., Geis, N., et al. 1993, *ApJ*, 404, 219
- Stanimirović, S. & Lazarian, A. 2001, *ApJ*, 551, L53
- Stanimirović, S., Staveley-Smith, L., Dickey, J. M., Sault, R. J. & Snowden, S. L. 1999, *MNRAS*, 302, 417
- Stenholm, L. G. 1984, *A&A*, 137, 133
- Sternberg, A. & Dalgarno, A. 1989, *ApJ*, 338, 197
- Sternberg, A. & Dalgarno, A. 1995, *ApJS*, 99, 565
- Stutzki, J., Bensch, F., Heithausen, A., Ossenkopf, V. & Zielinsky, M. 1998, *A&A*, 336, 697
- Stutzki, J. & Güsten, R. 1990, *ApJ*, 356, 513
- Stutzki, J., Stacey, G. J., Genzel, R., Harris, A. I., Jaffe, D. T. & Lugten, J. B. 1988, *ApJ*, 332, 379
- Störzer H. & Hollenbach, D. 1998, *ApJ*, 495, 853
- Störzer, H., Stutzki, J. & Sternberg, A. 1996, *A&A*, 310, 592
- Störzer, H., Zielinsky, M., Stutzki, J., & Sternberg, A. 2000, *A&A*, 358, 682
- Sun, K., Kramer, C., Ossenkopf, V., Bensch, F., Stutzki, J. & Miller, M. 2006, *A&A*, 451, 539
- Swings, P. & Rosenfeld, L. 1937, *ApJ*, 86, 483
- Tielens, A. G. G. M. 2005, *The physics and chemistry of the interstellar medium*
- Tielens, A. G. G. M. & Hollenbach, D. 1985, *ApJ*, 291, 722
- Testi, L., Olmi, L. & Hunt, L. et al. 1995, *A&A*, 303, 881
- Teyssier, D., Fossé, D., Gerin, M., Pety, J., Abergel, A. & Roueff, E. 2004, *A&A*, 417, 135
- Trullols, E. & Jordi, C. 1999, *A&A*, 324, 549
- Trumpler, R. J. 1930, *PASP*, 42, 214
- Tucker, K. D., Kutner, M. L. Thaddeus, P. 1974, *ApJ*, 193, L115

- Ungerechts, H., Brunswing, W., Kramer, C. et al. 2000, ASPC, 217, 190
- Ungerechts, H. & Thaddeus, P. 1987, ApJS, 63, 645
- van der Tak, F. F. S., Schilke, P., Müller, H. S. P., Lis, D. C., Phillips, T. G., Gerin, M. & Roueff, E 2002, A&A, 388,L53
- van Dishoeck, E. F. 2006, The lecture's notes of Interstellar Medium course
- van Dishoeck, E. F., Black, J. H. 1988, ApJ, 334, 771
- Vázquez-Semadeni, E., Ostriker, E. C., Passot, T., Gammie, C. F. & Stone, J. M. 2000, in Mannings V., Boss A. P., Russell S. S., eds, Protostars and Planets IV. University of Arizona Press, Tucson, p. 3
- Viti, S., Roueff, E., Hartquist, T. W., Pineau des Forêts, G. & Williams, D. A. 2001, A&A, 370, 557
- Vogelaar, M. G. R. & Wakker, B. P. 1994, A&A, 291, 557
- Von Weizsäcker, C. F. 1951. ApJ, 114,165
- Wagenblast, R. & Hartquist, T. W. 1988, MNRAS, 230, 363
- Walsh, A. J., Myers, P. C., di Francesco, J., Wilner, D. J. & Bourke, T. L. 2003, International Astronomical Union. Symposium no. 221, held 22-25 July, 2003 in Sydney, Australia
- Wang, H. 2003, Doctoral thesis of Purple Mountain Observatory
- Watson, W. D. 1972, AJ, 176, 103.
- Warin, S., Castets, A., Langer, W. D., Wilson, R. W. & Pagani, L. 1996, A&A, 306, 935
- Weinreb, S., Barrett, A. H., Meeks, M. L. & Henry, J. C. 1963, Nature, 200, 829
- Wiesemeyer, H., Guesten, R., Wink, J. E. & Yorke, H. W. 1997, A&A, 320,287
- Williams, J. P., Blitz, L. & McKee, C. F. 2000, in Protostars and Planets IV, ed. V. Mannings, A. P. Boss, & S. S. Russell (Tucson: Univ. Arizona Press), 97
- Williams, J. P., Blitz, L. & Stark, A. A. 1995, ApJ, 451, 252
- Williams, J. P., de Geus, E. J. & Blitz, L. 1994, ApJ, 428, 693
- Wilson, R. W., Jefferts, K. B. & Penzias, A. A. 1970, ApJ, 161, 43

- Winnewisser, G., Bester, M., & Ewald, R. 1986, A&A, 167, 207
- Wong, T., Ladd, E. F., Brisbin, D. et al. 2008, submitted to MNRAS
- Yu, K. C., Billawala, Y. & Bally, J. 1999, AJ, 118, 2940
- Zimmermann, T., 1993, Ph.D. thesis, University of Cologne
- Zimmermann, T. & Stutzki, J. 1993, Fractals, 1, 930
- Zinnecker, H., McCaughrean, M.J. & Wilking, B.A. 1993, The initial stellar population. In: Levy E.H., Lunine J.I. (eds.), Protostars and Planets III. The University of Arizona Press, Tuscon & London
- Ziurys, L. M. Saykally, R. J., Plambeck, R. L. & Erickson, N. R. 1982, ApJ, 254, 94

List of Figures

1.1	Hubble space telescope image of Cone nebula (NGC2264): star forming pillar of gas and dust.	2
1.2	Example of the filter function used in the Δ -variance analysis . . .	6
1.3	An example of a typical Δ -variance spectrum for a subset of the FCRAO outer galaxy survey (^{13}CO 1–0). This subset has a very large scale (384 by 128 pixels; 50'' per pixel). The x axis is the lag and the y axis is the value of the variance. The black line indicates the power-law fits to the data. The turnover at the smallest angular scales shows the effect from the white noise behavior (for pure white noise, $\sigma_{\Delta}^2(L) \propto L^{-2}$); the turnover at the large angular scales is due to the influence of the typical size of main structures in the image. The figure is adapted from the Fig. 3 in the paper by Stutzki et al. (1998).	7
1.4	An example of a clump mass spectrum for clump mass spectra of NGC 7538. All spectra are fitted by a power law function $dN = dM \propto M^{-\alpha}$. The straight line represents the best linear fit over the range of masses spanned by the line. The resulting indices α is 1.79 in this case. The dashed line denotes the minimum possible mass limit, which is estimated by the resolution limits and the rms noise. The figure is adapted from the Fig. 6 in the paper by Kramer et al. (1998b).	9
1.5	The GRS ^{13}CO intensity integrated over the velocity range relevant for emission from the individual cloud complexes. The beam size is indicated as a filled circle in the lower left corner of each panel. Top panels : Quiescent clouds; Bottom: Star-forming clouds. The figure is adapted from the Fig. 2 in the paper by Simon et al. (2001).	10

- 1.6 One example of galactic photon dominated region: NGC 3603 observed by HST. Sher 25, the evolved blue supergiant, is to the upper right of center. The star has a unique circumstellar ring of glowing gas. A starburst cluster is near the center. A torrent of ionizing radiation and fast stellar winds from these massive stars has blown a large cavity around the cluster. The giant gaseous pillars to the right and lower left of the cluster are the evidence of the interaction of ionizing radiation with cold molecular-hydrogen cloud material.
(<http://hubblesite.org/newscenter/archive/releases/1999/20/image/a/>). 11
- 2.1 Map of the integrated intensity of the ^{13}CO 1–0 in the Perseus cloud (Bachiller & Cernicharo, 1986). 15
- 2.2 Integrated intensity map of ^{12}CO 1–0 in Cepheus (Masur, 2005). Cepheus A to Cepheus F are marked. The white stars donate the stars in Cepheus OB3 association. 17
- 3.1 The ^{12}CO 3–2 spectra in one $10' \times 10'$ field. 19
- 3.2 The spectra of ^{12}CO 3–2 (black) and ^{13}CO 2–1 (red or grey in black and white) at the center of the observed map. 21
- 3.3 The Perseus molecular cloud complex. KOSMA maps of integrated intensities of ^{13}CO 2–1 (colors) and ^{12}CO 3–2 (contours) at $150''$ resolution. The integration interval is $0\text{--}16\text{ km s}^{-1}$. Colors run from 1 K km s^{-1} ($\sim 1\sigma$) to 32 K km s^{-1} . Contours range from 6.6 K km s^{-1} ($\sim 3\sigma$) to 83 K km s^{-1} in steps of 9 K km s^{-1} . The (0,0) position corresponds to RA=03:26:00, DEC=+31:10:00 (B1950). Seven sub-regions are marked by dotted square boxes of $50' \times 50'$ 22
- 3.4 Overlay of ^{13}CO 2–1 integrated intensities (contours) with a map of optical extinctions in colors (Goodman, 2004; Alves et al., 2005). Contours range from 2.7 K km s^{-1} (3σ) to 32 K km s^{-1} by 3 K km s^{-1} . Colors range from $A_V = 1\text{ mag}$ to 11 mag . Resolutions are $2.5'$ for ^{13}CO and $5'$ for A_V . A polygon marks the boundary of the ^{13}CO map. 23
- 3.5 ^{13}CO 2–1 velocity channel maps of the Perseus region. The velocity range runs from 3 km s^{-1} to 11 km s^{-1} with an interval of 1 km s^{-1} which is indicated on the top of each plot. The intensities are plotted from 0.7 K km s^{-1} ($\sim 1\sigma$) to 15 K km s^{-1} 25

- 3.6 Mean and rms of the equivalent line widths Δv_{eq} of the ^{12}CO 3–2 and ^{13}CO 2–1 spectra for the observed positions of the seven $50' \times 50'$ sub regions (Fig. 3.3). The dashed line delineates equal widths in ^{12}CO and ^{13}CO . The error bars indicate the difference between the minimum/maximum and the mean values. 26
- 3.7 Δ -variance analysis of the off-line channel maps. In the upper plot a velocity span corresponding to the integrated intensity maps is used. The two regions representing opposite extremes in the structural behaviour, NGC 1333 and L1455, show about the same spectral index of the colored noise in both transitions for small lags. In the lower plot, the influence of different velocity spans, as used in the velocity channel analysis (Sect. 3.3.2), is studied for L1455. The colored noise index d_{noise} is nearly constant independent of species, transition, velocity range Δv_{ch} , and center velocity v_{cen} . . 28
- 3.8 Δ -variance spectra of integrated intensities. **a)** Spectra obtained from the CO maps and the A_V data of the region mapped with the KOSMA telescope. **b)** Spectra of integrated intensity maps of two $50' \times 50'$ sub-regions: NGC 1333 and L 1455. Power-law fits to the data corrected for noise and beam-blurring are indicated as solid lines. 29
- 3.9 Comparison of the index spectrum of the ^{13}CO 2–1 data in L 1455 with the average line profile. The index spectrum is created by power-law fits to the Δ -variance spectrum of individual channel maps ($\Delta v_{\text{ch}} = 0.22 \text{ km s}^{-1}$). The vertical error bars represent the uncertainty of the fit. The horizontal error bars indicate the velocity channel width. 32
- 3.10 Comparison of the index spectra obtained for different velocity channel widths with the average line profile. The upper plots show the results for IC 348, the central plot NGC 1333 and the lower plot L 1455. For the left column I used the ^{12}CO 3–2 data, the right column represents the ^{13}CO 2–1 data. The different symbols indicate the results from different velocity channel widths. The dashed lines represents the index of the integrated intensity maps. 33

- 3.11 Average spectral indices of the channel maps as a function of the channel width. **a)** shows the average over the full line width. **b)** represents only the indices in the blue line wings. The line wing components are centered at 5 km s^{-1} for NGC 1333, at 4 km s^{-1} for L 1455, and at 7 km s^{-1} for IC 348. The error bars contain the fit error and the standard deviation of the indices within the considered velocity range. To avoid overlapping error bars in the plot, I have shifted the points for IC 348 and NGC 1333 by $\pm 0.02 \text{ km s}^{-1}$ relative to their actual position. 35
- 3.12 Sketch adopted from Fig. 3 of Sancisi (1974) illustrating the spatial arrangement and motion of the Perseus cloud complex. The gas is swept up by a shock expansion with 12 km s^{-1} . Due to the overall curvature, the line-of-sight velocity is 9 km s^{-1} for IC 348, but only 7 km s^{-1} for NGC1333. The diameter of the cloud is $\sim 20 \text{ pc}$. Pillar-like structures are left at lower velocities as remainders of high-density regions which were not accelerated to the same velocity. 37
- 4.1 Velocity (v_0) of the clumps found in NGC 1333 versus peak intensity (amp.). The average spectrum of ^{13}CO 2-1 in NGC1333 is also presented. 41
- 4.2 An example of the effect of different clump mass binning sizes. The bin size changes from $10^{0.2} M_{\odot}$, $10^{0.3} M_{\odot}$, $10^{0.4} M_{\odot}$, to $10^{0.5} M_{\odot}$. Error bars represent the standard deviation of a Poisson distribution $\sqrt{\Delta N}$. The dashed line denotes the lower clump mass limit ($10 * M_{\min}^{\text{limit}}$). 43
- 4.3 Clump mass spectra of the Perseus molecular cloud from both the FCRAO ^{13}CO 1-0 data and the KOSMA ^{13}CO 2-1 data. Both spectra are fitted by a power law function $dN = dM/M^{-\alpha}$. The straight line represents the best linear fit over the range of masses spanned by the line. The resulting indices α for both datasets are very similar, ~ 1.9 . The two vertical dashed lines show the 10 times of the lower mass limits for both tracers. 45
- 4.4 Clump mass spectra of the seven sub-sets in the Perseus molecular cloud. All spectra are fitted by a power law function $dN = dM/M^{-\alpha}$. The straight line represents the best linear fit over the range of masses spanned by the line. The resulting indices α lie in the range 1.65 to 1.85. The vertical dashed line shows the 10 times of the lower mass limits. 47

- 4.5 Size-line width (top panel) and size-mass (bottom panel) relations for the Perseus cloud using ^{13}CO 2–1 data. Least-squares fits to $\Delta v \propto R^{\alpha_w}$, and $M_{\text{LTE}} \propto R^{\alpha_m}$ are presented by the solid lines. The dashed lines show fit with fixed power law indices of $\alpha_w = 0.5$ and $\alpha_m = 2$, which correspond the conventional Larson relations (Larson, 1981). 48
- 4.6 Same as Fig. 4.5, but for two examples of seven sub-regions: NGC 1333 and L 1455. 49
- 4.7 Ratio of virial to LTE mass as a function of LTE mass for the clumps in the Perseus cloud. The dotted line corresponds to $M_{\text{vir}} = M_{\text{LTE}}$; The dashed line shows the 10 times of the lower mass limits for M_{LTE} . The solid line presents a power law index of $-\frac{2}{3}$ 51
- 4.8 Same as Fig. 4.7, but for two examples of seven sub-regions: NGC 1333 and L 1455. 51
- 4.9 Histograms of the external pressures needed to bind the clumps for the whole Perseus cloud. The solid line donates a Gaussian fit to the results. 52
- 4.10 Same as Fig. 4.9, but for two examples of seven sub-regions: NGC 1333 and L 1455. 53
- 5.1 Velocity integrated intensities of [C I] emission (*color*) overlayed with contours of (a) ^{12}CO 4–3, (b) ^{12}CO 1–0 and (c) ^{13}CO 1–0 integrated intensities at a common angular resolution of $70''$. The center of the maps is at $\alpha = 03^h44^m10^s$, $\delta = 32^\circ06'$ (J2000). All tracers are integrated from V_{LSR} 2 km s^{-1} to 14 km s^{-1} . Contours range between 20% to 90% with a step of 10% of the peak intensities that are 73 K km s^{-1} for ^{12}CO 4–3, 72 K km s^{-1} for ^{12}CO 1–0 and 31 K km s^{-1} for ^{13}CO 1–0. The seven filled triangles indicates the positions where I carry out a detailed PDR analysis later. The black star denotes the position of HD 281159. 57
- 5.2 Spectra of the four different tracers on those six positions along the cut from the northern edge of the cloud into the cloud, and on the seventh position at the south of the cloud. [C I] spectra in all the positions have been multiplied by 3. All panels have the same x axis from 3.5 km s^{-1} to 14.5 km s^{-1} and the same y axis from -0.5 K to 30.5 K 60

- 5.3 The top panel **(a)** presents the normalized integrated intensities of [C I], ^{12}CO 4–3, ^{12}CO 1–0 and ^{13}CO 1–0 in the seven selected positions. The typical errors of the intensities are about 15%; **(b)** displays integrated line intensity ratios. The x axes of all panels are the relative distance to the northern rim (8', 6') position. The southern rim is plotted in a separate box. 64
- 5.4 The color plot represents the ^{12}CO 4–3 / ^{12}CO 1–0 line intensity ratio (in units of K km s^{-1}) observed in the IC 348 cloud. The contours show the ^{12}CO 4–3 line intensity spaced at 10% intervals from 20% to 90% relative to the peak intensity of 73 K km s^{-1} . For line ratios, I only calculate for the positions where the line intensities of both tracer are larger than each 3 sigma value. 65
- 5.5 The C/CO column density ratio overlaid by ^{13}CO 1–0 integrated intensities contours. The contour levels are spaced at 10% intervals from 20% to 90% relative to the peak intensity of 31 K km s^{-1} . For column density ratios, I only calculate for the positions where the line intensities of ^{13}CO 1–0 are above the 3 sigma value. 66
- 5.6 FUV intensity distribution (contours) in IC 348 estimated from the IRAS FIR fluxes, overlayed on the [C I] integrated intensities (colors). The FUV intensity χ_{FIR} contour levels run from 5, 10, 20 to 100 by steps of 20 Draine units, χ_0 68
- 5.7 Comparison of the observed line intensity ratios [C I]/ ^{12}CO 4–3, [C I]/ ^{13}CO 1–0 and ^{12}CO 4–3/ ^{12}CO 1–0 at (1', -1') with the single clump KOSMA - τ PDR model calculations. The left figure shows the fitting of a clump mass and densities; the right one presents the fitting of the FUV field and clump densities. The middle drawn contours are the observed intensity ratios, and the outer two are those for the 20% uncertainty. The grey-scale images indicate the reduced χ^2 of the fit. The position of the minimum reduced χ^2 is marked using a white cross. The horizontal light blue line in the right panel shows the FUV flux χ_{FIR} from the HIRES data. 70
- 5.8 Observed (filled symbols) and modelled (drawn lines with open symbols) line intensities of ^{12}CO , ^{13}CO , and [C I] from Ensemble case 2 at the northern rim (left panel) and the southern rim (right panel). To better display the data, I artificially shift the [C I] frequency by +40 GHz for the observed intensity. 77

- 6.1 The MSX 8 micron PAH map of the Cepheus B PDRs overlaid by $C^{18}O$ 1–0 (thick black contours), ^{12}CO 1–0 (dashed black contours), radio continuum (white contours) and FUV field (dotted white contours). The two sets of three dashed lines in a row indicate the cuts I observed; the two white crosses show the two interface positions. The B 1 star, HD 217061 is denoted as an open triangle. The center (0,0) is corresponding to $\alpha = 22^h57^m07^s$, $\delta = 62^\circ37'33''$ (J2000). 84
- 6.2 The spectra of $HCS^+ 2-1$, $HNC 1-0$, $HNC 3-2$, $^{12}CO 1-0$, $^{13}CO 1-0$, $^{13}CO 2-1$, $C^{18}O 1-0$, $C^{18}O 2-1$, $HCO^+ 1-0$, $HCO^+ 2-1$, $HCO^+ 3-2$, $c-C_3H_2 2_{1,2}-1_{0,1}$, $H^{13}CN 1-0$, $H^{13}C^+ 1-0$, $HC_3N 1-0$, $HCO 1-0$, $C^{34}S 2-1$, $C^{34}S 3-2$, $CS 2-1$, $CS 3-2$, $CS 5-4$, $HCN 1-0$, $HCN 2-1$ and $HCN 3-2$ at the two interface positions. 86
- 6.3 Spectra at the interface ($60''$, $-185''$). In the sequence of left to right and top to bottom, there are $C_2H 1-0$, $2-1$, $3-2$, $HCN 1-0$, $2-1$, $3-2$ and part of $CN 1-0$ and $2-1$. The green lines are the results from the hyperfine structure fit. 89
- 6.4 Spectra at the interface ($20''$, $-50''$). In the sequence of left to right and top to bottom, there are $C_2H 1-0$, $2-1$, $3-2$, $HCN 1-0$, $2-1$, $3-2$ and part of $CN 1-0$ and $2-1$. The green lines are the results from the hyperfine structure fit. 90
- 6.5 The distribution of integrated intensities along the two cuts. The x axis indicates the relative distance to those two interface positions. Negative and positive distances are assigned to the west and east of those two interface positions, respectively. 92
- B.1 The the water vapor comparison between the input and calibrated values for low and normal receiver temperatures. The left panel shows the comparison for single calibration and the right panel presents the comparison for common calibration. 113
- B.2 The the water vapor comparison between the input and calibrated values when T_{amb} is equal to T_{sky} 114
- B.3 The the water vapor comparison between the input and calibrated values for sky temperature lower than ambient temperature. The left panel shows the comparison for single calibration and the right panel presents the comparison for common calibration. 115
- B.4 The the water vapor comparison between the input and calibrated values for sky temperature greater than ambient temperature. The left panel shows the comparison for single calibration and the right panel presents the comparison for common calibration. 116

- B.5 The water vapor comparison between the Hiyama and the new calibration methods. The drawn lines are where the two methods give the same water vapor. 117

List of Tables

- 3.1 Basic observation parameters. The first two columns indicate the line and transition frequency, followed by the main beam efficiency, B_{eff} . The telescope Half Power Beam Width (HPBW) (considering a distance of 350 pc, I converted the angle distance to distance) is listed in Column four. Column five is the observing grid and Column six is the number of observation points. Δv denotes the velocity resolution and T_{rms} is the average rms noise temperature per channel on a T_{mb} scale. 20
- 3.2 Dynamic range. Column one and two indicate the line and mapped area (I adopted the 350 pc as the distance) followed by the ratios of mapped area over beam size, the peak temperature over the average rms noise temperature and the σ . The σ is defined: $\sigma = \sqrt{N} \Delta V_{res} T_{rms}$. And the velocity range is from 0 km s^{-1} to 16 km s^{-1} 20
- 3.3 Results of the Δ -variance analysis of the integrated CO maps and the A_V data for the region mapped with KOSMA (Fig. 3.3). . . . 30
- 3.4 Results of the Δ -variance analysis of the KOSMA data for seven $50' \times 50'$ sub-regions of the cloud (Figure 3.3). The spectral indices β were fitted in the size range 2.2-14' for the ^{13}CO 2-1 and in the size range 1.4-14' for the ^{12}CO 3-2 data. 30

- 4.1 Comparison of the masses of clump identified in the Perseus cloud with studies of other molecular clouds. The cloud name, studied tracers, distance, and the HPBW are listed in Column (1), (2), (3) and (4); Column (5) presents the number of selected clumps; The mass range used for the least-squares fit is in Column (6). Column (7) and (8) present the total mass of all clumps selected and the minimum mass identified with the criteria of Equation 1.4; The fitted power law index α is given in Column (9) (note that I adopt the power law index for a bin size of $10^{0.2} M_{\odot}$ for comparison); Column (10) is the reference: ^a This work; ^b Kramer et al. (1998b); ^c Simon et al. (2001). 44
- 4.2 The results of the seven sub-regions. The cloud name is listed in Column (1); Column (2) presents the number of selected clumps; The mass range used for the least-squares fit is in Column (3). Column (4) and (5) present the total mass of all clumps selected and the minimum mass identified with the criteria of Equation 1.4; The fitted power law index α is given in Column (6). 46
- 5.1 The observed integrated line intensities (in $\text{erg s}^{-1} \text{sr}^{-1} \text{cm}^{-2}$) and line ratios at the seven selected positions. The errors on the integrated intensity are estimated to be $\sim 15\%$ 62
- 5.2 Results of the LTE analysis. The excitation temperature T_{ex} is listed in Column (2); Column (3) - (5) present C, CO and H_2 column densities; the C/CO ratio is listed in Column (6). The uncertainties of the column densities are derived by varying the integrated intensities by $\pm 15\%$ 65
- 5.3 Physical parameters at selected positions in Fig 5.1, obtained by fitting the observed intensity ratios to the **single clump** KOSMA - τ PDR models. Columns (2) - (5) list the fitted clump densities, clump mass, clump radius and FUV field; the derived FUV field from the HIRES data and from the star are in Column (6) and (7); The distance to HD 281159 used for the calculation of χ_{star} is listed in Column (8); Column (9) is the minimum chi square of the PDR fit. 71

5.4	Results of ensemble of identical clumps, Ensemble case 1 . The mass and FUV field for each single clump are listed in Column (2) and (3); Column (4) - (6) present the line intensity ratios between the ensemble models and observations of ^{12}CO 4–3, ^{12}CO 1–0 and ^{13}CO 1–0; The C, CO and H_2 column densities from the ensembles are presented in Column (7), (8) and (9); Column (10) is the C/CO ratios. The total number of the clumps in the ensemble and ensemble mass are listed in Column (11) and (12) The total ensemble mass M_{ens} listed in the table is computed as $M_{\text{ens}} = N_{\text{ens}} \times M_{\text{cl}}$, where M_{cl} is the mass of a clump.	73
5.5	Results of ensembles with a clump mass distribution and mass-size distribution, Ensemble case 2 . Column (2) - (4) present the ratios (in $\text{erg s}^{-1} \text{sr}^{-1} \text{cm}^{-2}$) of the modelled and observed line intensities for ^{12}CO 4–3, ^{12}CO 1–0 and ^{13}CO 1–0; The mean clump ensemble density n_{mean} and the fitted FUV field χ_{ens} are presented in Column (5) and (6). The C, CO and H_2 column densities from the ensembles are presented in Column (7), (8) and (9); Column (10) is the C/CO ratios. The total masses are listed in Column (11).	76
6.1	Rest frequencies of observed spectral lines	82
6.2	Line Parameters on the two interface positions besides for CO and its isotopes. ND is indicates non-detection.	87
6.3	The results of hyperfine transition fitting for C_2H , CN and HCN.	88
6.4	Molecular constants used for column density calculations. μ is permanent dipole moment and B is rotational constant. All the data are taken from the Cologne Database for Molecular Spectroscopy (CDMS, see http://www.astro.uni-koeln.de/vorhersagen/)	93
6.5	LTE analysis for CO, CS, HCO^+ , HCN, HNC, HCS^+ and HCO at the two interface positions. The opacities of ^{12}CO 1–0, ^{13}CO 1–0, C^{18}O 1–0, CS 2–1, C^{34}S 2–1, HCO^+ 1–0, H^{13}CO^+ 1–0, HCN 1–0, HNC 1–0, HCS^+ 2–1 and HCO 1–0 are listed at the top. The excitation temperatures of CO, CS, HCO^+ , HCN, HNC, HCS^+ and HCO are listed in the middle. The column densities of H_2 , ^{12}CO , ^{13}CO , C^{18}O , CS, C^{34}S , HCO^+ , H^{13}CO^+ , HCN, HNC, HCS^+ and HCO are listed at the bottom.	94
6.6	Results of the relative column densities to H_2 column density at two interface positions. $X(Y)$ is the fractional abundance of tracer Y relative to H_2 : $N(Y)/N(\text{H}_2)$	95

Acknowledgments

Foremost, my deepest gratitude goes first to my advisors Prof. Jürgen Stutzki and Carsten Kramer for their constant encouragement and advise. I am very grateful for their patience, enthusiasm, and immense knowledge in astrophysics. They are always willing to answer my questions. Their penetrating and insightful comments afford me with inspiring source. I also thank their suggestions and corrections on this thesis. Without their consistent and illuminating instruction, this thesis could not have reached its present form.

I also like to thank Prof. Andreas Zilges for co-refereeing this thesis.

I would also like to extend my sincere thanks to all members in A1 and A6 groups of SFB 494 from I. Physikalisches Institut for providing a very friendly and inspiring working atmosphere. I specially thank Martin Miller for helping me adapt to a new country. It would be much harder without his help on all those things like opening a bank account, first-time registration in the university and so on. I thank him for introducing me to get familiar with the KOSMA 3m telescope observations. I also thank him and his wife for providing me a place to stay at the beginning of my study in Köln.

I thank Bhaswati Mookerjee who not only gave me the fruitful scientific discussions on the PDR analysis in IC 348, but also passed me her tips on living in Germany. I also thank Volker Ossenkopf for helping me with the Δ -variance and PDR analysis and also for letting me using his IDL codes for the Δ -variance analysis. I am greatly indebted to him for those very useful and inspiring discussions. I appreciate the help from Markus Röllig on the PDR analysis. I also thank Frank Bensch for his great help on the Δ -variance analysis and for letting me use his Fortran codes on the Δ -variance analysis. Once more, I thank all those people I have mentioned for their great and patient help on the language corrections of the published papers.

I am indebted to Robert Simon for his great help on using GILDAS software. He is such an expert on GILDAS. Whenever I encountered the difficulties on data reduction, he is always the first one I would ask for help and tips. I would like also to thank Nikolaus Volgenau for his patience with my English. I thank Martina Wiedner for her help, as it is very nice to chat with someone who can speak a little

Chinese.

I also thank Marc Hitschfeld, Martin Emprechtinger, Markus Cubick and Oliver Baum for their help and chats and for their skills in spreading happiness. I really appreciate their help with my German translations, especially Marc's. Because I often bothered him with my German letters, and with asking him to help me contact with people who only speak German. I thank Holger Jakob and Martin Brüll for their help on the data reduction. Some of the startup scripts I used are from them. I also appreciate the help from Bettina Krause, Stefanie Krämer and Marlies Selt.

I also thank those Japanese colleagues for their supports during my NANTEN2 observations. I thank the staff at the IRAM 30m telescope for their support during my observations. I really like the environment at the 30m telescope, especially the food there.

I am very grateful to helpful discussions with Alex Lazarian and Doug Johnstone on the Δ -variance analysis. I also thank Joao Alves for providing us the 2MASS extinction data. I thank Naomi Ridge for allowing us to use the FCRAO low- J CO data in IC 348. I thank Hans Ungerechts for letting me use the low- J CO data in Cepheus B. In this work, I used the NASA/IPAC/IRAS/HIRES data reduction facilities.

I thank to all the friends I made in Köln for giving me the opportunity to spend a great time during my PhD study. I am grateful to my parents for their support during all these years. They always have faith in me. I also thank Jiayu for her patience and encouragement since we met during our undergraduate studies.

I acknowledge the financial support from the grant SFB494 of the Deutsche Forschungsgemeinschaft during my PhD study.

Erklärung

Ich versichere, dass ich die von mir vorgelegte Dissertation selbständig angefertigt, die benutzten Quellen und Hilfsmittel vollständig angegeben und die Stellen der Arbeit einschließlich Tabellen, Karten und Abbildungen, die anderen Werken im Wortlaut oder dem Sinn nach entnommen sind, in jedem Einzelfall als Entlehnung kenntlich gemacht habe; dass diese Dissertation noch keiner anderen Fakultät oder Universität zur Prüfung vorgelegen hat; dass sie abgesehen von unten angegebenen Teilpublikationen noch nicht veröffentlicht worden ist sowie, dass ich eine solche Veröffentlichung vor Abschluss des Promotionsverfahrens nicht vornehmen werde. Die Bestimmungen der Promotionsordnung sind mir bekannt. Die von mir vorgelegte Dissertation ist von Herrn Prof. Dr. Jürgen Stutzki betreut worden.

Kefeng Sun

Publications

- [1.] K. Sun, V. Ossenkopf, C. Kramer, B. Mookerjee, M. Röllig, M. Cubick, M., and J. Stutzki, J., *The Photon Dominated Region in the IC 348 molecular cloud*, 2008, accepted by Astronomy & Astrophysics
- [2.] J.L. Pineda N. Mizuno, J. Stutzki, M. Cubick, et al. *Submillimeter line emission from LMC N159W: a dense and clumpy PDR in a low metallicity environment*, 2008, accepted by Astronomy & Astrophysics, (arXiv:0802.1929)
- [3.] M. Hitschfeld, M. Aravena, C. Kramer, F. Bertoldi, et al., *CO 4–3 and [C I] 1–0 in the centers of NGC4945 and Circinus*, 2008, Astronomy & Astrophysics, in press, (arXiv:0712.1924)
- [4.] C. Kramer, M. Cubick, M. Röllig, K. Sun, K., et al., *Photon-dominated regions in the Carina nebula. I. Maps of atomic carbon and mid-J CO lines with NANTEN2*, 2008, Astronomy & Astrophysics, 477, 547
- [5.] K. Sun, C. Kramer, V. Ossenkopf, F. Bensch, J. Stutzki, and M. Miller, *A KOSMA 7 deg² ¹³CO 2–1 and ¹²CO 3–2 survey of the Perseus cloud I. Structure analysis*, 2006, Astronomy & Astrophysics, 451, 539
- [6.] Y. Wu, Q. Zhang, W. Yu, M. Miller, R. Mao, K. Sun, and Y. Wang, *Ammonia cores in high mass star formation regions*, 2006, Astronomy & Astrophysics, 450, 607
- [7.] K. Sun, J. Yang, S. Luo, M. Wang, L. Deng, X. Zhou, and J. Chen, *Large-Scale Distribution of Herbig-Haro Objects in Taurus*, 2003, Chinese Journal of Astronomy and Astrophysics, 3, 458
- [8.] K. Sun, Y. Wu, and L. Wang, *High-velocity Gas near S106*, 2003, Acta Astronomica Sinica, 44, 94
- [9.] K. Sun, and Y. Wu, *A new high-velocity molecular outflow of IRAS 19282+1814*, 2003, Chinese Astronomy and Astrophysics, 27, 73

Lebenslauf

Name : Kefeng Sun
Anschrift : Bachemer str. 46
50931 Köln
Geburtsdatum : 19.03.1978
Geburtsort : Wuxi, Jiangsu, China
Staatsangehörigkeit : Chinesisch
EMail : kefeng@ph1.uni-koeln.de

Schule

09. 1984 - 07. 1990 Luoshe-Zentral-Grundschule der Stadt Wuxi, Jiangsu, China
09. 1990 - 07. 1993 Luoshe-Mittelschule der Stadt Wuxi, Jiangsu, China
09. 1993 - 07. 1996 Obere Mittelschule Tianyi, Wuxi, Jiangsu, China

Universität

09. 1996 - 07. 2000 Peking Universität, Beijing, China
Bachelor of Science, Astrophysik
09. 2000 - 07. 2003 Peking Universität, Beijing, China
Master of Science, Astrophysik
01. 2004 I. Physikalisches Institut, Universität zu Köln, Deutschland
Beginn der Dissertation

Berufserfahrung

09. 2001 - 07. 2003 Wissenschaftliche Hilfskraft, Peking Universität
Beijing, China
10. 2001 - 11. 2001 Gastwissenschaftler, Purple Mountain Observatory
Nanjing, China
02. 2002 - 07. 2002 Tutor für Thermodynamics, Peking Universität, Beijing, China
09. 2003 - 11. 2003 Gastwissenschaftler, I. Physikalisches Institut
Universität zu Köln, Deutschland
seit 01. 2004 Wissenschaftlicher Mitarbeiter, I. Physikalisches Institut
Universität zu Köln, Deutschland

